The Rise of Amorphous Water-Splitting Materials

Sina Maghool [1], Sara Amirnejat [2], Ali Akbar Nosrati [3], Ali Akbar Asgharinezhad [4*], Afsanehsadat Larimi [5*]

[1] Department of Chemical and Petroleum Engineering, Sharif University of Technology, Tehran, Iran

[2] Department of Chemistry, Iran University of Science and Technology, Tehran, Iran

[3] Department of Chemistry, Kharazmi University, Tehran, Iran

[4] Chemistry and Process Research Department, Niroo Research Institute, Tehran, Iran

[5] Department of Chemical Engineering, Swansea University, Wales, UK

*Corresponding authors' Email: aasgharinezhad@nri.ac.ir (A. A. Asgharinezhad);

a.larimi@swansea.ac.uk (A. Larimi)

Abstract

Amorphous structural design offers a compelling route to raise the efficiency and durability of electrochemical water splitting. In contrast to crystalline lattices with activity confined to specific facets or grain boundaries, amorphous frameworks provide dense populations of under-coordinated sites, flexible local bonding that moderates adsorption energetics, and percolating pathways for electron/ion transport. These disordered phases can minimize interfacial resistance and, when coupled with hydrophilic surface chemistry and hierarchical porous/rough electrode architectures that often accompany amorphous coatings, enhance electrolyte access and gas-bubble removal during high-current operation, sustaining performance across diverse media. As a result, amorphous electrocatalysts can deliver competitive overpotentials and favorable kinetics in many systems, particularly when defect-rich phases are integrated with conductive scaffolds; however, performance remains system- and electrolyte-dependent.

This review assembles a structure-property-performance perspective on amorphous catalysts for water splitting. We show how short-range order, defect chemistry, and compositional tolerance can be orchestrated through accessible syntheses to tune intrinsic activity beyond rigid crystals. Collectively, the evidence positions amorphous architectures as a generalizable, manufacturable pathway to efficient, durable, and cost-effective water-splitting catalysts under realistic conditions. Although prior reviews discuss amorphous electrocatalysts, many focus on a single half-reaction or specific material families/architectures, limiting transferability into a unified design roadmap. Here, we bridge this gap by combining (i) reaction fundamentals and evaluation metrics, (ii) a synthesis-oriented discussion of how routes generate distinct amorphous structures, and (iii) a reaction-by-reaction analysis of HER, OER, and overall water splitting, enabling readers to match synthesis strategies to targeted reactions and performance goals.

Keywords: Amorphous structure; Water Splitting; Electrocatalysts; Oxygen Evolution Reaction; Hydrogen Evolution Reaction.

1.1 Introduction

The increasing global population and consequent climate change have heightened the need for dependable energy production and storage [1]. Nowadays, owing to reasons such as the environmental harm caused by fossil fuels, their major depletion due to excessive usage, and their non-renewable nature, researchers have increasingly concentrated on discovering acceptable alternatives [2–4]. Given the disadvantages of fossil fuels, the optimal substitute must exhibit essential attributes such as renewability, sustainability, and minimum environmental impact to adequately mitigate the shortcomings of traditional fossil energy sources [5].

Hydrogen is regarded as a viable substitute for traditional fossil fuels due to its elevated gravimetric energy density (120 MJ/kg), superior energy conversion efficiency, and the production of water as the only byproduct, in contrast to the harmful gases like carbon dioxide emitted by fossil fuels [6,7]. In addition, hydrogen is widely used in applications such as hydrocracking of crude oil, methanol synthesis, and ammonia production [8]. Hydrogen does not exist naturally in its elemental state and must be synthesized using designated techniques [9]. The predominant technique used is steam reforming, necessitating elevated temperatures and pressures, and leading to greenhouse gas emissions [10]. Consequently, establishing an effective and eco-friendly approach for hydrogen generation is a primary focus for researchers [11].

Electrochemical water splitting is considered an environmentally friendly and pollution-free method for hydrogen production, making it a promising alternative to conventional approaches [12,13]. The water splitting reaction consists of two main half-reactions: the anodic Oxygen Evolution Reaction (OER) and the cathodic Hydrogen Evolution Reaction (HER) [14]. As illustrated in Figure 1a, hydrogen is generated during electrolysis at the cathode (HER), while oxygen is simultaneously evolved at the anode (OER), and the produced H_2 can then be directed to various downstream applications (Figure 1b).

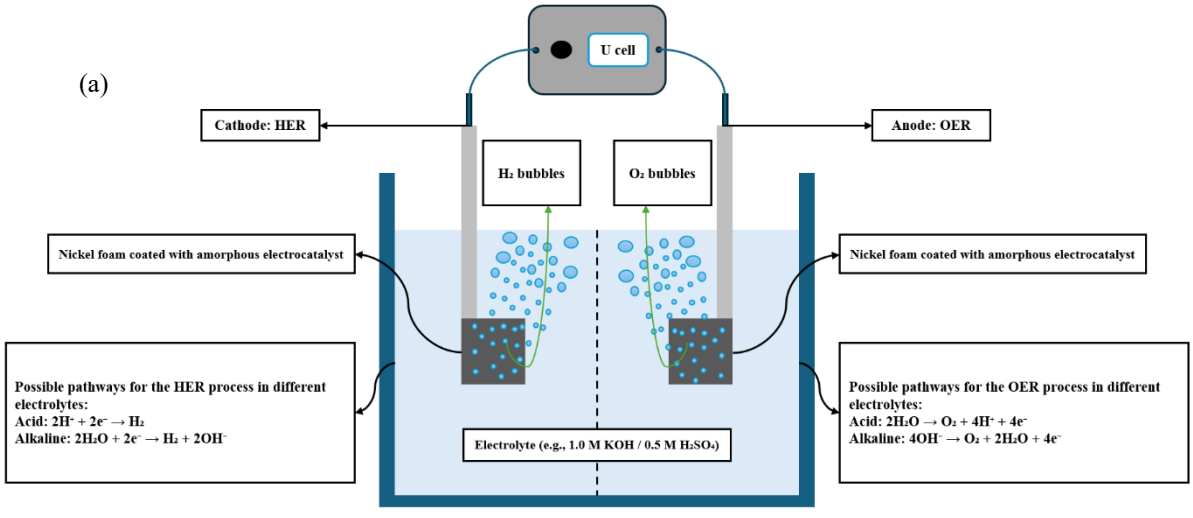

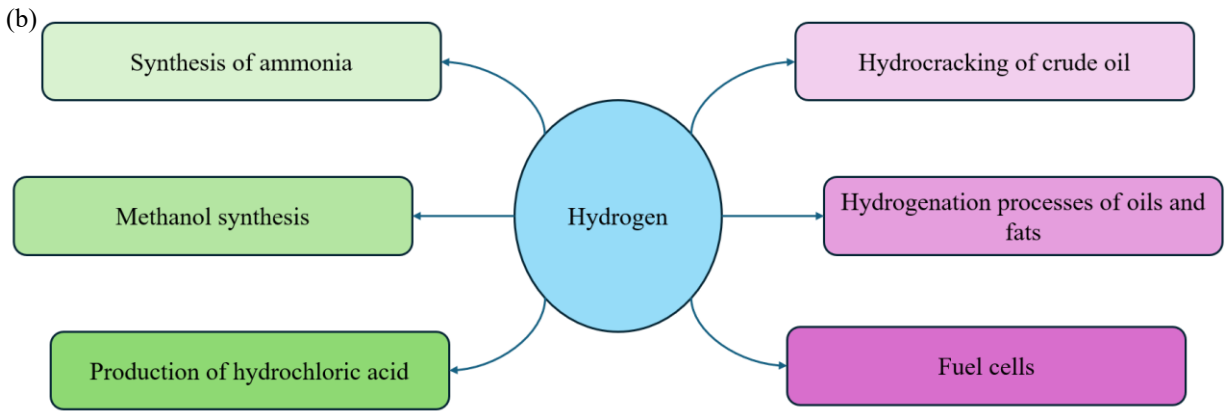

Figure 1. (a) Schematic illustration of hydrogen production via the water splitting process; (b) The potential applications of the produced hydrogen.

Ideally, the water splitting reaction occurs at 1.23 V [15]. However, in practice, it requires higher voltages due to kinetic limitations [16]. To reduce the required voltage and bring it closer to theoretical value, the use of electrocatalysts presents an effective solution [17,18]. Catalyst structure has become the decisive lever for lowering kinetic barriers in both the OER and HER. Whereas conventional crystalline electrocatalysts offer well-defined facets and robust band transport, their activity is often confined to a limited set of surface terminations and grain boundaries. By contrast, amorphous materials, lacking long-range order but retaining short-range coordination, present a dense population of under coordinated metal sites, flexible bond environments, and defect rich, percolating networks [19]. These features collectively increase the number of accessible active sites, relax adsorption-desorption energetics for key intermediates, and facilitate rapid interfacial charge transfer [20,21]. Moreover, the absence of long range order yields dense populations of under-coordinated sites, flexible local bonding that tunes adsorption energetics, and continuous percolation pathways for electron/ion transport [22,23]. When grown directly on conductive scaffolds or implemented as binder-free coatings, they minimize contact resistance and can improve electrolyte replenishment and gas removal, primarily through the accompanying surface chemistry and hierarchical micro/nanostructure (roughness/porosity) often produced during amorphous synthesis and electrochemical activation, and sustain performance at practical current densities [24]. Their broad compositional tolerance enables synergistic multi-metal and multi-anion effects, while the defect tolerant network generally imparts mechanical and chemical robustness during prolonged operation [21,25].

While amorphization is frequently associated with higher apparent activity, a higher degree of disorder does not automatically guarantee superior electrocatalysis. Excessive structural disorder may compromise long-range electronic percolation, reduce the persistence of catalytically competent local motifs, or accelerate dissolution/reconstruction under bias, thereby penalizing sustained performance. Recent perspectives instead emphasize short- to medium-range order as a key descriptor: retaining chemically meaningful coordination environments within a disordered matrix can preserve favorable adsorption energetics while maintaining transport pathways [26]. In practical electrode architectures, this often manifests as an “optimal disorder window,” and is one reason why amorphous-conductive hybrids, where the amorphous domain supplies site density

and the ordered/metallic domain supplies conductivity and mechanical integrity, frequently outperform either extreme [27,28].

Recent review articles have undoubtedly advanced the field, but they are often segmented in ways that limit their use as a practical guide for materials design. A substantial portion of the literature is organized around one half-reaction, most commonly OER-focused discussions of amorphous catalysts, which are highly valuable but do not simultaneously guide HER and overall water splitting design choices [29]. Other reviews are highly focused on a specific architecture (e.g., amorphous-crystalline heterostructures) or a specific catalyst class (e.g., amorphous noble-metal systems or high-entropy amorphous catalysts), which provides depth but can leave readers without a unified synthesis roadmap across the broader range of amorphous structures relevant to HER/OER/overall water splitting [30–32]. Additionally, broader "amorphous electrocatalysis" reviews cover multiple reactions beyond water splitting, so water-splitting-specific synthesis decisions and structure–function comparisons can become less explicit [33].

Motivated by these advantages, the purpose of this review is to provide a single, synthesis-guided framework for amorphous electrocatalysts in water splitting that connects "how the amorphous structure is made" with "how it is used" across HER, OER, and overall water splitting, and we clarify where amorphous phases match or outperform crystalline analogues under similar chemistry and experimental protocols, while it is clear that crystalline benchmarks remain more effective in some conditions (e.g., rutile IrO_2 in acidic OER; high-activity crystalline oxides/perovskites in alkaline media). The main contributions and novelties are: (1) a consolidated overview of HER and OER fundamentals to anchor interpretation of activity trends; (2) a synthesis-oriented comparison of routes used to produce amorphous structures (and amorphous-derived structures), explaining what structural features each route tends to generate and how these features can be intentionally selected; (3) a reaction-by-reaction discussion of amorphous catalysts for HER and OER, followed by an integrated view of overall water splitting, which highlights how bifunctionality is achieved and evaluated; and (4) a practical "reader's roadmap" that helps researchers choose amorphous-structure synthesis strategies that align with the targeted reaction and operating conditions.

1.2 Fundamental Mechanisms

The first concept of an electrochemical cell, consisting of three primary components: an anode, a cathode, and an electrolyte, was presented in 1789 [12]. In this cell, two half-reactions transpire at the electrodes: the cathodic HER and the anodic OER, resulting in the production of hydrogen and oxygen gases [34]. The comprehensive water splitting process is shown in Equation 1.

$$H_2O\ (l) \rightarrow H_2(g) + \frac{1}{2}O_2\ (g) \quad (1)$$

Although water is a relatively stable molecule, it has inadequate electrical conductivity; and the conductivity of water is greatly affected by the pH of the electrolyte; acidification or alkalization of the environment improves ion transport [35]. Furthermore, the pH of the electrolyte influences the reaction pathways of the anodic and cathodic processes, which adhere to different mechanisms in acidic and alkaline environments, as seen in the equations below [36].

Cathodic reactions:

$$4H^+ + 4e^- \rightarrow 2H_2 \text{ (In acidic medium)} \quad (2)$$

$$4H_2O + 4e^- \rightarrow 2H_2 + 4OH^- \text{ (In basic medium)} \quad (3)$$

Anodic reactions:

$2H_2O \rightarrow O_2 + 4H^+ + 4e^-$ (In acidic medium) (4)

$4OH^- \rightarrow O_2 + 2H_2O + 4e^-$ (In basic medium) (5)

Theoretically, the water-splitting process is expected to occur around 1.23 V [35]. In fact, even with commercial electrocatalysts, an extra voltage of 0.55 to 0.77 V is often necessary [37]. The voltage difference is referred to as overpotential (η), which mostly results from numerous resistances inside the electrochemical cell that impede electron transmission and decelerate reaction kinetics [38]. Current studies mostly concentrate on the advancement of electrode materials to substantially diminish this overpotential [39]. This approach may significantly reduce the total energy consumption and, therefore, the cost of hydrogen and oxygen production via water splitting [40]. In the following sections, a more detailed explanation of the mechanisms and pathways involved in the production of hydrogen and oxygen will be provided.

1.2.1 Fundamentals of the HER

The mechanism of the HER has been thoroughly examined by scholars. It has been shown that, in both acidic and alkaline electrolytes, the hydrogen evolution reaction typically occurs via three essential phases [41]. The particular chemical pathways vary according to the pH of the electrolyte [35]. The following equations illustrate the distinct reaction stages for the HER in both acidic and alkaline environments (the * shows the active site of the electrocatalyst) [42].

Volmer:

$H^+ + e^- \rightarrow H^*$ (In acidic medium) (6)

$H_2O + e^- \rightarrow H^* + OH^-$ (In basic medium) (7)

Heyrovsky:

$H^+ + e^- + H^* \rightarrow 2H_2$ (In acidic medium) (8)

$H_2O + e^- \rightarrow H_2 + OH^-$ (In basic medium) (9)

Tafel:

$2H^* \rightarrow H_2$ (In acidic and basic medium) (10)

Irrespective of the electrolyte's acidity or alkalinity, the first phase of the HER entails the adsorption of hydrogen atoms onto the electrocatalyst's surface [43]. This phase is referred to as the Volmer reaction, whereby hydrogen intermediates are generated [44]. The subsequent phase is the desorption of H_2, which may occur via two distinct pathways: an electrochemical method or a chemical approach. These are designated as the Heyrovsky and Tafel reactions, respectively [45]. In the Heyrovsky reaction, the adsorbed hydrogen intermediate interacts with either a proton in acidic conditions or a water molecule in alkaline conditions to generate hydrogen gas [46]. In contrast, the Tafel reaction involves the chemical recombination of two adsorbed hydrogen intermediates to form molecular hydrogen [47]. Figure 2a provides a graphical representation of the reaction pathways involved in the HER, illustrating the sequence of steps and the associated intermediates.

To identify the rate-determining step among the three primary phases in a certain HER process, the Tafel slope obtained from the HER polarization curve is often examined. The value of the Tafel slope provides insight into the reaction mechanism [48]. The Tafel slopes of roughly 29.5 mV/dec,

39 mV/dec, and 118 mV/dec indicate that the Tafel, Heyrovsky, and Volmer steps are the rate-limiting processes, respectively [49].

A crucial measure that offers significant insights into the performance of various materials in the HER process is the hydrogen adsorption free energy (ΔG_{H^*}) [50]. The correlation between exchange current density and Gibbs free energy of hydrogen adsorption is often shown by a volcano plot (Figure 2b) [51]. A substantially positive ΔG_{H^*} signifies a weak contact between hydrogen atoms and the electrocatalyst surface, making the Volmer step the rate-limiting phase. Conversely, if ΔG_{H^*} is significantly negative, the adsorbed hydrogen exhibits excessive binding to the surface, impeding its desorption and hence retarding the Tafel or Heyrovsky steps [52]. Figure 2b illustrates that platinum (Pt) is positioned toward the apex of the volcano plot, with a ΔG_{H^*} value approaching zero. This signifies an ideal equilibrium between hydrogen adsorption and desorption, establishing Pt as a superior electrocatalyst for HER, a conclusion corroborated under realistic operating conditions.

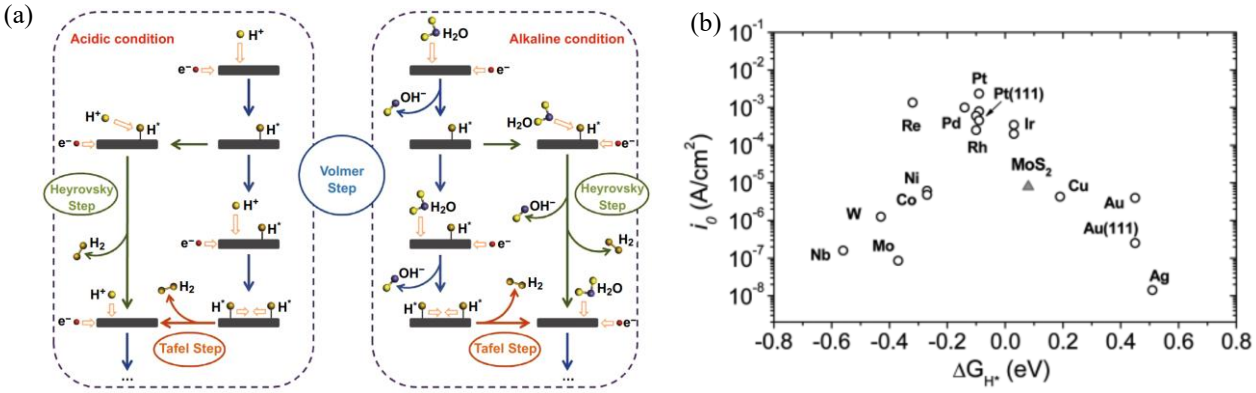

Figure 2. (a) Schematic paths for the HER in acidic and alkaline environments [53]; (b) Exchange current density vs Gibbs free energy plot [54].

1.2.2 Fundamentals of the OER

In contrast to the HER process, the OER, the complementary half-reaction in total water splitting, demonstrates markedly slower kinetics and necessitates a greater overpotential to occur [55]. This is mainly because to the intricacy of the OER process, which encompasses four proton-coupled electron transfer stages and the difficult creation of the O–O bond [56]. The OER is a multifaceted and intricate reaction, with its mechanism significantly influenced by the structure and content of the electrode material [57]. The commonly known OER processes in both acidic and alkaline environments are delineated as follows [58].

In acidic environments:

$$H_2O + * \rightarrow *OH + H^+ + e^- \quad (11)$$

$$*OH \rightarrow *O + H^+ + e^- \quad (12)$$

$$*O + H_2O \rightarrow *OOH + H^+ + e^- \quad (13)$$

$$*OOH \rightarrow O_2 + H^+ + e^- + * \quad (14)$$

In alkaline environments:

$$* + OH^- \rightarrow *OH + e^- \quad (15)$$

$$*OH + 0H^- \rightarrow *O + H_2O + e^- \quad (16)$$

$$*O + 0H^- \rightarrow *OOH + e^- \quad (17)$$

$$*OOH + 0H^- \rightarrow O_2 + H_2O + e^- + * \quad (18)$$

The * denotes the active spots on the surface of the electrocatalyst. The combining of the newly created intermediates, *O, *OOH and *OH to gaseous oxygen is very challenging owing to the significant thermodynamic barrier [59]. This is the main reason behind the sluggish kinetics of the OER and the relatively high overpotential required to drive the reaction. Additionally, the oxygen evolution pathway is illustrated in Figure 3a. Prior theoretical investigations have shown that the binding energies of intermediary species in the process are linked by scaling connections [60]. This indicates that catalytic activity is often characterized by a single descriptor, such as the Gibbs free energy differential between O* and HO* [61]. The catalytic performance of OER, when graphed against this description, often produces a volcano-shaped curve , like to that seen in HER, as shown in Figure 3b [62]. The volcano figure indicates that peak catalytic efficiency occurs when the binding affinities of the intermediates are ideally matched [63]. The volcano plot offers a qualitative assessment of the efficacy of different structures in the OER process [64]. It functions as an essential instrument for directing the logical design and forecasting of novel electrocatalyst structures [65].

Figure 3b illustrates that Ru-based structures have superior performance in the OER owing to their proximity to the apex of the volcano plot [66]. The increased catalytic activity has been repeatedly validated by experimental findings.

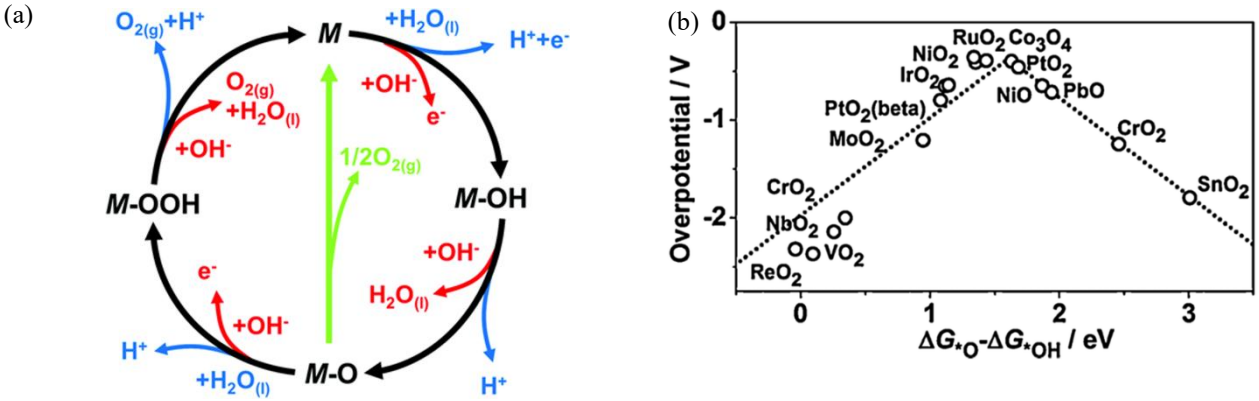

Figure 3. (a) The oxygen evolution reaction (OER) proceeds via different pathways under acidic (blue line) and alkaline (red line) conditions. One common route, shown by the black line, involves the formation of a peroxide intermediate (M–OOH). Alternatively, a direct coupling between two neighboring oxo species (M–O), represented by the green line, can also lead to O_2 production [67]; (b) Volcano plot for OER on metal oxides [68].

1.2.3 Volcano plot under structural disorder

Volcano plots are commonly used as design maps because they compress complex multistep electrochemical kinetics into a small set of thermodynamic descriptors. For HER, the key descriptor is typically the hydrogen adsorption free energy (ΔG_{H^*}), with optimal performance near thermoneutral binding ($\Delta G_{H^*} \approx 0$), as established by DFT-derived adsorption energetics and exchange-current trends [42]. For OER on oxides, descriptor-based volcano relationships emerge from scaling relations among oxygenated intermediates (*OH, *O, *OOH); in the conventional adsorbate-evolution mechanism, the near-linear scaling between OOH and OH introduces a well-

known thermodynamic bottleneck and motivates the use of descriptors such as ΔG_O - ΔG_{OH} to compare catalysts on a common activity map [69].

A critical nuance for amorphous electrocatalysts is that "a single volcano position" is often ill-defined. Unlike a crystalline facet with a small number of symmetry-equivalent adsorption sites, amorphous solids expose a statistical ensemble of local motifs (coordination environments, strained bonds, vacancies, and mixed-anion/cation neighborhoods). Consequently, adsorption thermodynamics are better represented as a distribution of descriptor values rather than a single number, and the catalytic response can be dominated by a subpopulation of near-optimal sites. This is consistent with defect arguments even for crystalline metals, where low-coordination sites can contribute disproportionately by shifting adsorption energetics toward the volcano optimum [42]. In practical terms, volcano placement of amorphous catalysts is most rigorous when reported as either (i) a mean +/- spread across representative sites generated from atomistic models (for example, melt-quench structures with site sampling), or (ii) a bounded range inferred from chemically distinct motifs exposed under operating conditions [70].

Operando reconstruction and coverage effects further "move" amorphous catalysts on the volcano map. Many amorphous and amorphous-rich precatalysts undergo potential-driven surface evolution (hydration/oxidation, anion exchange, and formation of (oxy)hydroxide skins), meaning the relevant descriptor should correspond to the active state under bias rather than the as-synthesized phase. In addition, for OER in particular, adsorption energetics can be strongly coverage-dependent: operando studies on amorphous IrO_x versus rutile IrO_2 demonstrate that increasing *O coverage weakens *O binding via repulsive adsorbate-adsorbate interactions (quantified by an interaction parameter r), thereby shifting effective binding toward the optimal descriptor region at reaction-relevant potentials [71]. This observation illustrates a broader implication for amorphous materials: higher densities of redox-active centers and flexible local coordination can increase active-state coverage, altering the effective binding energetics under operation and changing the apparent volcano position relative to a zero-coverage descriptor.

Representative amorphous case studies highlight how disorder reshapes descriptor values. For alkaline HER, direct observation of in situ surface amorphization in Ru-doped $NiPS_3$ nanosheets shows that the reconstructed amorphous layer introduces motifs that tune hydrogen adsorption into a favorable window (reported H* adsorption energies spanning approximately -0.16 to 0.35 eV across candidate sites) while also mitigating poisoning by separating H* and OH* adsorption sites; this coincides with substantially reduced η_{10} relative to the undoped analogue [72]. For engineered metallic systems, atomistic modeling of amorphized alloy/HEA surfaces similarly adopts a site-sampling approach to compute average H* adsorption free energies for amorphous versus crystalline regions, reinforcing that amorphization can measurably shift adsorption energetics through electronic-structure redistribution [70]. Collectively, these results motivate a disorder-aware use of volcano plots in amorphous electrocatalysis: rather than treating amorphousness as a qualitative label, one should relate quantified local structure (short-/medium-range order and defect chemistry) to descriptor distributions and to the reconstructed active state that is kinetically relevant under operating conditions.

1.3 Electrocatalyst Evaluation

Electrocatalyst performance is commonly assessed through several kinetic metrics, such as overpotential and Tafel slope, along with parameters like turnover frequency (TOF),

electrochemical impedance spectroscopy (EIS), electrochemical surface area (ECSA), and long-term stability.

1.3.1 Overpotential

This parameter is an essential requirement for assessing the performance of electrocatalysts in water splitting. The overpotential of an electrochemical process is the additional potential necessary to facilitate a specific electrochemical reaction at a practical rate, exceeding its thermodynamic (reversible) potential. The reversible potential for the HER is 0 V relative to the standard hydrogen electrode (SHE), whereas for the OER, it is 1.23 V relative to SHE. Consequently, the overpotentials for these two processes can be determined using the following equations, respectively [73–75]:

$$\eta_{HER} = E_{RHE} - 0\ V \quad (19)$$

$$\eta_{OER} = E_{RHE} - 1.23\ V \quad (20)$$

Resistance overpotential significantly influences the total overpotential experienced in electrochemical operations. To account for its influence, one may manually modify the recorded values by computing the product of current density and resistance acquired from the Nyquist plot derived using EIS. An alternative method involves implementing IR compensation in real-time via the electrochemical workstation during the experiment [76,77].

1.3.2 Tafel analysis

Tafel analysis is an effective technique for assessing the activity and kinetics of electrocatalytic events. It offers various critical parameters, including exchange current density (j_0), transfer coefficient (α), Tafel constant (η at unit current density, i.e., η when j = 1), and Tafel slope ($\frac{2.303RT}{\alpha nF}$). Among these, j_0 and the Tafel constant are regarded as activity descriptors, whereas the Tafel slope and α function as kinetic descriptors. Tafel slopes are frequently employed to ascertain the rate-determining step (RDS) of the reaction. The transfer coefficient (α) indicates the ease with which the reaction occurs on the surface of the electrocatalyst [78]. The Tafel equation is presented below:

$$\eta = a + b\log(j) \quad (21)$$

Where η is the overpotential, j is the current density, a/or ($\frac{2.303RT}{\alpha nF}\log(j_0)$) is the Tafel intercept, and b or ($\frac{2.303RT}{\alpha nF}$) is the Tafel slope. This connection elucidates the correlation between overpotential and current density, enhancing the comprehension of reaction mechanisms and catalytic behavior [79,80].

1.3.3 Turnover frequency

TOF is a clear and direct intrinsic activity metric that signifies the efficiency with which a catalyst promotes a certain reaction. It is defined as the quantity of reactant molecules transformed (or product molecules generated) per active site per unit of time. This measure offers significant insight into the inherent catalytic efficacy, irrespective of surface area or catalyst quantity [81]. TOF can be determined using the subsequent equation:

$$TOF = \frac{JA}{\alpha Fn} \quad (22)$$

In this context, j (mA cm^{-2}) refers to the current density of the sample at a given potential measured. A represents the surface area of the working electrode, while α denotes the number of electrons

involved per mole, accounting for both the catalyst and the desired product. F stands for Faraday's constant (96485.3 C mol^{-1}). The term n indicates the number of moles of metal present on the electrode, calculated by dividing the mass of the catalyst (m, in grams) by its molecular weight (M, in g mol^{-1}) [82,83].

1.3.4 Electrochemical impedance spectroscopy

EIS is an essential method for assessing electrocatalysts [84]. The process is applying an alternating current (AC) potential to assess the impedance (Z) of an electrochemical system, wherein Z fluctuates with frequency. Impedance denotes the correlation between voltage and current inside the system [85]. To analyze EIS data, the resulting spectra are generally fitted to an equivalent circuit model consisting of components such as resistors and capacitors. These circuit components signify fundamental physical phenomena, encompassing charge and mass transfer, double-layer capacitance, film resistance, and electrolyte conductivity [86]. By aligning the experimental results with a suitable circuit, one can derive numerical values that match to the features of these phenomena.

1.3.5 Electrochemical surface area

ECSA is a crucial metric for evaluating the inherent catalytic activity of electrocatalysts, as it represents the double-layer capacitance [87]. To ascertain the ECSA, the double-layer capacitance (C_{dl}) is initially derived via cyclic voltammetry (CV) performed within a non-Faradaic potential range [88,89]. CV curves are obtained at different scan rates, and the disparity between anodic and cathodic currents at a certain potential is graphed against the respective scan speeds. The slope of the resultant linear fit, when divided by two, provides the value of C_{dl} [90]. The ECSA can subsequently be determined using Equation 22, derived from this capacitance [91].

$$\mathrm{ECSA} = \frac{C_{dl}}{C_s} \tag{22}$$

C_s represents the standard capacitance, which is dependent upon the electrolyte's properties [92].

1.3.6 Stability

Stability is a key criterion in evaluating the overall efficacy of an electrocatalyst. Considering that electrodes frequently function under severe, reductive circumstances, it is imperative to assess both their electrochemical and morphological stability. Standard methodologies for this assessment encompass chronopotentiometry (potential versus time), chronoamperometry (current versus time), and cyclic voltammetry. Chronopotentiometry and chronoamperometry are generally performed at a steady current density or applied potential for a specified duration to assess durability. Chronopotentiometry, typically conducted at a current density of 10 mA cm^{-2}, is extensively utilized by researchers owing to its straightforwardness and informative results. The overall length of electrochemical testing depends on the particular material and testing technique employed. A crucial approach for evaluating stability involves comparing the polarization curves obtained prior to and during several cyclic voltammetry scans. High stability is demonstrated when the final curve closely aligns with the original curve or shows just a minimal rise in overpotential (often less than 10%) [93,94].

Importantly, stability in water electrolysis should be interpreted in at least two complementary ways: (i) electrochemical durability, i.e., retention of catalytic activity during chronopotentiometry/chronoamperometry and repeated cycling, and (ii) structural/chemical stability, i.e., preservation (or controlled evolution) of the catalyst composition, phase, and

interfacial integrity under strongly cathodic (HER) or anodic (OER) potentials. In many transition-metal systems, particularly amorphous phases and non-oxide catalysts, the applied bias can induce surface/bulk reconstruction, oxidation, and/or leaching, frequently yielding (oxy)hydroxide/oxide species that function as the steady-state active phase. Therefore, sustained activity does not necessarily imply that the as-synthesized amorphous structure remains unchanged; instead, it may indicate convergence toward a reconstructed active surface that is dynamically maintained under operating conditions [95–97].

Accordingly, stability claims should ideally be supported by pre-/post-test structural and compositional verification (e.g., XRD/TEM for phase/morphology, XPS for surface chemistry) and, when feasible, in situ/operando characterization to capture reconstruction pathways and the identity of the true active phase. In parallel, quantifying catalyst loss (e.g., dissolved metal via ICP-OES/ICP-MS, mass loss, or detachment from the support) helps distinguish apparent electrochemical stability from chemical corrosion/dissolution. These considerations are now widely emphasized in modern stability protocols and OER-stability analyses, because morphological/phase evolution and dissolution are often intertwined with activity trends [98–100].

1.4 Structural Designs: Amorphous

Amorphous materials are characterized by the lack of long-range crystallinity, featuring only short-range atomic arrangements and a disordered network without periodic lattice symmetry [33]. In contrast, crystalline solids display an ordered lattice structure that repeats periodically in three dimensions. This key structural difference imparts amorphous materials with a higher density of inherent defects, such as dangling bonds and coordination vacancies, and typically a greater specific surface area [20]. However, the absence of long-range order generally suppresses band-like carrier transport; thus, for many amorphous oxides/hydroxides, long-range electronic conduction can be lower than in crystalline counterparts and may proceed via localized hopping/polaronic mechanisms. In practice, high-performing amorphous electrocatalysts are therefore frequently deployed as ultrathin coatings or nanoscale domains that are electronically coupled to conductive backbones (e.g., metal foams, carbon textiles) or to crystalline/metallic phases, which provide continuous electron pathways while the amorphous component maximizes accessible active sites [27,101]. Moreover, the expanded surface area and the high number of low-coordinated sites in amorphous structures provide more active sites for catalytic reactions, generally improving reactivity [102]. In comparison, a perfectly crystalline catalyst has fewer inherent defects, and its active sites are primarily confined to its well-defined surfaces or facets [30]. Importantly, the disordered atomic structure of amorphous catalysts can also enhance charge transport and mass diffusion, as the varied pathways within the random network allow reactants and electrons to move more easily [103]. While crystalline materials usually offer superior intrinsic electronic conductivity and thermal stability due to their ordered lattices [30], they often face limited catalytic activity because only surface atoms are involved in reactions. Amorphous catalysts, by virtue of their structural disorder, overcome this limitation by enabling both surface and bulk atoms to serve as active sites, thereby enhancing the material's utilization in catalysis [104]. Table 1 summarizes the qualitative differences between amorphous and crystalline structures in the context of catalysis.

Table 1. Differences between amorphous and crystalline structures.

Aspect	Amorphous Structure	Crystalline Structure
Atomic order	No long-range order; only short-range motifs.	Periodic lattice with long-range order and defined facets.

Active site distribution	Many unsaturated/heterogeneous sites throughout bulk and surface.	Sites mainly on specific facets/edges/defects; bulk largely inactive.
Defects and disorder	High density of intrinsic defects/voids → more adsorption sites.	Fewer, localized defects in the ideal lattice.
Compositional flexibility	Broad solubility for dopants/multi-element mixing; fewer lattice constraints.	Substitution limited by lattice tolerances and fixed stoichiometry.
Electronic properties	Lower long-range conductivity; efficient local charge transfer; often needs conductive support.	Higher intrinsic conductivity (metals/semiconductors) via ordered bands.
Structural stability	Often metastable; can crystallize at elevated temperature; grain-boundary-free surfaces resist some corrosion.	Thermodynamically stable up to phase/melting transitions; grain boundaries/facets can corrode.
Morphology and surface area	Easily forms porous networks with high surface area; tunable by synthesis.	Morphology follows crystal habit; high area usually requires nanostructuring/templating.

In discussing electron transport in crystalline and amorphous structures, it is important to distinguish the intrinsic electronic/ionic transport properties of the catalyst phase from the apparent charge/mass transport of the assembled electrode. Crystalline materials often exhibit higher electron transport, whereas the lack of long-range order in amorphous phases can localize carriers and suppress band-like mobility; for many amorphous transition-metal oxides/hydroxides, electronic conduction is frequently described by localized hopping or polaronic transport. Consequently, high-performing amorphous electrocatalysts are commonly realized as ultrathin amorphous layers, or as amorphous/crystalline (or amorphous/conductive) hybrids supported on highly conductive scaffolds (e.g., metal foams, carbon cloth), which reduces contact resistance and transport distances while preserving the high density of under-coordinated active sites. Likewise, ionic transport is governed primarily by electrolyte access, porosity/tortuosity, and hydration; amorphous catalysts often appear advantageous in practice because they are frequently synthesized together with porous, gel-like, or nanosheet morphologies that shorten diffusion pathways [27,101,105].

Moreover, amorphous structural design has shown significant advantages for water-splitting catalysis, including both the HER and OER [106]. Studies have indicated that amorphous electrocatalysts often match or exceed the performance and durability of their crystalline counterparts in these reactions. This improved performance is primarily due to the structural features mentioned earlier, where the disordered atomic network results in a higher concentration of active sites and more adaptable local geometries for reactant binding and conversion [29]. In this context, subsurface atoms are more easily involved, and electrochemical bulk activation is promoted, reducing the limitations usually associated with ordered surfaces. However, it is important to mention that, amorphousness is not a universal predictor of superiority: crystalline catalysts can be favored when intrinsic conductivity and/or thermodynamic stability dominate performance, and important benchmarks exist for both acidic and alkaline OER.

Beyond enhanced activity, many amorphous catalysts exhibit bifunctional behavior (effective for both HER and OER) alongside stability [107]. Flexible bonding and the high density of defect derived reactive sites promote bias-induced surface reorganization and the formation of active oxide/oxyhydroxide layers without compromising electronic conductivity [108]. When these materials are grown directly on porous current collectors, mass and charge transport are improved

and bubble adhesion can be mitigated when the resulting surface chemistry and hierarchical roughness/porosity create favorable wetting (hydrophilic/underwater aerophobic) interfaces that shorten bubble residence time [102]. It is worth noting that, enhanced wettability and efficient bubble detachment in gas-evolving electrocatalysis are not inherent outcomes of amorphization; instead, they are chiefly dictated by surface chemistry in concert with roughness/porosity, and by gas-liquid-solid interfacial interactions coupled to electrode architecture. The apparent bubble-management benefits often associated with amorphous catalysts largely arise because typical fabrication or activation methods produce defect-rich, hydroxylated/oxidized surfaces and hierarchical 3D textures that directly promote wetting and bubble transport. Accordingly, these effects are best attributed to concomitant surface and structural features, with amorphization viewed primarily as a route to reconstruct able, defect-rich catalytic surfaces [109–112].

A further key advantage of amorphous materials is their high tolerance for multielement incorporation and the consequent tunability of active site chemistry. The absence of a rigid lattice enables doping, complex alloying, and even high-entropy strategies; this compositional freedom allows targeted modulation of the electronic structure and synergistic effects. In addition, these phases reconstruct rapidly and efficiently to their active states under operating conditions [113]. From the standpoint of durability, the lack of grain boundaries in amorphous structures mitigates common weaknesses of crystalline materials such as stress concentration, grain growth, and preferential corrosion [114]. Recent work also shows that amorphous carbon can act as a functional support to stabilize active-site distributions through anchoring/embedding/confinement effects, thereby improving durability and sometimes intrinsic activity (see Section 1.5.6, Chemistry and Key Mechanisms).

From a durability perspective, it is also important to remember that while amorphous networks may better accommodate strain and facilitate formation of catalytically competent surface layers, many amorphous catalysts (and amorphous-rich non-oxide precatalysts) undergo non-trivial in situ evolution under HER/OER operation, such as partial oxidation to (oxy)hydroxides, compositional redistribution, amorphous-to-crystalline transitions, and/or element leaching. Consequently, the long-term stability of an “amorphous catalyst” often depends less on static retention of the initial disorder and more on whether the reconstructed active layer remains electrically connected, mechanically anchored, and resistant to dissolution under the applied potential and electrolyte environment [95,96,100].

Additionally, although amorphous phases can increase site density and broaden accessible binding environments, the highest catalytic performance is often achieved when disorder is balanced with structural connectivity. In other words, the most active catalysts may not be the “most amorphous,” but those that combine defect-rich local coordination with sufficient network continuity for electron/ion transport and with robust anchoring to the current collector. This principle is consistent with reports where moderated interfaces improve electrocatalysis by coupling abundant reactive motifs to efficient transport and durability, thereby mitigating the conductivity and stability limitations that may arise in fully disordered phases [26–28].

In conclusion, amorphous structures, with their abundant active sites, flexible local geometries, defect-rich surfaces, and extensive compositional tunability, present a highly effective approach to improving both activity and stability in water splitting. As a result, amorphous materials are highly suitable for application in practical water-splitting processes.

1.5 Amorphous Structures and Synthesis Strategies

Amorphous structures, characterized by the lack of long-range crystalline order and the presence of voids, possess a range of properties that make them highly attractive electrocatalysts. These include a high density of electron-rich and electron-deficient centers that provide abundant active sites, extensive pore networks that improve the adsorption and confinement of reactants or gaseous intermediates, and efficient surface charge transfer that facilitates in situ/operando reconstruction into highly active surface phases [115].

To harness these advantages, various synthesis methods have been developed to optimize structure and performance. Direct routes build amorphous frameworks from the ground up: electroless deposition [116] creates uniform metal/alloy coatings without external bias; pulsed electrodeposition [117] allows precise control over nucleation and growth for thin amorphous films; colloidal synthesis [118] produces nanoparticles with adjustable size and composition; and chemical reduction [119] forms amorphous nanoparticles or hybrids from metal salts under controlled conditions.

Indirect routes transform preformed crystalline or molecular precursors into disordered phases, including thermal decomposition [120] of metal thiolates or oxides, electrochemical activation [121] that induces surface disorder and creates amorphous active layers, and selective leaching/etching to develop high-surface-area architectures. Together, these techniques enable precise control over factors like active-site density, electronic conductivity, particle size, and morphology, all crucial for optimizing amorphous electrocatalysts for HER, OER, and water splitting. This section provides a comprehensive overview of the main types of amorphous structures and the synthesis strategies used to produce them.

1.5.1 Amorphous Transition Metal Phosphides (a-TMPs)

1.5.1.1 Chemistry and Key Mechanisms

a-TMPs possess both positive and negative polarized centers, which create favorable active sites for catalytic interactions. The positively charged centers ($M^{\delta+}$) arise from the transition metal atoms, whereas the negatively charged centers ($P^{\delta-}$) originate from phosphorus. This intrinsic polarity underpins their electro catalytic activity. During the HER, $P^{\delta-}$ sites readily adsorb proton species ($H^{\delta+}$), while adjacent metal centers stabilize the resulting hydride intermediates ($M\text{-}H^{\delta+}$). This heterolytic pathway for H_2 generation closely resembles the catalytic mechanism of hydrogenase enzymes in nature. Moreover, the coexistence of polar centers facilitates metal oxidation under anodic potentials, thereby leading to the in-situ formation of surface (oxy) hydroxide layers, which serve as highly active OER sites [122,123].

Extensive studies on multi metallic phosphides, such as Ni-Fe-P systems, have revealed that during OER, certain metals (most notably Fe) undergo preferential oxidation and leaching. This process progressively weakens the M-P bonds and ultimately induces the formation of thin, porous (oxy) hydroxide layers (e.g., NiFeOOH) on the catalyst surface. Consequently, the original phosphide phase functions as a pre catalyst**,** undergoing structural reconstruction to yield the true catalytically active species [124].

1.5.1.2 Synthesis of Amorphous Transition Metal Phosphides

Electroless deposition has proven to be an effective method for directly synthesizing amorphous metal-phosphide coatings, owing to its simplicity, precise control over metal composition, and versatility in substrate selection. These coatings have demonstrated strong performance in electrochemical applications, especially for HER and OER. The first systematic study on electroless deposition for producing amorphous Ni-P films was conducted by Pearlstein and

Weightman in 1963 [116] . In this method, sodium hypophosphite (NaH_2PO_2) acts as a reducing agent, converting Ni^{2+} ions to metallic nickel while incorporating phosphorus into the film, resulting in a uniform amorphous structure. The process is self-catalyzing, meaning the initially deposited nickel facilitates further deposition on the substrate. This pioneering work laid the foundation for numerous subsequent studies on amorphous catalysts, corrosion-resistant coatings, and electrochemical electrodes, highlighting the importance of electroless deposition for creating amorphous phosphide materials. Amorphous Co-P coatings were electrolessly deposited on copper substrates as shown in Figure 4a, demonstrating that the phosphorus content critically affects overpotential and catalytic activity for both HER and OER. Increasing phosphorus content improved stability and lowered overpotential [125]. In this study, electroless deposition was used to prepare Co-P/Cu catalysts, where 11 wt% P optimized HER performance, 8 wt% P optimized OER, and the Co-P11/Cu electrode achieved 1.813 V at 10 mA/cm².

Additionally, the Ni-Fe-P-WO_3/NF atalyst was fabricated on nickel foam using a straightforward electroless deposition method. This process generated a uniform amorphous Ni-Fe-P layer embedded with WO_3 nanoparticles, resulting in a hybrid nanostructured, multiphase architecture. The synergy between the amorphous framework, plentiful active sites, and efficient mass transfer substantially improved OER performance [126].

In addition, Ni-P alloys with different phosphorus contents were synthesized. Film formation occurs through an autocatalytic reduction process on the nickel surface, where Ni^{2+} ions are reduced by electrons from the reducing agent, sodium hypophosphite (NaH_2PO_2), resulting in zero-valent phosphorus and H_2 as by-products. as by-products. SEM images in Figure 4(b,c) showed that the Ni-P films are uniform, with grain sizes smaller than 10 nm, and the observed pinholes are attributed to hydrogen evolution during deposition. This amorphous nanostructure enhances the density of active sites, improving electrocatalytic performance. Post-OER analysis also revealed significant surface changes that impact catalyst activity. Furthermore, controlling the Ni/P ratio and the thickness of the amorphous Ni-P layers on nickel foam was found to reduce overpotential and boost the turnover frequency (TOF), emphasizing the importance of precise compositional and structural tuning for achieving optimal OER performance [127].

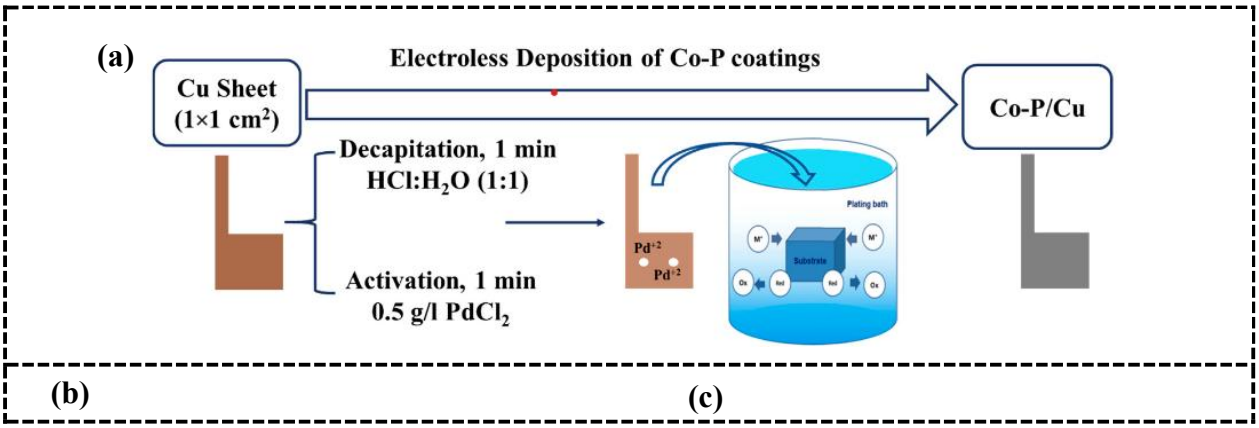

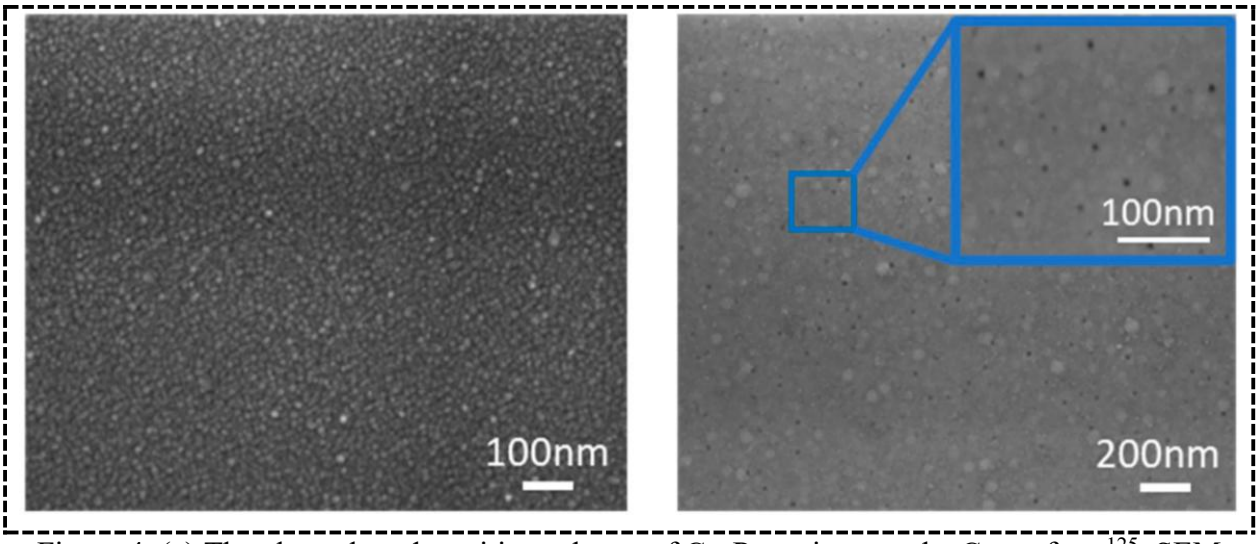

Figure 4. (a) The electroless deposition scheme of Co-P coatings on the Cu surface [125]; SEM images of (a) Ni substrate and (b) Ni-P deposited for 6 min [127].

Overall, electroless deposition offers a simple, cost-effective, and versatile method for directly synthesizing amorphous phosphide coatings with controlled composition and morphology. This approach facilitates the creation of high-performance HER and OER electrocatalysts by integrating structural uniformity, a high density of active sites, and improved mass transfer.

In addition to electroless deposition, amorphous nanostructured phosphides can also be synthesized via pulse electrodeposition. Using this method, the Moloudi research group prepared a Ni-Co-Fe-P (NCFP) electrocatalyst by applying rapid potential pulses (Figure 5a). Alternating current/voltage pulses promote nucleation over crystal growth, resulting in amorphous metal phosphides with uniform morphology and a phosphorus-rich composition. Such amorphous structures provide abundant active sites, reduce electrode resistance when electronically well-coupled to the current collector (and/or when doped to introduce more conductive pathways), leading to superior electrocatalytic performance [128]. The electrolyte contained Ni^{2+}, Co^{2+}, and Fe^{2+} ions along with a phosphorus source (e.g., NaH_2PO_2) in an alkaline or buffered medium. Short voltage pulses, consisting of on and off periods, were applied to the electrode, enabling the simultaneous deposition of metals and phosphorus. The limited time for atomic arrangement favored the formation of a nanostructured amorphous film. Pulse parameters, including voltage, on/off durations, and number of cycles, were optimized to control film thickness and surface loading.

Thanks to its high surface area and amorphous structure, this electrocatalyst exhibited excellent activity not only for the HER but also for the OER, making it suitable for sustainable energy applications such as water electrolysis and Zn-Air batteries (Figure 5b).

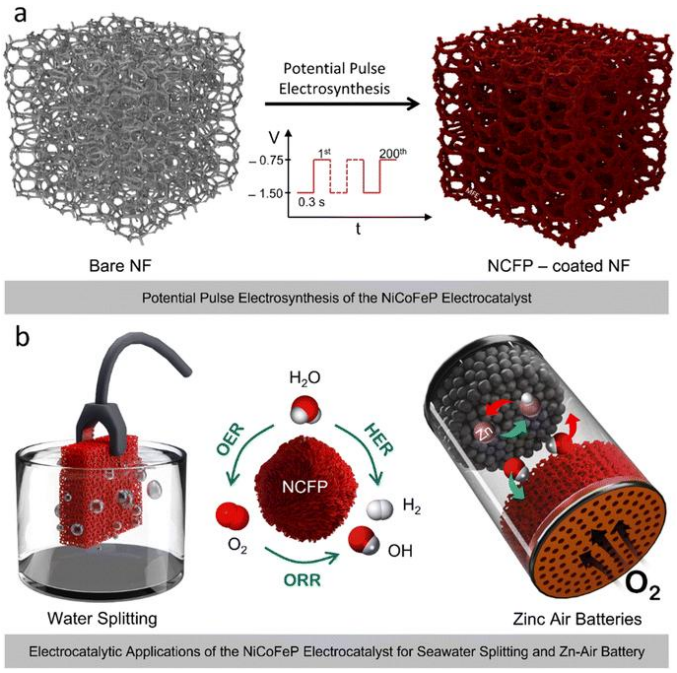

Figure 5. Schematic illustration of the electrosynthesis of the NCFP electrocatalyst and its applications. (a) Electrosynthesis of the NCFP elec-trocatalyst that lasts for just 2 min (b) illustration of the practical application of the multifunctional NCFP electrocatalyst for overall (sea)water splitting and zinc–air batteries [128].

Building on pulse electrodeposition approaches, the JO research group prepared Ni-P films using a pulse-reverse electrodeposition technique. The synthesis mechanism involves the reduction of H^+ ions to adsorbed hydrogen, which then reacts with H_3PO_3 to produce PH_3, followed by the simultaneous deposition of Ni and P on the electrode surface. By adjusting the duty cycles, the phosphorus content in the Ni-P alloy could be precisely controlled, and subsequent annealing led to the formation of crystalline Ni_3P with pure Ni particles. This precise control over composition and structure improved the electrochemical behavior and enhanced the catalyst's stability during hydrogen evolution. Ultimately, the crystalline Ni_3P/Ni composite demonstrated excellent performance as a stable and efficient hydrogen evolution catalyst [117].

Moreover, the colloidal method allows the synthesis of uniform metal phosphide nanostructures through surfactant-assisted growth in solution. This approach provides precise control over particle size and morphology while maintaining high dispersion. The resulting nanophosphides possess abundant accessible active sites, making them efficient catalysts for HER and OER.

In a study by the Kang group, amorphous molybdenum phosphide (MoP) nanoparticles were synthesized via the colloidal method to enhance catalytic performance for the HER, and two synthetic routes, the one-pot and two-step methods, were compared [129]. In the two-step method, Mo nanoparticles were first formed by heating $Mo(CO)_6$ in the presence of ODE and oleylamine at 230 °C, and then injected into an activated TOP solution in squalane at 320 °C to form MoP. In the one-pot method, all precursors and solvents were mixed in a single vessel and heated directly to 320 °C. Both methods produced amorphous nanoparticles with sizes of 3.9-4.1 nm, but the two-step synthesized NPs exhibited higher HER activity (overpotential = 177 mV versus 208 mV for the one-pot method), which was attributed to a higher P/Mo ratio, more Mo-P bonds, and lower surface oxidation.

This study highlights that the choice of synthetic method and careful control of reaction conditions play a crucial role in optimizing the morphology, elemental composition, and electrochemical performance of metal phosphide nanoparticles.

1.5.1.3 Characterization of Amorphous Metal Phosphides

Understanding the structural, morphological, and local chemical properties of amorphous metal phosphides is essential to correlate synthesis strategies with electrocatalytic performance. Various complementary techniques provide insight into the amorphous structure, but each has inherent limitations that must be considered together.

X-ray diffraction (XRD) is commonly used to confirm the absence of long-range crystalline order. For example, Co-P coatings prepared via electroless deposition showed broad, low-intensity features without sharp peaks, indicating an amorphous phase up to 11 wt % phosphorus [125]. Similarly, Ni-Co-Fe-P (NCFP) films produced by pulse electrodeposition displayed only diffuse patterns, demonstrating preserved amorphous structure despite multiple metal components [128]. While XRD effectively identifies amorphousness and can monitor phase evolution upon annealing, it provides limited information about short-range atomic arrangements, which are critical for active site formation.

Transmission electron microscopy (TEM) complements XRD by revealing nanoscale morphology, particle size, and dispersion. TEM images of Co-P films showed dense, uniform films on Cu substrates [125], while NCFP samples exhibited ~30 nm spherical particles and porous textures enhancing surface area [128]. MoP nanoparticles synthesized by colloidal methods measured 3.9-4.1 nm [129]. Despite providing direct visual evidence of particle morphology and connectivity, TEM represents only localized regions and may not fully capture bulk uniformity, with potential sample preparation artifacts.

X-ray absorption spectroscopy (XAS/EXAFS) probes the local atomic environment, providing bond lengths, coordination numbers, and oxidation states even in amorphous networks. EXAFS analysis of Co-P revealed Co-P coordination critical for HER/OER activity [125], and in NCFP, XAS distinguished local environments around Ni, Co, and Fe, clarifying how phosphorus incorporation alters electronic structure [128]. While powerful, EXAFS requires careful modeling and cannot provide direct imaging.

Raman spectroscopy offers complementary information by probing vibrational modes and short-range bonding. In Ni-Fe-P-WO_3/NF and NCFP, Raman spectra indicated phosphorus incorporation and local structural heterogeneity [126,128]. Although interpretation can be complicated by overlapping peaks and limited spatial resolution, Raman helps connect local bonding to catalytic behavior where XRD lacks resolution. Combining these techniques provides a comprehensive picture of structure-property relationships. These examples underscore that the combination of XRD, TEM, EXAFS/XAS, and Raman is essential to understand how amorphous short-range order, morphology, and local bonding collectively govern catalytic behavior.

1.5.2 Amorphous Transition Metal Borides (a-TMBs)

1.5.2.1 Chemistry and Key Mechanisms

Boron (B), with lower electronegativity compared to phosphorus, tends to form stronger covalent and electron-donating bonds with metals. Due to the availability of vacant orbitals, boron can facilitate electron circulation and transfer from the metal center into these orbitals, thereby intensifying regions of positive or negative potential. This process optimizes hydrogen adsorption

energies, which is critical for the HER. Similar to phosphides, borides undergo in situ surface reconstruction under OER conditions, leading to the formation of metal (oxy) hydroxides coated with a borate layer [130,131]. The reconstructed phase serves as the actual catalytic active site for OER. Moreover, in borate-containing electrolytes, –B (OH)x groups can function as proton buffers, thereby enhancing the reaction kinetics [130,132,133].

1.5.2.2 Synthesis of Amorphous Transition Metal Borides

Parakh and colleagues synthesized metal nanoparticles coated with an amorphous NiB or CoB shell using a colloidal method. In this approach, metal nanoparticles such as Au and Pd were first prepared in a stable colloidal solution, after which a thin amorphous NiB or CoB layer was deposited onto their surfaces by adding chemical precursors. The aim was to enhance the stability of the nanoparticles and prevent their aggregation while maintaining the catalytic activity of the metal core. The study highlighted that these nanoparticles are suitable for various catalytic applications, including electrochemical reactions. The colloidal method was emphasized as a major advantage due to its simplicity, precise particle size control, and uniform coating capability [119].

Li and colleagues synthesized a-TMBs via a chemical reduction method to develop cost-effective and efficient alternatives to platinum catalysts for photocatalytic water splitting. The main goal was to produce catalysts with less than 0.1% platinum content while maintaining high hydrogen generation performance [134].

Quantum mechanical calculations indicated that TMBs adsorb protons more readily and release hydrogen molecules faster than platinum. Their amorphous, nanostructured nature, combined with the presence of graphene, enhances surface dispersion and accessibility. Spectroscopic studies including PL, SPS, and EPR confirmed that TMBs act as “electron sinks,” reducing electron-hole recombination and improving photocatalytic efficiency. Overall, amorphous transition metal borides synthesized via chemical reduction and the Santer Amorphous method serve as stable, inexpensive, and effective alternatives to platinum catalysts for photocatalytic hydrogen production.

Building on earlier research on amorphous transition metal borides, Wang’s research group [135] synthesized metallic NiFe-boride as a precursor, which was then in situ transformed under OER conditions into NiB_4O_7 and $FeBO_3$ phases. These resulting phases form the active amorphous structure of the catalyst and play a crucial role in facilitating the *O → *OOH steps, thereby improving electrocatalytic activity. DFT calculations revealed that NiB_4O_7 has the lowest overpotential and acts as the primary active site. Further coupling mechanism analyses and advanced activity descriptors confirmed that the incorporation of boron leads to the formation of new active phases, significantly boosting OER performance.

The oxygen evolution reaction (OER) on the NiFe catalyst follows a four-electron mechanism, and DFT calculations were conducted to assess the reaction energies and identify the active sites of the in-situ formed NiB_4O_7 and $FeBO_3$ phases. This study clearly shows that boride-derived (indirect) synthesis is a highly effective and robust method for producing high-performance amorphous catalysts.

Overall, these synthetic strategies highlight the versatility of amorphous transition metal borides. Colloidal and chemical reduction methods allow precise control over particle size, morphology, and surface composition, enhancing both catalytic activity and stability. Boride-derived in-situ

transformations further generate active amorphous structures that optimize reaction pathways and electrocatalytic performance. Together, these strategies underscore the potential of a-TMBs as cost-effective, stable, and high-performance catalysts for a wide range of electrochemical and photocatalytic applications.

1.5.2.3 Characterization of Amorphous Transition Metal Borides

Comprehensive structural and spectroscopic analyses provide crucial insights into how the amorphous structure, nanoscale morphology, and local bonding of transition metal borides determine their electrocatalytic performance. Multiple complementary techniques are typically employed, each offering distinct information while having inherent limitations.

XRD confirms the absence of long-range crystalline order in a-TMBs. NiB and CoB shells synthesized via colloidal deposition show broad, featureless XRD patterns, indicating their amorphous nature even when coated on metallic cores such as Au or Pd [119,134]. Similarly, NiFe-boride precursors transformed in situ during OER conditions produce diffuse XRD features consistent with amorphous NiB_4O_7 and $FeBO_3$ phases [135]. Although XRD effectively distinguishes amorphous from crystalline phases and tracks phase evolution, it provides limited information on short-range atomic arrangements, which are critical for understanding active sites.

TEM complements XRD by revealing particle size, morphology, and coating uniformity. TEM images of NiB and NiCoB nanoparticles show homogeneous amorphous shells surrounding metallic cores, with selected-area electron diffraction (SAED) confirming the lack of long-range order (Figure 6) [134]. NiFe-boride-derived catalysts exhibit nanoscale connectivity and uniform dispersion that enhance surface accessibility and mass transport [135]. While TEM provides direct visualization of morphology, it represents localized regions and may not capture bulk sample uniformity, and sample preparation can introduce artifacts.

Spectroscopic techniques provide further insight into local bonding and electronic structure. Photoluminescence (PL), surface photovoltage spectroscopy (SPS), and electron paramagnetic resonance (EPR) applied to NiB and NiCoB reveal their role as "electron sinks," reducing electron-hole recombination and enhancing photocatalytic hydrogen evolution [134]. These measurements, along with DFT calculations for NiFe-boride-derived catalysts, show that NiB_4O_7 acts as the primary active site during OER, providing the lowest overpotential and facilitating the four-electron reaction pathway [135]. While these techniques offer detailed local information, interpretation can be complex and they do not provide direct morphological imaging.

Integrating XRD, TEM, and spectroscopic analyses provides a comprehensive understanding of the structure-property relationships in a-TMBs. For example, NiB and NiCoB nanoparticles synthesized via colloidal or chemical reduction methods exhibit uniform amorphous shells that stabilize the metallic cores while maintaining high surface accessibility, enabling efficient hydrogen evolution even with <0.1 wt % Pt [134]. NiFe-boride-derived catalysts form amorphous NiB_4O_7 and $FeBO_3$ phases under OER conditions, achieving low overpotentials and high density of active sites, reflecting the combined effects of amorphous structure, nanoscale morphology, and boron incorporation [135].

Overall, the combination of complementary characterization techniques, XRD for phase identification, TEM for morphology, and PL/SPS/EPR or DFT for local bonding and electronic properties, allows a detailed understanding of how amorphous structure, particle uniformity, and boron chemistry govern the electrocatalytic and photocatalytic performance of a-TMBs. This

integrated approach emphasizes the versatility, stability, and high catalytic efficiency of amorphous transition metal borides

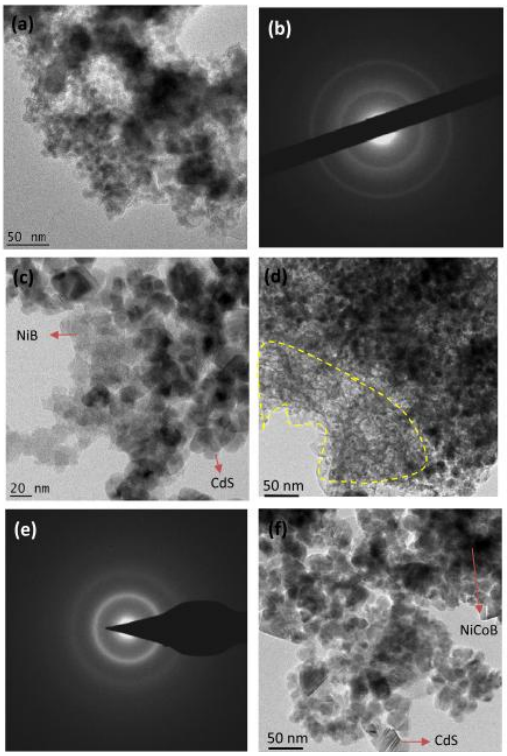

Figure 6. TEM image of the NiB products. (b) The corresponding SAED image for the NiB sample. (c) TEM image of the NiB/CdS nanocomposite. (d) TEM image of the NiCoB sample. (e) The corresponding SAED image for NiCoB. (f) TEM image of the NiCoB/CdS nanocomposite [134].

1.5.3 Amorphous Oxides and Hydroxides

1.5.3.1 Chemistry and Key Mechanisms

LOM (lattice oxygen mechanism)-based catalysts possess distinct properties that make them excellent candidates for the OER. The strong covalent metal-oxygen bonds in these catalysts give rise to a unique electronic configuration that facilitates efficient orbital hybridization, positioning the O-2p band near the Fermi level. Notable advantages include a low enthalpy of oxygen vacancy formation, reduced charge transfer energy, and the capacity to directly activate lattice oxygen. These characteristics overcome the theoretical limitations of the conventional adsorbate evolution mechanism, enabling an overpotential below 370 mV. Furthermore, LOM-based catalysts demonstrate high intrinsic activity, fast reaction kinetics, and remarkable electrochemical stability. Despite these strengths, challenges such as dynamic surface reconstruction and long-term durability remain, requiring further thorough investigation [136].

1.5.3.2 Synthesis of Amorphous Oxides and Hydroxides

Amorphous metal oxides and hydroxides are typically synthesized through solution-based chemical methods that allow precise control over metal ratios and the preservation of amorphous structures.

In the sol-gel method, metal precursors are dissolved in a solvent and undergo controlled hydrolysis and gelation. Gentle drying, such as vacuum drying at low temperatures, preserves the amorphous structure and ensures uniform metal distribution, providing structural flexibility during electrochemical reactions [137]. Moreover, Qiu et al. synthesized amorphous NiFeCo and NiFeMo oxyhydroxides via a sol-gel approach under ambient conditions. Controlled hydrolysis and rapid gelation using propylene oxide, followed by mild vacuum drying, maintained the amorphous framework. The resulting NiFeCo catalyst exhibited high structural flexibility and enhanced OER performance.

Co-precipitation and hydrothermal methods involve precipitating metal ions under controlled pH and temperature conditions, often yielding porous amorphous structures with high electrochemical surface areas. For example, a one-step hydrothermal method was used to synthesize amorphous nickel-iron oxide, achieving efficient OER performance with low overpotential [138].

Tao et al. reported the synthesis of amorphous MoO_2 with a porous nanostructure via a hydrothermal route [139]. Ammonium heptamolybdate and thiourea were dissolved in deionized water, followed by addition of OM and OA. The mixture was transferred to a Teflon-sealed autoclave and heated at 200 °C for 6 h. After cooling, the product was collected by centrifugation and washed with cyclohexane and ethanol. The resulting amorphous and porous MoO_2 exhibited a high surface area, abundant active sites, and loss of crystallinity, enhancing both HER and OER activity.

Electrodeposition enables the direct formation of amorphous oxides or hydroxides on electrode surfaces under an applied potential, creating high surface area active layers with abundant catalytic sites [140]. Ding et al. reported an in-situ electrochemical approach for synthesizing amorphous metal hydroxide microarrays with rich defects to enhance OER activity [141]. Leaflike CoM-ZIF-L precursors were grown uniformly on nickel foam via simple impregnation (Figure 7). Cyclic voltammetry (CV) induced ligand substitution of 2-methylimidazole by OH^- ions and activated the reversible redox of Co ions, forming defective amorphous metal hydroxides. The resulting $aCo(OH)_2$-ZIF-L/NF arrays exhibited abundant oxygen vacancies, high conductivity, short ion diffusion paths, and numerous catalytic sites, all contributing to improved OER performance.

.

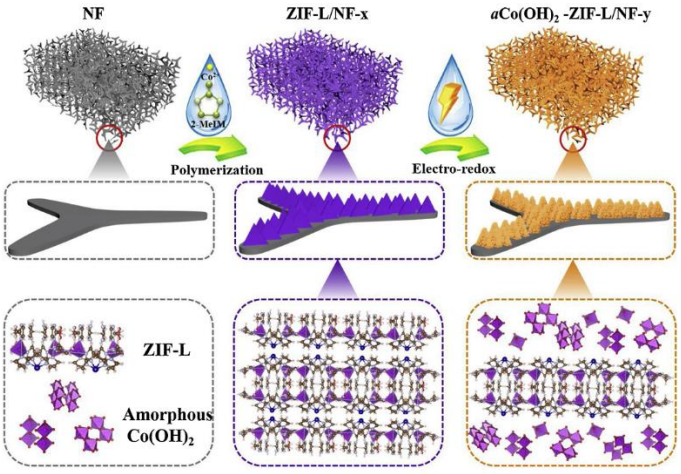

Figure 7. Schematic illustration of the synthesis and structure of ZIF-L/NF-x and aCo(OH)$_2$-ZIF-L/NF-y [141].

Building on the previously described synthetic strategies, post-treatment or structural reconstruction of pre-catalysts has emerged as a widely employed approach for producing amorphous oxide and hydroxide electrocatalysts. In this method, metallic or metal–oxide precursors, whether crystalline or semi-amorphous, are subjected to electrochemical or thermal treatments, resulting in structural reconstruction. This process generates amorphous phases with abundant defects, high surface area, and improved accessibility for ions and electrons. Representative materials include NiFe-borate, CoFe-borate, NiFe-(oxy)hydroxide, and amorphous MoO_x, all of which exhibit high catalytic activity in OER and HER. Post-treatment strategies provide enhanced stability, optimized surface activation, and structural flexibility during electrochemical operation, enabling efficient use of non-noble catalysts [142,143].

Xia et al. [142] further investigated structural reconstruction under electrochemical conditions, demonstrating that the process is influenced by both thermodynamic and kinetic factors. Thermodynamically, the electrode potential and two-phase equilibrium determine the likelihood of reconstruction, while kinetically, the electron transfer rate between oxidation and reduction centers governs the reconstruction rate. This method results in the formation of new amorphous phases with lower free energy and a larger active surface area, thereby enhancing electrocatalytic performance in reactions such as OER and HER. The study offers a conceptual framework and analytical tools for predicting and controlling catalyst reconstruction.

Overall, the diverse synthetic strategies for amorphous metal oxides and hydroxides highlight their exceptional versatility in controlling structure, composition, and surface properties. Sol-gel and hydrothermal methods allow for precise adjustments of metal ratios, particle size, and porosity, all while preserving the amorphous framework, thus improving catalytic activity. Electrodeposition generates high-surface-area, defect-rich amorphous layers on electrodes, promoting efficient charge and mass transport. Post-treatment and structural reconstruction of pre-catalysts further yield new amorphous phases with abundant defects, high surface area, and enhanced ion and electron accessibility, leading to superior OER and HER performance [137,142]. Together, these strategies provide robust, stable, and high-performance amorphous oxide and hydroxide catalysts, ideal for a wide range of electrochemical energy conversion applications, including overall water splitting.

1.5.3.3 Characterization of Amorphous Oxides and Hydroxides

NiFeCo and NiFeMo oxyhydroxides prepared via sol-gel methods exhibit broad, featureless XRD patterns, confirming their amorphous structure [137]. TEM images reveal nanosheets with thicknesses of ~5-8 nm and lateral dimensions of 50-100 nm for NiFeCo, forming a porous network that enhances ion diffusion and active site accessibility [137]. Hydrothermally synthesized NiFe oxides form mesoporous nanoflakes, while porous MoO_2 nanoparticles reach surface areas of ~120 m^2/g, contributing to high HER and OER activity [138,139].

Electrodeposited NiFeCo and NiFeCoP layers show defect-rich amorphous structures generated via CV-induced ligand exchange and surface hydroxylation, correlating with overpotentials of 280-320 mV at 10 mA cm^{-2} for OER [140,141]. EPR and XAS analyses indicate abundant oxygen vacancies and undercoordinated metal sites that act as active centers, while post-treatment or structural reconstruction produces new amorphous phases with enhanced active site density and surface accessibility, lowering overpotentials and improving catalytic performance [142,143].

Together, these results demonstrate that precise control of composition, morphology, porosity, and defect sites in amorphous oxides and hydroxides directly governs their electrocatalytic activity.

The combination of XRD, TEM, and spectroscopic analyses reveals how structural disorder and nanoscale features optimize ion/electron transport and active site availability, explaining the superior OER and HER performance of these materials.

1.5.4 Amorphous Sulfides

1.5.4.1 Chemistry and Key Mechanisms

Amorphous metal sulfides (a-MS_x) are materials composed of metal sulfide compounds, but instead of exhibiting a regular crystalline lattice, they possess an amorphous structure. This structural disorder generates asymmetric and unsaturated active sites, which often demonstrate superior catalytic activity compared to their crystalline counterparts. In contrast to ordered structures, a-MS_x offer a higher density of active sites, larger specific surface area, enhanced ion and electron mobility across disordered boundaries, and greater chemical flexibility.

In terms of their catalytic mechanism in water-splitting reactions, it has been established that amorphous sulfides contain numerous edge sites and under coordinated metal centers. These sites exhibit a strong affinity for proton (H^+) adsorption, thereby facilitating the generation of adsorbed hydrogen intermediates (H*). The amorphous state, owing to its diverse metal-sulfur bonding environments, provides sites with H* adsorption energies comparable to those of metallic systems. This is attributed to the increased negative charge localized on sulfur, stemming from the electronegativity difference between the metal and sulfur, which forms a heterogeneous active network with abundant sites for hydrogen adsorption and recombination. Furthermore, during oxygen evolution reactions (OER), a-MS_x are readily converted into amorphous oxides or ox hydroxides (M–OOH or M–O_xH_y) under anodic potentials. Such dynamic and reversible phase transitions occur more easily in amorphous phases compared to crystalline structures, representing a distinct advantage of amorphous sulfides in electro catalytic water splitting [144–146].

1.5.4.2 Synthesis of Amorphous Sulfides

Amorphous metal sulfides (a-MS_x), such as MoS_2, WS_2, and CoS_x, are synthesized via several strategies depending on the desired morphology and application. For powder materials, colloidal synthesis is widely used, providing control over particle size and morphology, which is crucial for catalytic applications. Thermal decomposition of metal precursors is another common approach for producing high purity amorphous sulfides. For electrode coatings, electroless deposition offers a simple route to form uniform films on complex geometries [120,147]. Additionally, pulsed electrodeposition allows precise control over film thickness and composition, further enhancing electrocatalytic performance. These methods are valued for their scalability, efficiency, and versatility across technological applications.

Ma and colleagues synthesized amorphous MoS_2/RGO hybrid nanoflowers through a direct colloidal hydrothermal method (Figure 8) [148]. In this approach, a graphene oxide suspension was mixed with molybdenum and sulfur precursors ($(NH_4)_4Mo_7O_{24}.4H_2O$ and CH_4N_2S), stirred, and sealed in a Teflon-lined autoclave at 250 °C for 2 hours. After washing and drying, the product consisted of 3D nanoflowers formed by few-layer MoS_2 nanosheets assembled on RGO. The amorphous structure, with stepped edges and basal plane cracks, provides abundant catalytically active sites. Coupling with RGO enhances electronic conductivity, while the 3D architecture ensures short charge transport paths, high surface to volume ratio, and mechanical stability. Consequently, these hybrid nanoflowers exhibit outstanding activity and durability for the HER

across a wide pH range, representing a successful strategy to optimize nanoscale architecture and electronic properties for next generation HER catalysts.

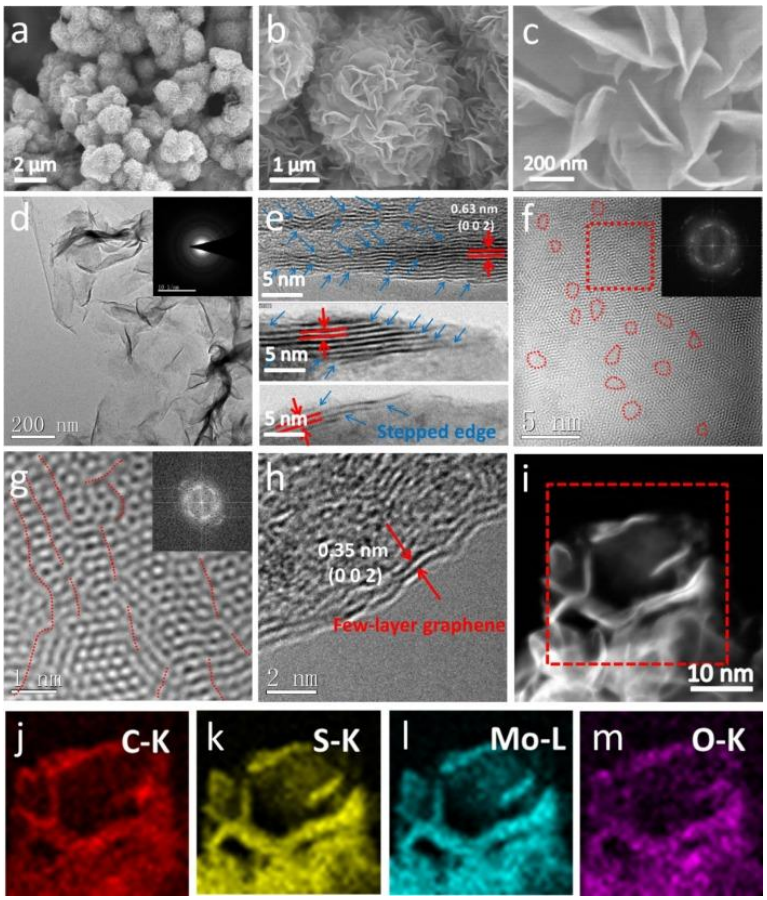

Figure 8. (a-c) SEM images of A-MoS_2/RGO NFs, (d) TEM image of A-MoS2/RGO NFs, the inset is the SAED of A-MoS_2/RGO NFs, (e) HRTEM image of the side view ofA-MoS_2/RGO NFs, (f, g) HRTEM images of the top view of A-MoS_2/RGO NFs, (h) HRTEM image of the edge of the RGO nanosheet, (i-m) STEM-EDX elemental mapping images of A-MoS_2/RGO NFs [148].

As another representative case, Kornienko et al. reported the synthesis of amorphous cobalt sulfide films via pulsed electrodeposition [149]. In this method, Co^{2+} ions and thiourea were dissolved in a neutral phosphate buffer solution, and CV sweeps were applied to deposit the film onto conductive substrates. A typical voltammogram shows an anodic peak at −0.3 V versus Ag/AgCl, a cathodic peak at -0.5 V versus Ag/AgCl, and a cathodic current at potentials more negative than −0.7 V, which increases with increasing number of CV cycles. Electrochemical double-layer capacitance measurements indicate that the amorphous cobalt sulfide film after 5 and 15 CV cycles possesses a surface area 8 and 23 times higher than the bare FTO substrate (Figure 9(a-c)). The deposited film exhibits a reflective black appearance, and SEM images reveal a rough, cracked surface (Figure 9d).

The deposition process yields a porous amorphous film composed of small oxide and sulfide clusters, as confirmed by SEM, XPS, and SAED analyses. Upon cathodic polarization during the hydrogen evolution reaction, the initially disordered CoS_x transforms into CoS_2-like clusters, exposing a high density of catalytically active sulfur edge sites. Operando Raman and X-ray

absorption spectroscopy further revealed that these clusters preferentially expose sulfur atoms to the electrolyte, in contrast to bulk crystalline CoS_2, thereby enhancing catalytic activity. Benefiting from its amorphous nature and the dynamic structural transformation under operating conditions, the electrodeposited amorphous cobalt sulfide catalyst achieved low overpotentials and excellent durability for the HER in neutral electrolyte, highlighting electrodeposition as a scalable and versatile method for fabricating amorphous chalcogenide electrocatalysts [149].

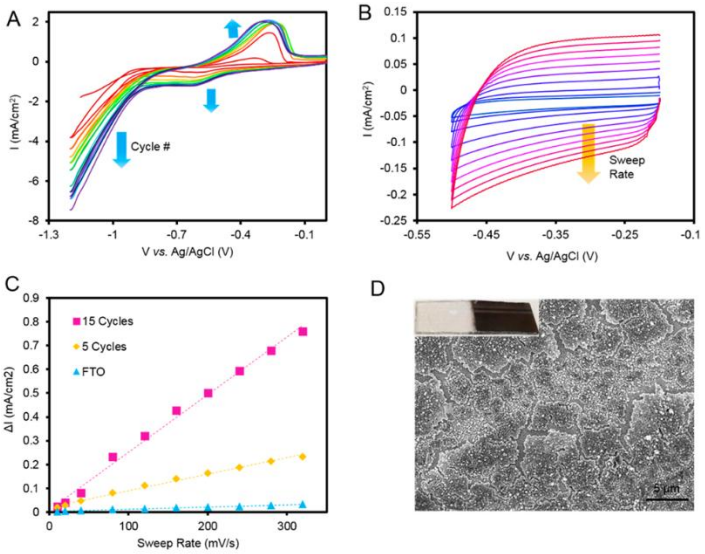

Figure 9. CoSx catalyst is electrodeposited through a series of CV sweeps (A) A typical voltammogram shows an anodic peak at -0.3 V versus Ag/AgCl, a cathodic peak at -0.5 V versus Ag/AgCl, and acathodic current at potentials more negative than -0.7 V versus Ag/AgCl, which increases with increasing number of CV cycles. Electrochemical double layer capacitance (B and C) indicates that the CoS_x film after 5 and 15 cycles of electrodeposition possesses a surface area of 8 and 23 times higher than the bare FTO substrate. An SEM image of the CoS_x film (d) shows a rough, cracked surface. Optically, the film has a reflective black appearance (inset) [149].

Overall, amorphous chalcogenides exhibit abundant active sites, enhanced conductivity, and structural flexibility, making them highly efficient HER and OER electrocatalysts. Their synthesis via colloidal, hydrothermal, and electrodeposition methods allows precise control over composition and morphology, enabling robust performance in water-splitting applications [120,147,149].

1.5.4.3 Characterization of Amorphous Metal Sulfides

Amorphous MoS_2, WS_2, and CoS_x prepared via colloidal, hydrothermal, or electrodeposition methods display broad, featureless XRD patterns, confirming their lack of long-range crystalline order [128, 129]. TEM and SEM analyses reveal nanoscale morphologies optimized for catalytic activity. For instance, amorphous MoS_2/RGO hybrid nanoflowers synthesized via colloidal hydrothermal reaction exhibit few-layer MoS_2 nanosheets assembled into 3D nanoflowers on RGO, with stepped edges and basal plane cracks providing abundant active sites and high surface-to-volume ratio (Figure 8) [148].

Electrodeposited CoS_x films formed via pulsed CV sweeps show rough, cracked surfaces and porous structures composed of small oxide and sulfide clusters. SEM, SAED, and XPS confirm the amorphous nature of these clusters, while operando Raman and XAS reveal dynamic structural

transformation under cathodic polarization, forming CoS_2-like clusters with exposed sulfur edge sites (Figure 9) [149]. Electrochemical double-layer capacitance measurements indicate that the surface area of CoS_x after 5 and 15 CV cycles increases 8- and 23-fold compared to bare FTO, correlating with enhanced HER performance [149].

These amorphous sulfides combine high density of active sites, enhanced electronic conductivity, and structural flexibility. The dynamic reorganization of CoS_x under reaction conditions further maximizes exposure of catalytically relevant sites. Similarly, MoS_2/RGO hybrids benefit from conductive supports and 3D architectures, shortening charge transport paths and improving mechanical stability [147].

Overall, the integration of TEM, SEM, XPS, SAED, and operando spectroscopies provides a detailed understanding of the structure-property relationships in amorphous metal sulfides. These analyses show how amorphous structure, nanoscale morphology, and defect-rich surfaces govern electrocatalytic activity. Controlled synthesis through colloidal, hydrothermal, and electrodeposition methods allows precise tuning of composition and morphology, enabling robust and efficient HER and OER performance for water-splitting applications.

1.5.5 Amorphous Multi Element Compositions

1.5.5.1 Chemistry and Key Mechanisms

Modern electrocatalysis has experienced a fundamental shift, driven by the integration of theoretical, experimental, and computational advancements, enabling a move from traditional trial-and-error methods to rational catalyst design. This transformation is based on a deep understanding of the mechanisms behind key reactions. By utilizing advanced spectroscopic techniques, atomic-level imaging, and computational modeling, researchers have uncovered volcano-type relationships between the electronic structure of materials and their catalytic activity. These insights have paved the way for intelligent engineering strategies, including the optimization of electronic properties through multi-metal combinations (cationic synergy) or heteroatom doping (anionic synergy) within an amorphous matrix, as well as the design of advanced nanostructures to boost active surface area and improve mass transport [150–152]. Notable examples of these strategies include incorporating Fe into Ni/Co for OER or W/Ni/Co into Mo for HER (cationic synergy), and doping oxides/hydroxides with N, P, or S to modify electronic density, conductivity, and adsorption energies (anionic synergy). The result of this shift is the development of metal-free catalysts with performance comparable to noble metals, and the expansion of electrocatalysis applications into emerging areas such as CO_2 reduction and electrochemical synthesis of value-added chemicals, opening new possibilities for the sustainable advancement of energy technologies [153–155].

1.5.5.2 Synthesis of Amorphous Multi Element Compositions

These structures, amorphous electrocatalysts are typically synthesized through direct chemical methods such as chemical reduction, chemical precipitation, electrochemical deposition, or co-precipitation. In these approaches, two or more elements are simultaneously incorporated into an amorphous structure. The addition of a dopant can enhance the physical and chemical properties of the material, increasing the number of catalytically active sites, improving electronic conductivity, and enhancing structural stability. Hybrid or amorphous heterostructures are examples of this strategy, where binary and doped compositions in a disordered framework deliver high catalytic performance in reactions like the HER and OER.

In the study by Lin et al. [156], 2D amorphous/amorphous nickel boride/borate heterostructures were engineered using a one-pot chemical reduction method. The synthesis involved reacting $NiCl_2$, $NaBH_4$, and NaOH under nitrogen atmosphere at ambient temperature. The resulting materials consisted of 2D amorphous layers of nickel boride and borate with high surface area, low electrical resistance, and abundant active sites. These heterostructures exhibited excellent performance for HER and OER in alkaline media, while also showing desirable magnetic properties. The study demonstrated that engineering 2D amorphous heterostructures can simultaneously improve catalytic performance and magnetic properties, and the straightforward synthesis method offers scalability for industrial applications.

In a separate study, Murugan et al. [157] prepared interlaced nanoflower Co@Pyn-NPs and interconnected nanochain Co@NC-NPs catalysts via wetness impregnation followed by thermal amorphization. These materials demonstrated excellent electrocatalytic performance for OER, HER, and overall water splitting under alkaline conditions. The study highlighted that non-precious amorphous Co@NC-NPs catalysts hold great promise for economically viable industrial-scale overall water splitting for energy conversion and storage.

These studies underscore the potential of binary and doped amorphous electrocatalysts in enhancing the efficiency and stability of water splitting reactions, paving the way for their application in sustainable energy technologies.

1.5.5.3 Characterization of Amorphous Multi Element Compositions

Multi element electrocatalysts, such as Ni-B/borate heterostructures and Co@NC nanoparticles, are synthesized via chemical reduction, wet impregnation, thermal amorphization, or co-precipitation, allowing multiple elements to be incorporated into a disordered framework [156,157].

TEM images of 2D Ni-B/borate heterostructures reveal ultrathin amorphous layers with thicknesses of ~4-6 nm and lateral dimensions of 50-80 nm, while SAED shows diffuse rings, confirming the absence of long-range order [156]. TEM provides high-resolution insight into nanoscale morphology, but only samples a limited region and does not capture long-range uniformity. BET analysis indicates a specific surface area of 175 m^2/g, supporting abundant edge sites.

Co@NC-NPs exhibit interlaced nanoflower and interconnected nanochain morphologies with Co nanoparticles embedded in nitrogen-doped carbon, preserving amorphous character after thermal treatment [157]. XPS spectra show Co 2p peaks at 780.1 eV and 796.0 eV (Co^{2+} species) and N 1s peaks at 398.5-400.8 eV (pyridinic/graphitic nitrogen), indicating strong metal-support interactions and improved electronic conductivity. EPR spectra display pronounced signals at $g \approx 2.002$, confirming high densities of unpaired electrons at defect sites. While XPS and EPR give detailed local chemical and electronic information, they do not provide direct morphological imaging.

Electrochemical analyses link these structural features to performance: Ni-B/borate heterostructures exhibit HER overpotentials of 185 mV and OER overpotentials of 312 mV at 10 mA cm^{-2} in 1 M KOH [136]. Co@NC-NPs show HER overpotentials of 190 mV and OER overpotentials of 310 mV, retaining >95% activity over 48 h [157]. High surface area, defect-rich amorphous structures, and heterostructuring facilitate rapid electron/ion transport and maximize active site exposure, while maintaining structural stability.

Together, the combination of TEM, SAED, XPS, EPR, and BET analyses provides a comprehensive understanding of how amorphous, heterostructured, and doped frameworks govern electrocatalytic activity. These studies illustrate the direct link between disordered structure, nanoscale morphology, defect density, and high catalytic performance, guiding the rational design of next-generation water splitting catalysts.

1.5.6 Novel Amorphous Structures

1.5.6.1 Chemistry and Key Mechanisms

Beyond traditional amorphous materials, several advanced amorphous architectures have emerged, each exhibiting distinct structural characteristics and property profiles. These include amorphous metallic alloys, doped amorphous carbon matrices, and amorphous-crystalline hybrid systems. Amorphous metal alloys are notably characterized by their high electrical conductivity and absence of long-range order [31,158]. Doped amorphous carbon frameworks often demonstrate high porosity and a significant density of electrochemically active sites, making them particularly suitable for catalytic and energy storage applications. Lastly, amorphous-crystalline hybrids, which feature an amorphous phase nanostructured onto a crystalline substrate, combine a high density of active sites from the amorphous phase with improved electrode-level electron transport supplied by the crystalline/metallic component (and reduced contact resistance), offering a synergistic platform for enhanced interfacial processes [27,159,160].

Beyond serving as a simple conductive additive, amorphous carbon can function as an active structural "host" that improves both durability and the uniformity of active-site distribution. In particular, amorphous carbon substrates with abundant dangling bonds can provide continuous and robust anchoring sites that suppress the agglomeration of isolated active species and help preserve electronically favorable oxidation states during operation (e.g., Cu single-atomic-layer clusters stabilized on amorphous carbon to prevent Cu aggregation) [161]. A related design route is to embed nanoparticles or clusters within a conductive amorphous carbon matrix, which maintains electrical continuity and reduces migration/coalescence; for example, crystalline Fe_3O_4 nanoparticles can be fabricated embedded in amorphous carbon on a conductive substrate, and single atoms can be anchored at dangling bonds on the amorphous-carbon surface, both illustrating how carbon hosts can immobilize and spatially distribute active species [162]. Similarly, confinement of catalytic nanoparticles inside amorphous carbon matrices has been used as a practical stabilization strategy in electrocatalysis: NiO/NiOOH core-shell nanoparticles confined in an amorphous carbon matrix demonstrate how carbon confinement can physically restrain nanophases while sustaining function under electrochemical conditions [163]. In addition, amorphous-carbon-matrix confinement has been highlighted as a burgeoning strategy to protect nanoparticles from degradation and to provide high conductivity for fast electron transport during long-term OER operation [164]. Overall, anchoring/embedding/confinement by amorphous carbon supports can simultaneously suppress aggregation-driven deactivation and modulate local electronic structure, offering a mechanistic pathway to enhanced catalytic durability and intrinsic activity.

1.5.6.2 Synthesis of Novel Amorphous Structures

This category includes amorphous metal alloys, doped amorphous carbons, and amorphous-crystalline hybrids, all of which have demonstrated exceptional electrocatalytic performance for HER, OER, and overall water splitting.

Amorphous Co-W-B nanoparticles have been shown to be highly active bifunctional electrocatalysts for overall water splitting [165]. The nanoparticles were synthesized via chemical reduction using $CoCl_2 \cdot 6H_2O$ and $Na_2WO_4 \cdot 2H_2O$ as precursors, with $NaBH_2$ serving both as a reducing agent and a boron source. The W content was systematically varied (1–6%) to assess its impact on catalytic activity. Characterization using XRD, SEM, HR-TEM, BET, and XPS confirmed the amorphous morphology, high surface area, and uniform elemental distribution. Electrochemical measurements demonstrated excellent HER and OER performance, while DFT calculations revealed that the incorporation of W into the amorphous structure creates multiple catalytic sites, some preferentially active for HER and others for OER, synergistically enhancing overall water-splitting rates. Chronoamperometry and recycling tests confirmed long-term stability, emphasizing the benefit of multi-catalytic sites in amorphous Co-W-B for efficient and durable electrocatalysis.

Lin et al. reported the synthesis of an amorphous/crystalline Ni-Mo-O/Cu heterostructure using a one-pot electrodeposition method at room temperature [166]. In this method, $NiCl_2 \cdot 6H_2O$, $(NH_4)_6Mo_7O_{24} \cdot 4H_2O$, $CuCl_2 \cdot 2H_2O$, and NH_4Cl were dissolved in deionized water to create the electrodeposition electrolyte. A piece of Cu foam was used as the working electrode, and a carbon electrode as the counter electrode. Electrodeposition was performed at a constant current of −250 mA for 250 s. After deposition, the electrodes were washed with deionized water. To optimize performance, control experiments were conducted by preparing Ni-Mo-O electrodes without Cu and pure Cu electrodes. Post-treatment by heating at 400 °C under N_2 flow produced crystalline counterparts (Ni-Mo-O/Cu-400 and Ni-Mo-O-400). The resulting amorphous Ni-Mo-O coupled with metallic Cu created abundant active sites and facilitated electron transfer across the interface. This synergistic interaction modified the adsorption/desorption energies of hydrogen atoms, enhancing HER activity.

Yang et al. reported a facile pyrolysis strategy to synthesize Co nanoparticles embedded in N-doped carbon nanotubes and graphitic nanosheets (Co@NCNTs/NG) as bifunctional electrocatalysts for overall water splitting [167]. Two variants were prepared using different cobalt precursors: Co_3O_4 for Co@NCNTs/NG-1 and $Co(NO_3)_2 \cdot 6H_2O$ for Co@NCNTs/NG-2. In both cases, the precursors were mixed with glucose and urea, ground for 1 h, and then pyrolyzed at 800 °C for 2 h under Ar flow to obtain black powders.

Material characterization via XRD, SEM, TEM, XPS, BET, and TGA confirmed the formation of porous structures with highly dispersed Co nanoparticles embedded within the N-doped carbon matrix. The Co nanoparticles were tightly anchored, preventing aggregation and preserving catalytic activity. The study highlights the benefits of N-doped carbon supports in providing pseudo-metallic active sites, enhancing electron transfer, and anchoring Co nanoparticles, thereby improving both HER and OER performance. This facile pyrolysis approach offers a scalable route for the design of highly efficient cobalt-based bifunctional electrocatalysts.

These amorphous structures, with abundant active sites and enhanced electron transport, deliver high performance for HER, OER, and overall water splitting, making them efficient and stable electrocatalyst candidates.

1.5.6.3 Characterization of Novel Amorphous Structures

Novel amorphous structures, including amorphous metal alloys, doped amorphous carbons, and amorphous-crystalline hybrids, exhibit exceptional electrocatalytic performance for HER, OER, and overall water splitting [165–167].

Amorphous Co-W-B nanoparticles were synthesized via chemical reduction, with W content systematically varied from 1-6 mol% [165]. TEM and HR-TEM images show spherical amorphous nanoparticles of 10-15 nm in diameter, uniformly dispersed with high surface area (~120 m^2/g). XPS confirmed Co^{2+} and B 1s signals at 188.5 eV, while W 4f peaks at 35.2-37.5 eV indicated successful W incorporation. Electrochemical tests showed HER overpotentials of 172-185 mV and OER overpotentials of 300-315 mV at 10 mA cm^{-2}, with chronoamperometry confirming stability over 48 h. DFT calculations revealed that W incorporation creates multiple catalytic sites, some preferentially active for HER and others for OER, synergistically enhancing overall water splitting. While XPS provides detailed surface composition, it does not capture morphology, making TEM essential for structural confirmation.

The amorphous/crystalline Ni-Mo-O/Cu heterostructure was prepared via one-pot electrodeposition and post-treated at 400 °C [166]. TEM images show amorphous Ni-Mo-O domains intimately coupled with crystalline Cu nanoparticles (~20-25 nm). XPS analyses of Ni 2p, Mo 3d, and Cu 2p confirm oxidation states and element distribution, while BET analysis indicates a surface area of 95 m^2/g. The interface between amorphous Ni-Mo-O and metallic Cu facilitates electron transfer and modifies hydrogen adsorption/desorption energies, enhancing HER activity. Although TEM and XPS capture morphology and chemical composition, operando studies would further elucidate dynamic structural transformations under reaction conditions.

Co@NCNTs/NG catalysts synthesized via pyrolysis show highly dispersed Co nanoparticles (~8-12 nm) embedded in N-doped carbon nanotubes and graphitic nanosheets [167]. TEM and SEM reveal uniform dispersion and porous structures. XPS indicates Co^{2+}/Co^{3+} states and pyridinic/graphitic nitrogen at 398.7-400.5 eV, while BET measurements report high surface areas of 160-180 m^2/g. TGA confirms thermal stability up to 800 °C. The tight anchoring of Co nanoparticles prevents aggregation, preserving active sites, and the N-doped carbon matrix enhances electron transfer. Limitations include the lack of direct operando observation of local structural changes during HER/OER.

Overall, these studies demonstrate that abundant active sites, high surface area, defect-rich amorphous domains, and heterointerfaces are crucial for high electrocatalytic performance. Combining TEM, HR-TEM, XPS, BET, and TGA provides a comprehensive picture of morphology, composition, and surface properties, while highlighting inherent limitations of each technique. These insights guide the design of next-generation amorphous electrocatalysts for scalable, efficient, and durable water splitting.

All in all, Amorphous electrocatalysts, with their disordered structures, offer abundant active sites, superior electron transport, and structural flexibility, resulting in excellent HER, OER, and overall water-splitting performance. Direct and indirect synthesis strategies, including electroless/pulse electrodeposition, colloidal methods, chemical reduction, and post-treatment, allow precise control over composition, morphology, and surface properties. Transition metal phosphides, borides, oxides, hydroxides, chalcogenides, and novel doped or hybrid amorphous materials demonstrate enhanced catalytic activity, stability, and scalability, making them promising candidates for next generation sustainable water splitting technologies

1.6 Electrocatalytic Performance of Amorphous Structures in Water Splitting

Amorphous materials have attracted increasing attention as electrocatalysts for water splitting because of their distinctive structural characteristics and promising performance. Building on the discussions in the preceding sections, this part of the review highlights their electrocatalytic

behavior in water splitting. The following subsections focus on the activity of amorphous structures in the HER, the OER, and their performance in overall water splitting systems.

1.6.1 Hydrogen Evolution Reaction

Amorphous electrocatalysts are becoming acknowledged as viable HER electrodes due to their short-range order and flexible bonding, which stabilize numerous under-coordinated sites while accommodating surface rebuilding under bias. In oxides, borides, phosphides/phosphosulfides, sulfides, and metallic alloys, a common strategy is to create the disordered phase directly on a conductive framework to reduce contact resistance and enhance mass transport; and when improved bubble release is observed, it is typically linked to the accompanying wettability and micro/nanotexture of the architecture rather than amorphization alone. The particular benefits therefore depend strongly on composition, surface chemistry, and electrode morphology.

Among phosphides, W-doped Fe-phosphide grown as nano-flake arrays on iron foam (Figure 10b) demonstrates how superhydrophilicity can amplify the benefits of disorder [168]. After a simple corrosion step and low-temperature phosphidation (Figure 10a), the resulting binder-free electrode shows featureless diffraction and uniform Fe/W/P/O mapping; more importantly, it combines a near-zero contact angle with a high density of under-coordinated sites. The device-level payoffs are clear: η_{10} = 35 mV in 1 M KOH as shown in Figure 10c (with competitive η at 50/500/1000 mA cm^{-2}), η_{10} = 105 mV in PBS, and η_{10} = 67 mV in alkaline seawater, all with low R_{ct} and good stability. This result also illustrates an electrode-format comparison point, binder-free 3D foams can outperform drop-cast powder electrodes (e.g., on glassy carbon) because direct growth lowers contact resistance and the superhydrophilic/superaerophobic interface accelerates bubble release at high current density [169170]. The authors attribute the intrinsic activity to W-induced electronic tuning within the amorphous lattice and facile bubble disengagement at high current densities. Accordingly, when comparing “amorphous vs crystalline” phosphides, it is important to consider both intrinsic descriptors and the electrode-level wetting/bubble behavior enabled by the chosen substrate [170].

In a one-bath conversion route, Pang et al.[171] synthesized Fe-Co carbonate-hydroxide nanosheets coated by amorphous Co-S-P shells, which deliver η_{10} = 73 mV (Figure 10d) in 1 M KOH. This ordered-core/amorphous-shell motif provides a structure-performance rationale, the hydroxide-derived scaffold promotes electrolyte access and water activation in alkaline media, while the amorphous Co-S-P shell supplies abundant unsaturated sites and locally tunable electronic structure, so the interface can outperform a single-phase phosphide at similar loading [172]. The activity enhancement tracks with higher C_{dl}, consistent with more accessible sites. At the same time, the Cdl increase suggests that part of the improvement may be architecture-enabled (exposed area/porosity), motivating comparisons on identical substrates when available.

A different structural motif, amorphous ball-in-ball hollow spheres [173], encapsulates oxygen-containing amorphous Co-P-O within N-doped carbon. Here, minimal structural proof suffices (diffuse SAED, featureless XRD (Figure 10e), and oxygen-vacancy ESR signals) to support the claim; the catalytic readout in 1 M KOH (in Figure 10f it is obvious that η_{10} is 157 mV, lower slope than the single-shell control) aligns with the idea that oxygen vacancies and a conductive carbon framework together ease water dissociation and charge transport. This example also helps compare structure formats, unlike binder-free foam electrodes, carbon-encapsulated hollow architectures rely on internal conductive networks to maintain percolation, so the performance gains are often linked to coupling “defect-rich amorphous domains” with “engineered electron pathways” rather

than amorphousness alone. Stability at 10 mA cm^{-2} over 12 h further supports the platform's robustness.

In other work, which was conducted by Cao et al. [174]; as shown in Figure 10g, one-step, room-temperature electrodeposition/phosphidation yields amorphous NiCoP/CC, characterized by roughened nano-textured surfaces (Figure 10h) and charge-transfer signatures. In 1 M KOH, NiCoP/CC reaches η_{10} = 74 mV (101/149 mV at 20/50 mA cm^{-2})(Figure 10i), with markedly lower R_{ct} than binary controls and durable operation over 2000 cycles and 24 h galvanostatic testing while remaining amorphous. So this work shows that electrodeposition on carbon cloth improves electrical continuity versus powder/binder films, helping the amorphous NiCoP motifs translate into lower Rct and practical current-density operation.

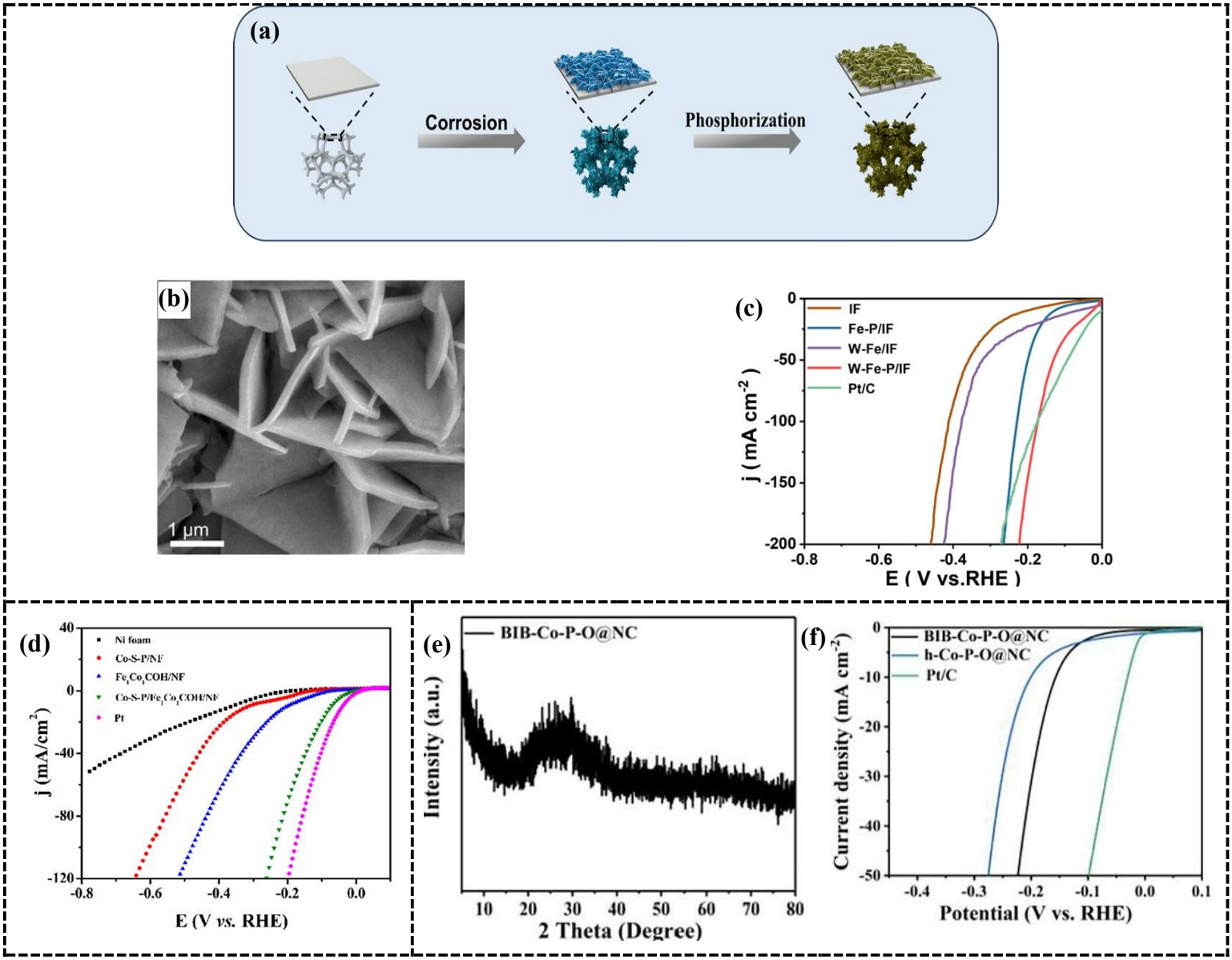

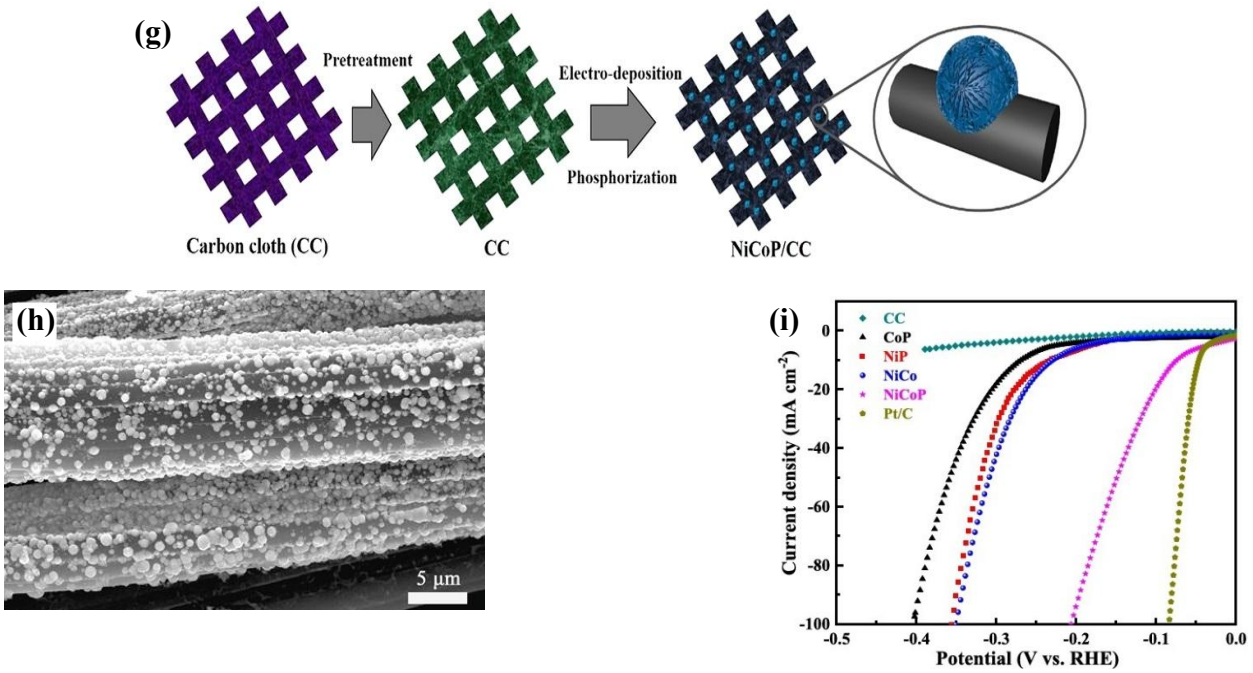

Figure 10. (a) Synthesis route of W-Fe-P/IF; (b) SEM micrograph of W-Fe-P/IF; (c) LSV curves of Pt/C, W-Fe-P/IF, W-Fe /IF, Fe-P/IF, and IF [168]. (d) HER polarization curves of synthesized materials 1 M KOH [171]. (e) XRD pattern of BIB-Co-P-O@NC; (f) HER electrochemical measurements of structures 1 M KOH [173]. (g) Synthesis route of NiCoP/CC; (h) SEM image of NiCoP/CC; (i) Electrochemical measurements as-prepared catalysts 1 M KOH [174].

Amorphous Fe-Ni-B nanosheets, which was synthesized by Yadav et al. [175], illustrate how disorder can be coupled to ultrathin morphology. A microemulsion $NaBH_4$ reduction produces 3-4 nm sheets (high specific area), uniform Fe/Ni/B mixing, and a single broad XRD hump near 45° (Figure 11a). Ultrathin amorphous boride-type networks are particularly effective in alkaline HER because they expose abundant under-coordinated motifs while minimizing solid-state transport lengths, which can accelerate the Volmer-Heyrovsky pathway when charge transfer is not rate-limiting [176]. The optimized $Fe_{1.0}Ni_{1.0}B$ reaches η_{10} = 70 mV and maintains low overpotentials at 100/500/1100 mA cm^{-10} (149/186/204 mV) (Figure 11b). This high-current behavior is also consistent with an electrode-format advantage of ultrathin, binder-free (or strongly adhered) nanosheet architectures relative to drop-cast powder films, where contact resistance and bubble blocking can become dominant at large j [177]. A small Rct (2.2 Ω), and durability over ~6000 cycles point to accelerated Volmer-Heyrovsky kinetics enabled by the amorphous network; crystallization at 500 °C degrades both η_{10} (136 mV) and Tafel slope (54 mV dec^{-1}), directly linking performance to the disordered state.

As a complementary carbon-hosted approach, Co@NC nanoparticles prepared by wetness impregnation followed by thermal amorphization (500 °C) convert a crystalline interlaced nanoflower into an amorphous nanochain (Figure 11d) network with homogeneous Co/N/C/O distribution and Co-N coordination [157]. This structure-format comparison is informative, unlike free particles on planar electrodes, carbon-encapsulated nanochains provide continuous electronic percolation and stabilize highly dispersed Co sites (including Co-N motifs), so the performance gain reflects both amorphization and electrode-level conductivity/anchoring effects. In 1.0 M KOH the catalyst delivers η_{10} = 142 mV (vs. 301 mV for the crystalline precursor) (Figure 11e), low

charge-transfer resistance (1.8 Ω), and enlarged double-layer capacitance (~56.9 mF cm^{-2}). The conductive N-carbon encapsulation improves charge transport and protects Co sites, sustaining HER for ~80 h with ~1.3% potential drift as shown in Figure 11f.

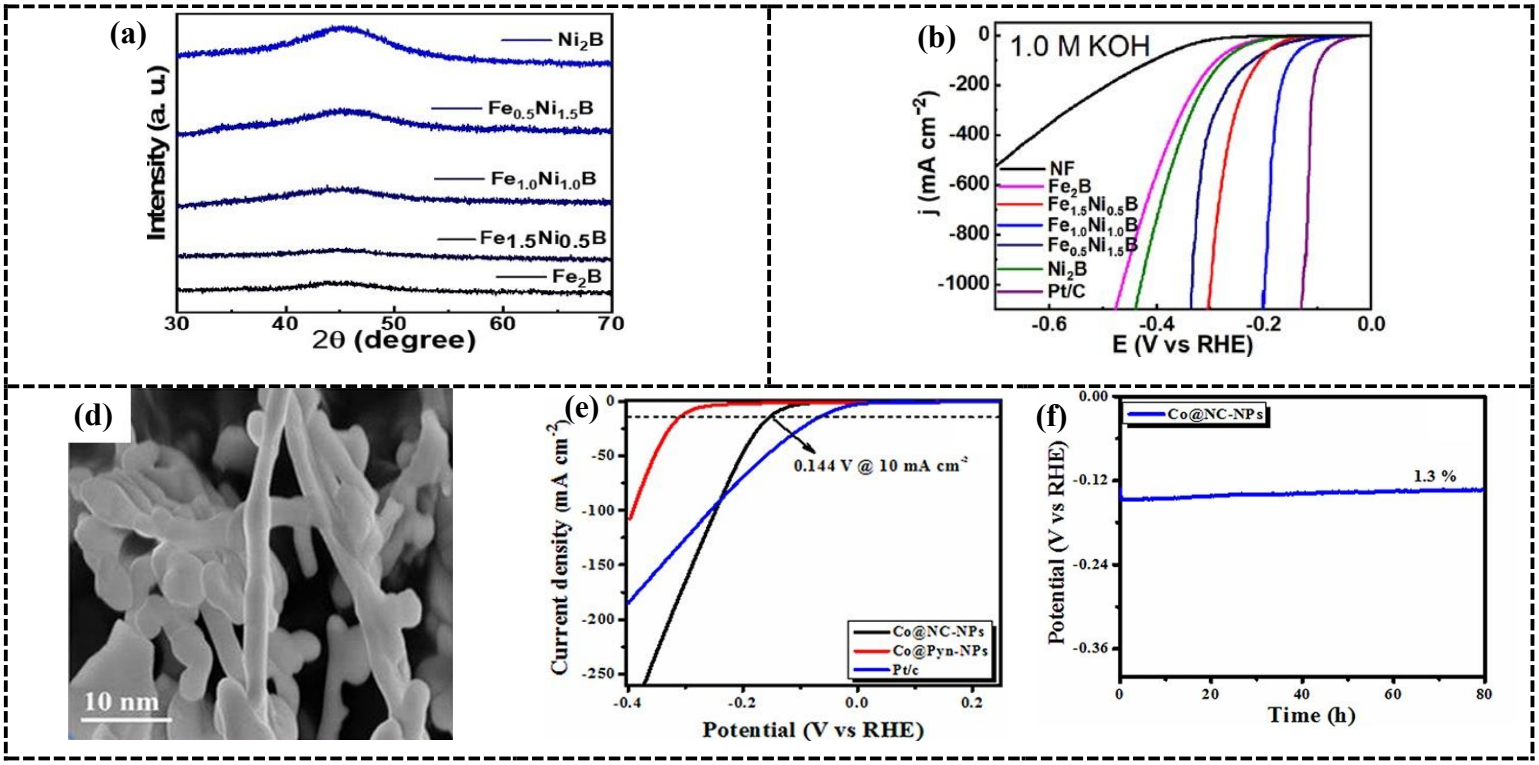

Figure 11. (a) Fe-Ni-B nanosheets XRD pattern; (b) Polarization curves, and (c) Tafel slopes of synthesized materials 1 M KOH [175]. (d) FESEM micrograph of Co@NC nanoparticles; (e) Pt/C, Co@Pyn- nanoparticles, and Co@NC- nanoparticles LSV curves 1 M KOH; (d) Co@NC- nanoparticles stability test [157].

In oxide systems, $CoNiRuO_x$ grown on Ni foam exemplifies how composition and topology can be co-tuned at room temperature [178]. A corrosion-replacement process produces a conformal 15-20 nm nanoparticle layer; spectroscopies show that Ru incorporation perturbs the M-O environment, consistent with an electronically modified amorphous oxide. In alkaline HER, Ru incorporation into Ni/Co-oxide environments is frequently rationalized as improving the water-dissociation step and interfacial charge transfer, so the strong kinetics here are consistent with a "local electronic/coordination tuning" role rather than surface area alone [179]. In 1 M KOH, the electrode requires only η_{10} = 43 mV (Figure 12b) and sustains 100 mA cm^{-1} for over 100 h (Figure 12c) with negligible decay. This performance should also be viewed in the context of electrode-format comparison: conformal, binder-free coatings on 3D Ni foam often show lower interfacial resistance and better gas removal than drop-cast powder films on planar substrates, particularly at elevated current densities [170,180]. Lower R_{ct} and enlarged ECSA (relative to Co/NF, Ru/NF, and bare NF) indicate that the activity gain is intrinsic to the disordered, binder-free coating; minor Ru leaching does not compromise performance. Accordingly, the most convincing structure–performance interpretation in this case is that amorphization supplies abundant accessible motifs while the 3D foam architecture ensures electronic percolation and bubble disengagement, allowing intrinsic gains to translate into practical operation.

Likewise, Jiang et al. [181] realized a binder-free amorphous NiO_x leaf array on Ni foam via one-step H_2O_2-assisted hydrothermal oxidation (Figure 12d). This "leaf-array on foam" configuration provides a clear structural comparison against conventional powder electrodes: the open, oriented array increases electrolyte accessibility and accelerates bubble detachment. With diffraction free of NiO peaks and fringe-free domains, NiO_x/NF reaches η_{10} = 70 mV and maintains 318/361 mV at 500/1000 mA cm^{-2} (Figure 12e), outperforming Pt/C at high current. A low resistance has been shown, R_{ct} = 51.3 Ω, C_{dl} = 17.8 mF cm^{-2}, and stable 50 h at 20 mA cm^{-2} and 1000 cycles corroborate that the amorphous network and NiO_x/Ni interface jointly enhance site accessibility and charge transfer. More broadly, high-current alkaline electrolysis studies increasingly emphasize that bubble dynamics and flow/porous-electrode design can be decisive at industrially relevant current densities, reinforcing why array/foam electrodes frequently outperform planar electrodes even for similar catalyst chemistries [180].

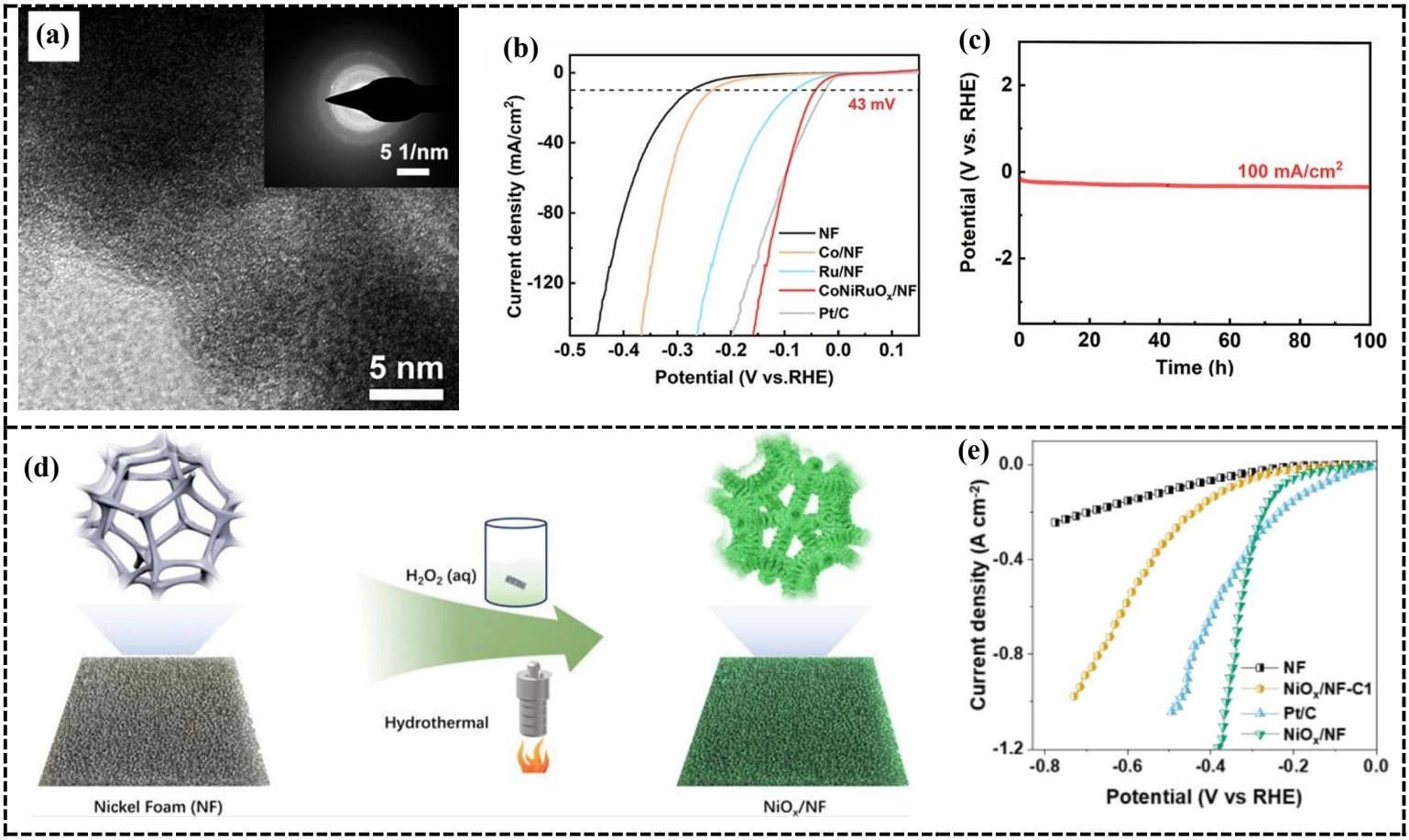

Figure 12. (a) HRTEM and SAED images of $CoNiRuO_x$/NF, (b) LSV curves of Pt/C, $CoNiRuO_x$/NF, Ru/NF, Co/NF, and NF 1 M KOH; (c) Chronopotentiometric pattern of $CoNiRuO_x$/NF [178]. (d) Synthesis route of NiO_x/NF; (e) LSV curves of NiO_x/NF, Pt/C, NiO_x/NF-C1, and NF 1 M KOH [181].

In sulfide materials, amorphous FeS nanorods grown in octylamine by Zhang et al. [182] give a useful counterpoint. As it is obvious in Figure 13a the material shows η_{10} = 67 mV in 0.5 M H_2SO_4. Lower R_{ct} (5.5 Ω) (Figure 13b) and higher C_{dl} (8.7 mF cm^{-2}) than crystalline counterpart, together with durability under 2500 cycles and 80 h galvanostatic testing, trace the advantage to defect-rich amorphous domains that preserve activity under corrosive conditions. Notably, this "amorphous

vs crystalline" comparison is particularly meaningful in acidic media, where stability constraints often eliminate many non-noble candidates; amorphization can help maintain activity by tolerating defect formation and structural relaxation without catastrophic loss of catalytic ensembles [183].

In strong base, Co-Ni-S nanoflakes on carbon cloth (ligand-assisted oxide growth followed by mild vulcanization) (Figure 13c) show modest η_{10} = 192 mV (Figure 13d); yet, after ECSA normalization they exhibit higher intrinsic rates than ordered analogues [184]. This is an important structure/format point to consider that, ECSA-normalized rates (jECSA) are widely recommended for comparing intrinsic activity across different morphologies and electrode formats, because geometric currents can be dominated by roughness/porosity differences [185]. In addition, carbon cloth electrodes often outperform planar drop-cast films because the textile architecture improves electrical percolation and mitigates catalyst layer delamination/leaching under gas evolution, which should be considered when comparing sulfide nanoflakes on CC against other supports [186]. Low R_{ct} (2.32 Ω), small η shifts after 1000 cycles, and stable 36 h operation at 10 mA cm^{-2} (Figure 13e) indicate that defect mediated surface rearrangement in the amorphous state can sustain kinetics under polarization.

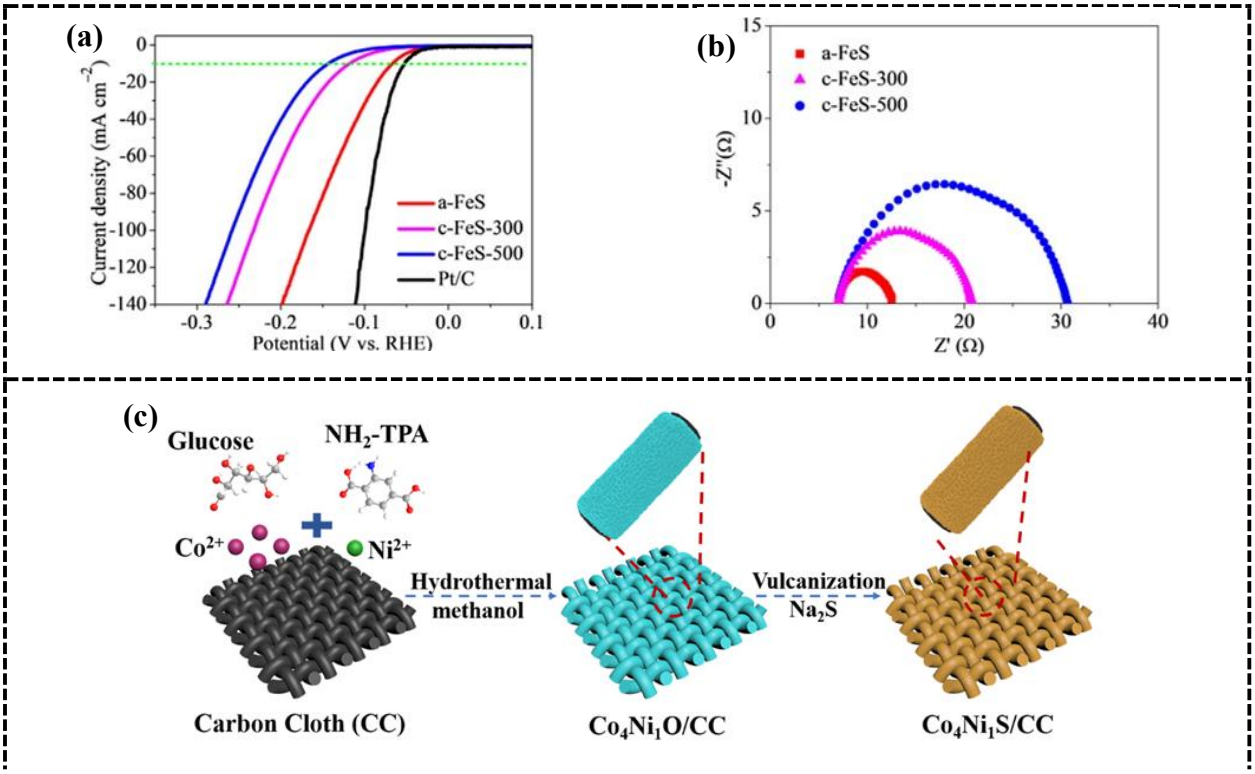

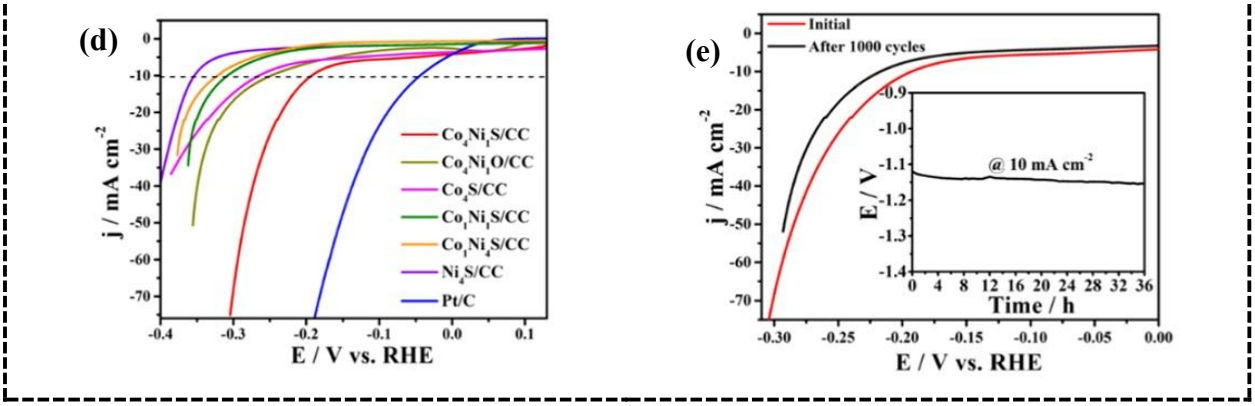

Figure 13. (a) LSV measurements of materials in 0.5 M H_2SO_4; (b) a-FeS, c-FeS-300 and c-FeS-500 Nyquist plots [182]. (c) Co_4Ni_1S/CC preparation schematic; (d) HER polarization curves of as-prepared materials in 1 M KOH; (e) Co_4Ni_1S/CC LSV curves before and after 1000 cycles of usage (inset is chronopotentiometry test) [184].

In other experiment, which was conducted by Jian et al. [187] they analyze the effect of amorphization in HER. This thin-film platform also makes the "amorphization effect" easier to interpret than in many powder studies, because sputtered alloys minimize binder effects and allow more controlled structure/composition comparisons on the same conductive scaffold (Ni foam). In this work, amorphous Cu-W thin films that were co-sputtered onto Ni foam, as well as the effect of the percentage composition of these two elements on the amorphization of this microstructure, which is shown in Figure 14a, were investigated. $Cu_{50}W_{50}$ reaches η_{10} = 65 mV (194 mV at 100 mA cm^{-2}) in 1 M KOH (Figure 14b) and $\eta_{10} \approx$ 158 mV in 0.5 M H_2SO_4 (Figure 14c), which was better than the crystalline structure, and remains stable for 200 h at 100 mA cm^{-2} and 50 h even at 800 mA cm^{-2}. This performance therefore provides a useful comparison against other electrode formats, conformal, binder-free coatings on 3D foams commonly exhibit lower interfacial resistance and improved gas removal compared with drop-cast powder films on planar substrates, especially at high current densities. DFT suggests that amorphization shifts the d-band and brings ΔG_H close to zero, highlighting an adsorption-energy mechanism rather than solely a site-count effect. This ΔG_H-based interpretation is consistent with broader thin-film alloy electrocatalysis discussions, where tuning adsorption energetics (rather than simply increasing roughness/ECSA) is emphasized as the primary origin of intrinsic activity shifts.

For ternary amorphous films formed in situ, a hydrothermal NiFeMo layer on Ni foam provides a clean comparison against NiFe and bare Ni supports [188]. Prepared at 180 °C (12 h) in $FeCl_3$/Na_2MoO_4, the film shows only Ni-foam reflections (XRD) with a diffuse SAED halo and surface Ni^{2+}/Fe^{3+}/Mo^{6+} by XPS; the pod-like coating uniformly covers the 3D scaffold. In 1.0 M KOH it delivers η_{10} = 180 mV (vs 273 mV for NiFe/NF; 264 mV NF) (Figure 14d), and as shown in Figure 14e 20 h stability at 10 mA cm^{-2} evidence that the amorphous matrix plus direct electrical coupling boost alkaline Volmer-Heyrovský kinetics. Accordingly, this system also serves as an electrode-type comparison: relative to powders deposited on inert substrates, in-situ grown amorphous films on Ni foam can reduce contact resistance and stabilize the catalyst layer under long electrolysis, which is particularly important for interpreting structure-performance claims.

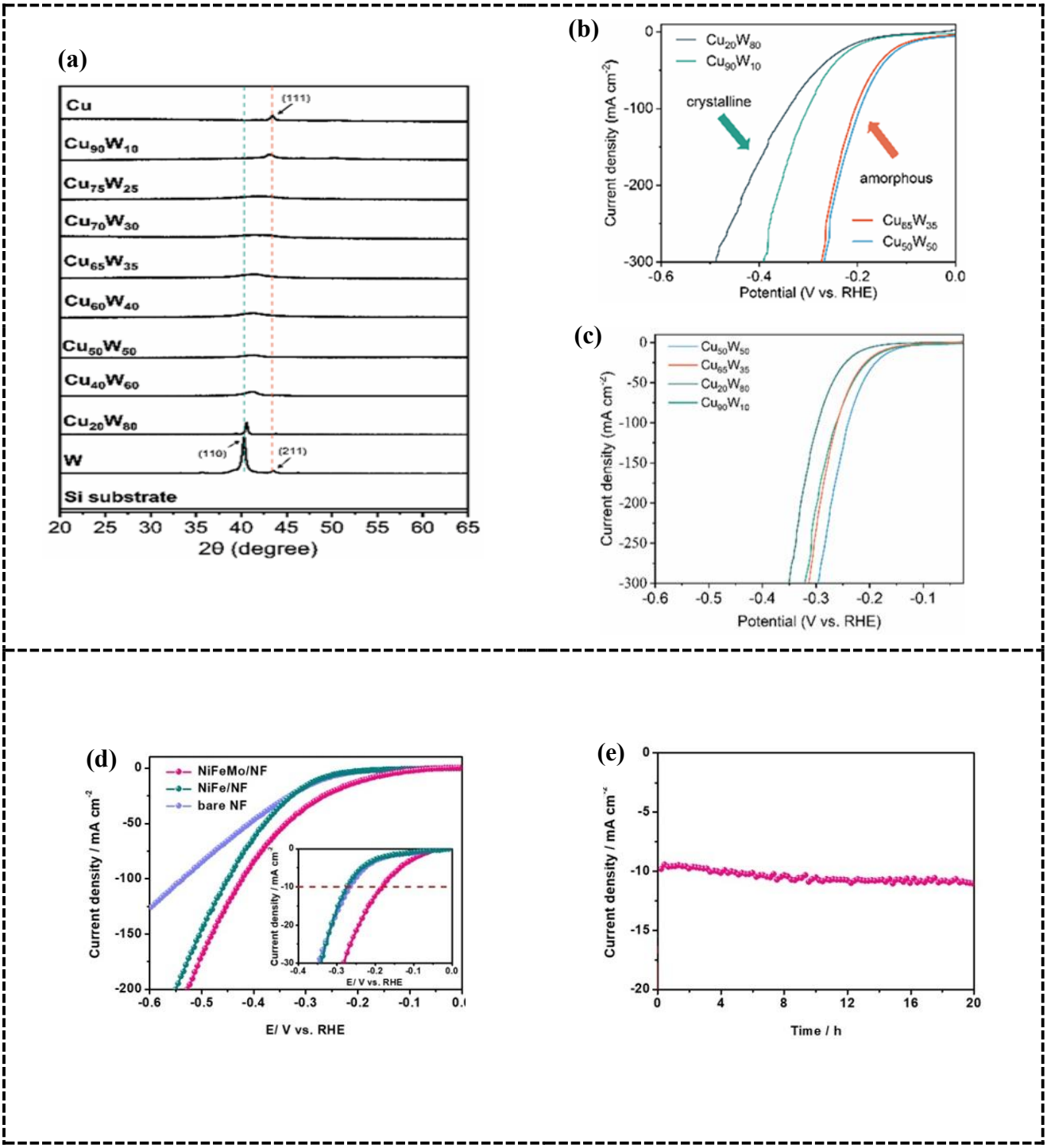

Figure 14. (a) As-prepared samples XRD patterns; LSV measurements for materials in (b) alkaline (1 M KOH), and (c) acidic conditions (0.5 M H_2SO_4) [187]. (d) Polarization curves for NiFeMo/NF, NiFe/NF, and NF 1 M KOH; (e) NiFeMo/NF stability test [188].

On highly alkaline electrolytes, electrodeposited amorphous NiMo on Ni foam underscores the benefit of binder-free integration for ohmic and bubble-management losses [189]. The optimized pH 10 film ($NiMo_{(pH10)}$) yields η_{10} = 63.9 mV and η_{100} = 157.1 mV (6 M KOH, 80% iR compensation) (Figure 15c), maintains performance on scale-up, and runs at 100 mA cm^{-2} for 100 h with only localized cracking/partial peeling minor morphological changes (Figure 15a and Figure 15b) that do not materially impact activity. Such durability under high alkalinity/high current aligns with broader findings that NiMo coatings are particularly effective when structure-engineered as strongly coupled films/arrays on conductive scaffolds rather than as thick, binder-containing layers [190]. Kinetic analysis indicates a Volmer-limited Volmer-Heyrovský pathway and the smallest Nyquist semicircle among comparators. In parallel, amorphous Ni-Sb-P films on graphite provide a porous, super-wetting alternative [191]: super-hydrophilicity/aerophobicity (contact angle < 10°) aids bubble release, while low R_{ct} (4.2 Ω cm^{-2}) (Figure 15e) and η_{10} = 77 mV (Figure 15d); long chronoamperometric/chronopotentiometric tests show minimal degradation, consistent with a defect-rich amorphous matrix that exposes active sites without binder penalties. This supports a structure-performance rationale, amorphous NiMo can provide abundant accessible motifs while the foam architecture minimizes interfacial resistances, so improved charge-transfer characteristics are reflected directly in the Nyquist response.

Finally, ultrasmall amorphous RuFeP clusters on carbon nanofibers, which was synthesized by Yang et al. [192], provide a noble-lean benchmark approaching Pt-like behavior. The $NaBH_4$-assisted nucleation followed by low-temperature phosphidation yields 0.4–3.6 nm clusters that remain amorphous and uniformly dispersed (Figure 15f); this ultrasmall, amorphous-cluster motif is also an important structure-format comparison versus conventional nanoparticles, because maximizing the fraction of surface atoms improves noble-metal utilization while the amorphous state provides locally flexible coordination environments [192]. in 1.0 M NaOH the system reaches η_{10} = 16 mV (65.8 mV in 0.5 M H_2SO_4) (Figure 15g and Figure 15h), and 100 h stability in both electrolytes. This performance can be interpreted in electrode-type terms as well: carbon nanofiber supports provide continuous electronic percolation and suppress cluster agglomeration, helping the intrinsic activity of ultrasmall amorphous phosphide clusters translate into stable device-level currents [192]. As a useful comparison to other Ru-phosphide structures discussed in the broader literature, crystalline/amorphous Ru-RuP core-shell motifs and Ru-alloyed iron phosphides also emphasize that interfacial/electronic tuning of Ru-P environments can deliver Pt-competitive HER kinetics with reduced precious-metal loading [193,194]. Computations attribute the activity to near-optimal ΔG_{H^*} and favorable alkaline water-dissociation energetics, reinforcing that amorphization can tune adsorption thermodynamics, not just site density. This aligns with recent Ru-based HER design discussions that repeatedly identify adsorption-energy optimization and interfacial synergy (rather than surface area alone) as the primary route to Pt-like behavior at lower Ru usage [195]. Notably, a review on Ru_2P-type and related Ru-phosphide motifs specifically highlights amorphous RuFeP nanoclusters supported on carbon nanofibers as an example of Pt-level overpotentials in both alkaline and acidic media, underscoring the broader relevance of this structural strategy [196].

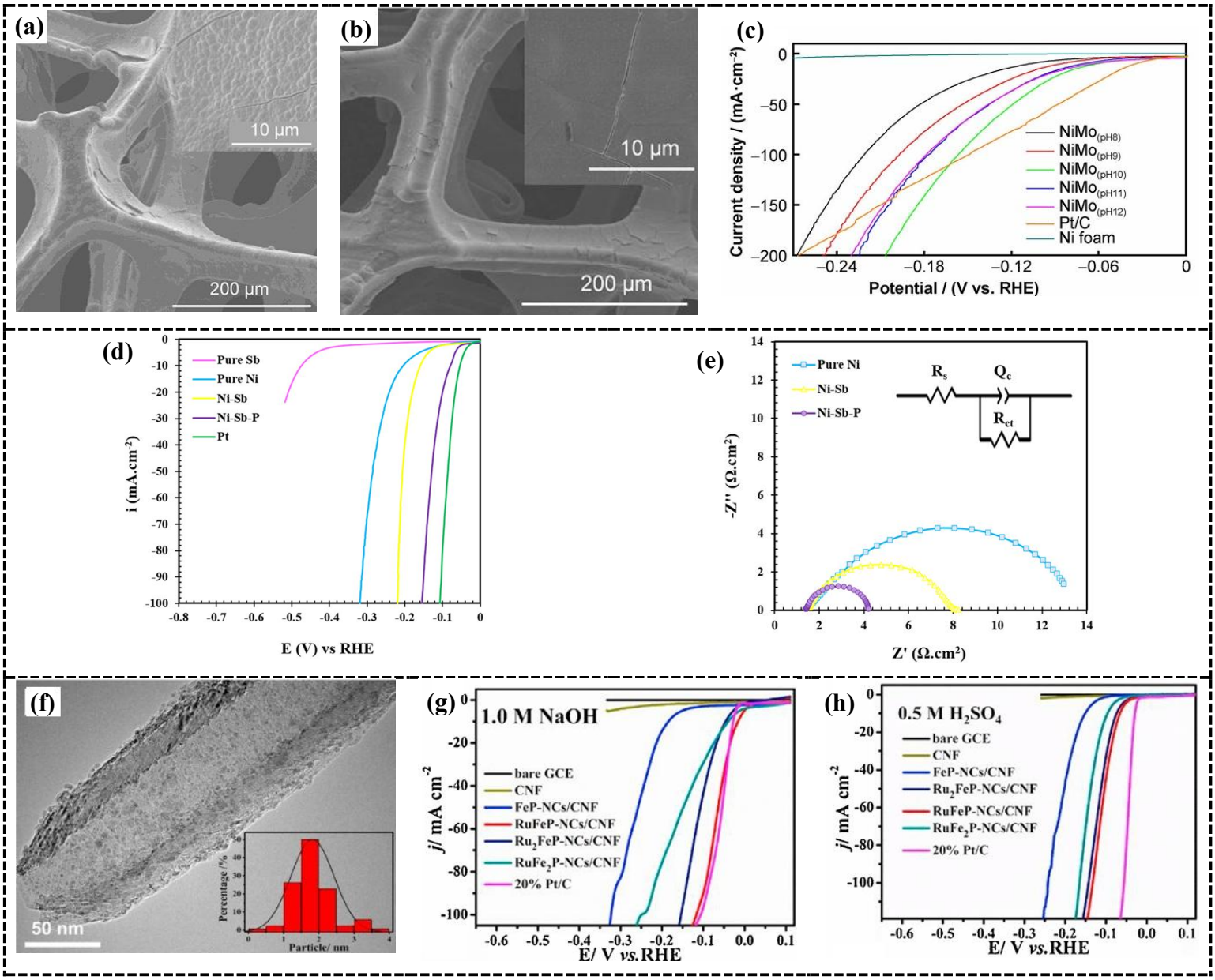

Figure 15. (a) SEM micrograph of NiMo(pH10); (b) SEM micrograph of $NiMo_{(pH10)}$ after stability test; (c) LSV curves of materials in 6 M KOH [189]. (d) LSV curves of different structures for HER activity in 1 M KOH; (e) Nyquist plots of the Ni-Sb-P, Ni-Sb, and Ni [191]; (f) TEM image of RuFeP-NCs/CNF, Inset is a size distribution histogram of RuFeP-NCs; LSV curves of synthesized materials in (g) 1 M NaOH, and (h) 0.5 M H_2SO_4 [192].

Taken together, these studies show that amorphous phases offer multiple, sometimes complementary levers, active-site abundance, adsorption-energy tuning, and in cases where amorphous coatings also exhibit hydrophilic surface chemistry and hierarchical porosity/roughness improved wetting and bubble management, and mechanical tolerance to reconstruction, that translate into low overpotentials and durable high-current HER across acids, bases, and even saline environments. When comparing absolute values, differences in electrolyte (e.g., 6 M KOH vs. 1 M KOH or PBS), iR compensation, and geometric vs. intrinsic normalization

must be kept in view; accounting for these variables, amorphization emerges as a robust and generalizable strategy for HER electrocatalyst design.

Table 2 provides a concise comparison of amorphous HER catalysts across chemistries and supports, summarizing η at 10 mA cm^{-2}, high-current performance, and durability under the authors' reported conditions. Read left to right, it shows which systems pair low kinetic barriers with stable operation at practical current densities. Taken together, the comparisons highlight a consistent trend: amorphous architectures, especially when directly integrated with conductive scaffolds and/or using multi-component compositions, deliver lower overpotentials, competitive Tafel slopes, and robust high-current stability.

Table 2. Performance of different amorphous electrocatalysts in HER process.

Catalyst (Support)	**Electrolyte**	**η at 10 mA cm^{-2} (mV)**	**High-j point (mV)**	**Stability**	**Reference**
W-Fe-P (iron foam)	1 M KOH / PBS / alk. seawater	35 (KOH); 105 (PBS); 67 (seawater)	93 @ 50; 354 @ 500; 404 @ 1000 mA cm^{-2} (KOH)	15 h @ 10 mA cm^{-2}; 15 h @ 500 mA cm^{-2}	168
Co-S-P / Fe-CoCOH (Ni foam)	1 M KOH	73	—	24 h two-electrode @ 1.5–1.7 V	171
Ball in Ball-Co-P-O@NC	1 M KOH	157	—	12 h @ 10 mA cm^{-2}	173
NiCoP (carbon cloth)	1 M KOH	74	101 @ 20; 149 @ 50 mA cm^{-2}	24 h @ −10 mA cm^{-2}; 2000 CV	174
$Fe_{1.0}Ni_{1.0}B$ nanosheets	1 M KOH	70	149 @ 100; 186 @ 500; 204 @ 1100 mA cm^{-2}	~6000 CV (negligible drift)	175
Co@NC nanochains	1 M KOH	142	—	~80 h ($\Delta\eta \approx$ 1.3%)	157
$CoNiRuO_x$ (Ni foam)	1 M KOH	43	—	100 h @ 100 mA cm^{-2}	178
NiO_x leaf arrays (Ni foam)	1 M KOH	70	318 @ 500; 361 @ 1000 mA cm^{-2}	50 h @ 20 mA cm^{-2}; 1000 CV	181

amorphous-FeS nanorods	0.5 M H_2SO_4	67	200 @ 141.2 mA cm^{-2}	2500 CV; 80 h @ 80 mV	182
Co_4Ni_1S (carbon cloth)	1 M KOH	192	—	36 h @ 10 mA cm^{-2}; 1000 CV	184
$Cu_{50}W_{50}$ (Ni foam)	1 M KOH / 0.5 M H_2SO_4	65 (KOH); ≈158 (acid)	194 @ 100 mA cm^{-2} (KOH)	200 h @ 100 mA cm^{-2}; 50 h @ 800 mA cm^{-2}	187
NiFeMo (Ni foam)	1 M KOH	180	—	20 h @ 10 mA cm^{-2}	188
NiMo(pH10) (Ni foam)	6 M KOH	63.9	157.1 @ 100 mA cm^{-2}	100 h @ −100 mA cm^{-2}	189
Ni-Sb-P (graphite)	1 M KOH	77	—	90 h @ −100 mA cm^{-2}; 1000 CV; 24 h (98%)	191
RuFeP NCs (CNF)	1 M NaOH / 0.5 M H_2SO_4	16 (base) / 65.8 (acid)	111 @ 100 mA cm^{-2} (base) / 132 @ 100 mA cm^{-2} (acid)	100 h (acid & base)	192

1.6.2 Oxygen Evolution Reaction

Amorphous OER electrodes are frequently contain defect-rich, short-range-ordered backbones can accommodate in situ surface reconstruction to oxy(hydroxide)-like active layers while maintaining electrical contact to the current collector. Nevertheless, amorphousness does not universally guarantee higher OER performance: in acidic electrolytes relevant to PEM water electrolysis, crystalline/rutile IrO_2 remains a widely used benchmark, largely due to its practical stability; and in alkaline media, several crystalline oxide families (e.g., perovskites/double perovskites) exhibit high intrinsic activity. Accordingly, throughout this section we interpret "amorphous advantages" primarily in terms of the structural/electrode features that frequently accompany disordered phases (active-site density, reconstruction dynamics, and electrode integration), and we avoid treating crystallinity as a standalone performance descriptor.

Amorphous phosphides continue to set the pace for alkaline OER because they combine short-range disorder with surfaces that reconstruct into highly active oxy(hydroxide) skins. This "phosphide-as-precatalyst" interpretation is now widely accepted in alkaline OER studies, where phosphide surfaces undergo rapid (oxy)hydroxide conversion and the steady-state activity is often

governed by the reconstructed skin rather than the pristine phosphide lattice [197]. On nickel-iron foam, Wang et al [198]. used a corrosion/etching phosphidation sequence to anchor Mo-doped NiFeP nanospheres (Figure 16a). The film is X-ray amorphous and superhydrophilic (≈0° contact angle); STEM-EDS shows uniform Ni/Mo/Fe/P/O dispersion. Mo-doping in NiFe phosphide/derived systems is frequently rationalized as enhancing electronic interactions and charge transfer during OER reconstruction, which supports the "composition-tuned reconstruction" explanation implied here [199]. In 1.0 M KOH it delivers $\eta_{10}/\eta_{50}/\eta_{500}/\eta_{1000}$ = 207/227/310/330 mV (Figure 16b). Multi-step and constant-current tests (10-500 mA cm^{-2}) show negligible drift, morphology is retained, and in alkaline seawater the electrode maintains η_{10} = 257 mV without chlorine evolution, evidence that amorphization + high-valent Mo accelerates charge transfer while the measured superhydrophilic surface and 3D foam-supported nanostructure likely support high-current operation by facilitating electrolyte replenishment and bubble removal.

A phosphate analogue underscores the same motif. researchers introduced Co into an amorphous $FePO_4$ framework via a mild hydrothermal route as shown in Figure 16d [200]. This system provides a useful structure-only comparison against the phosphide-on-foam case above, because it is evaluated on glassy carbon where the electrode architecture advantage is reduced and intrinsic kinetic trends (e.g., R_{ct}/Tafel/C_{dl} shifts) are more clearly reflected in the measured response. Without belaboring full phase proofs, the key point is that Co-$FePO_4$, still largely disordered, lowers η_{10} to 320 mV (Figure 16e) with a Tafel slope of 64 mV dec^{-1} on glassy carbon; C_{dl} increases and R_{ct} drops versus $FePO_4$, consistent with added redox-active centers and faster interfacial kinetics within an amorphous phosphate backbone. In other words, relative to the phosphide examples where reconstructed oxy(hydroxide) skins and foam-enabled transport can dominate, this phosphate case highlights the more direct role of cation tuning within a disordered polyanion framework in shifting interfacial kinetics on a planar electrode. A 32 h durability test with retained morphology closes the loop. Together these P-family cases show how disorder and moderate cation tuning converge, and in some cases concomitant superwetting surface states and porous textures further support high-current operation by improving mass transfer and bubble removal.

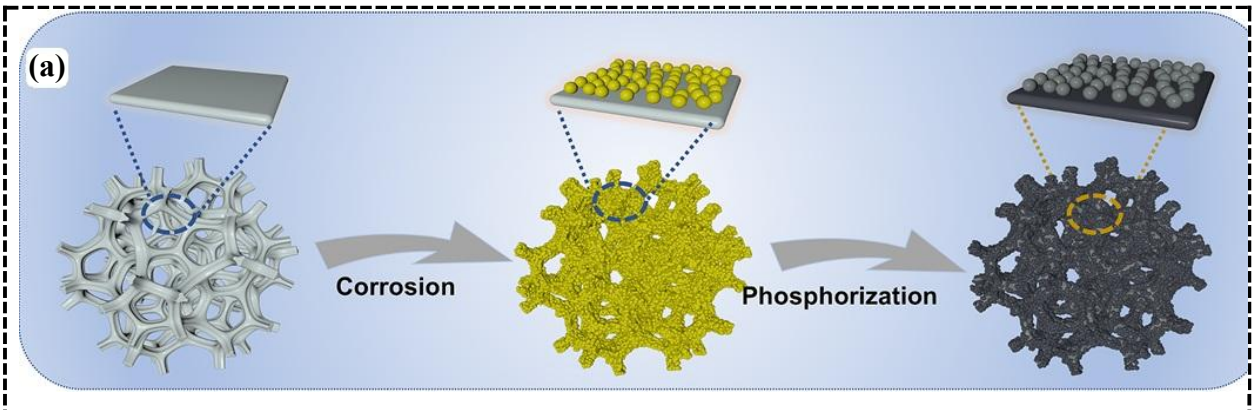

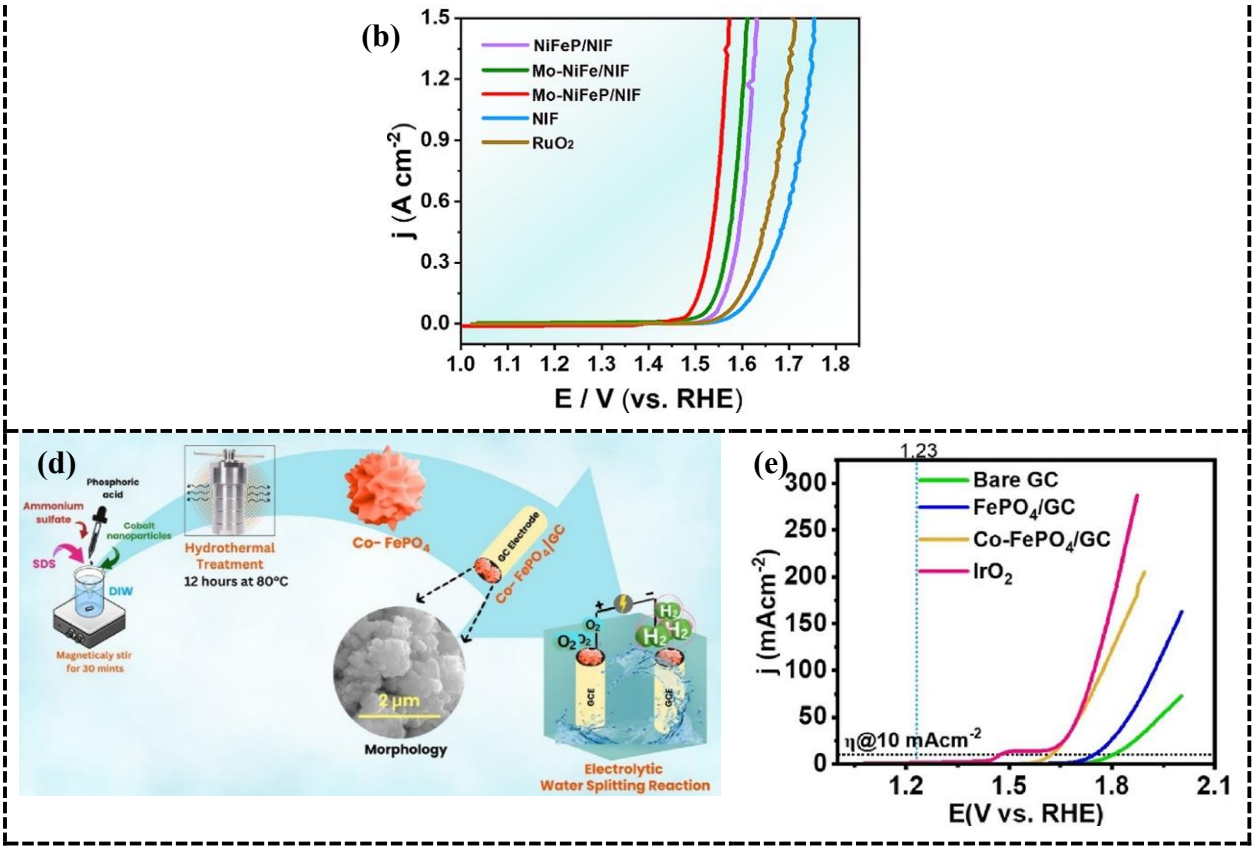

Figure 16. (a) Synthesis illustration of Mo-NiFeP/NIF; (b) LSV curves, and (c) Tafel slopes of obtained catalysts in 1 M KOH [198]. (d) Synthesis schematic of Co–$FePO_4$; (e) LSV curves bare GC, Co–$FePO_4$ /GC, $FePO_4$/GC, and IrO_2 in 1 M KOH [200].

Boride-rich glasses couple electronic disorder with high site density. Wang et al. [201] reported amorphous Mn-Co-B nanoparticles (15-50 nm) with a single XRD hump near 45° as it is obvious in Figure 17a. The optimized MnCoB-1 records η_{10} = 292 mV (Figure 17b), outpacing CoB; EIS shows the smallest semicircle, $C_{dl} \approx 39.4$ (Figure 17c) and ECSA ≈ 985 cm^2 are large, and DFT assigns a lower ΔG for the O → OOH** step, indicating adsorption-energy tuning, not just surface area.

Among oxides, the clearest through-line is that disordered lattices provide both reconstruction tolerance and favorable adsorption energetics once biased into oxyhydroxide states. Amorphous CoO_x grown on N-doped carbon (CoO_x/CN_x) [202]: with only a light structural touch (SAED/HRTEM showing mostly amorphous domains) (Figure 17d), the emphasis falls on performance, η_{10} = 310 mV (Figure 17e) and 60.7 mV dec^{-1} (Figure 17f) in 1.0 M KOH, plus strong stability (≈24-100 h) and ~94% O_2 Faradaic efficiency. This is also a useful structure/support comparison, CoOx anchored on N-doped carbon supports is widely reported to benefit from improved electronic coupling and conductivity relative to unsupported oxides or weakly contacted powders, which can elevate mass activity/TOF even when detailed crystallography is not the main focus. Interfacial coupling to CN_x (lower R_{ct}, higher mass activity/TOF) rather than heavy crystallography explains the kinetic gains.

Another oxide exemplar is an ultralow Ru incorporated amorphous cobalt oxide on Ni foam (Ru–CoO_x/NF) [203]. The film is made by growing ZIF-L nanosheets on NF, calcining at 250 °C (air) to

CoO_x/NF, then briefly soaking in $RuCl_3$ (ethanol) and re-annealing at 250 °C under inert gas to yield Ru-CoO_x/NF while preserving the vertical-nanosheet morphology as shown in Figure 17g. MOF-derived Ru-doped CoOx systems are commonly interpreted through, interface engineering and electronic modulation at ultralow Ru contents, which supports the idea that small amounts of Ru can disproportionately influence charge transfer during OER on Co-based oxides [204]. TEM shows no lattice fringes and XRD of scraped powder is featureless as it is obvious in Figure 16h (only NF peaks on the intact electrode), confirming an amorphous phase; EDX maps Ru uniformly, and XPS registers Co 2p shifts to higher binding energy after Ru insertion. In 1.0 M KOH the electrode reaches η_{100} = 220 mV and η_{1000} = 370 mV (Figure 17i), alongside a large $C_{dl} \approx 102$ mF cm^{-2} and the smallest R_{ct} among controls; durability is excellent (~100 h i-t and 10000 CV cycles with minimal change). Post-activation XPS/Raman indicate surface reconstruction to β-CoOOH (e.g., O 1s ≈ 531.0 eV; Raman at ~694/488 cm^{-1}), illustrating the general point that an amorphous lattice tolerates, and indeed facilitates, the oxyhydroxide transition while maintaining adhesion and high-current operation. In situ/operando studies on cobalt oxides further emphasize that the route and extent of reconstruction toward CoOOH-like states can strongly correlate with OER activity, reinforcing why, reconstruction tolerance is a central structure-performance rationale for amorphous oxides [205].

A deliberately modest benchmark is Tao et al. [139], whose porous, poorly crystalline MoO_2 shows only weak reflections and moderate OER metrics (potential at 10 mA cm^{-2} decreasing from 2.808 → 2.414 V vs RHE when moving from 0.1 to 1.0 M KOH (Figure 17j). This provides a helpful structure comparison within oxides, porous/poorly crystalline can improve accessibility and lower resistance relative to fully crystalline parents, but the magnitude of the gain is strongly system-dependent and is not necessarily comparable to reconstruction-driven Co/Ni oxyhydroxide platforms [29]. The instructive point is conceptual: even when numbers aren't record-setting, amorphization and porosity reproducibly increase accessible under-coordinated sites and lower interfacial resistance relative to crystalline parents.

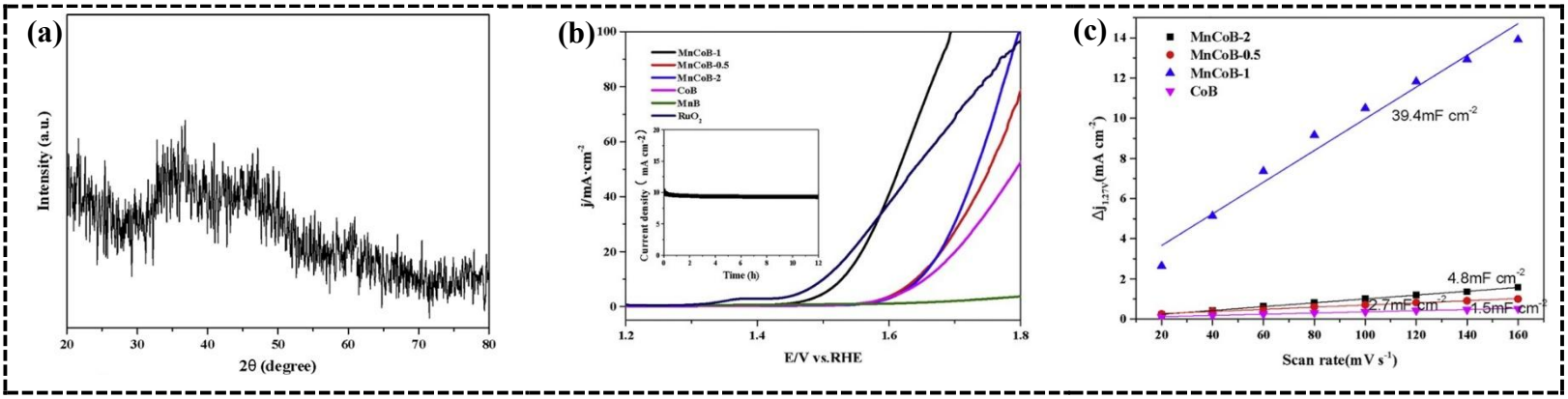

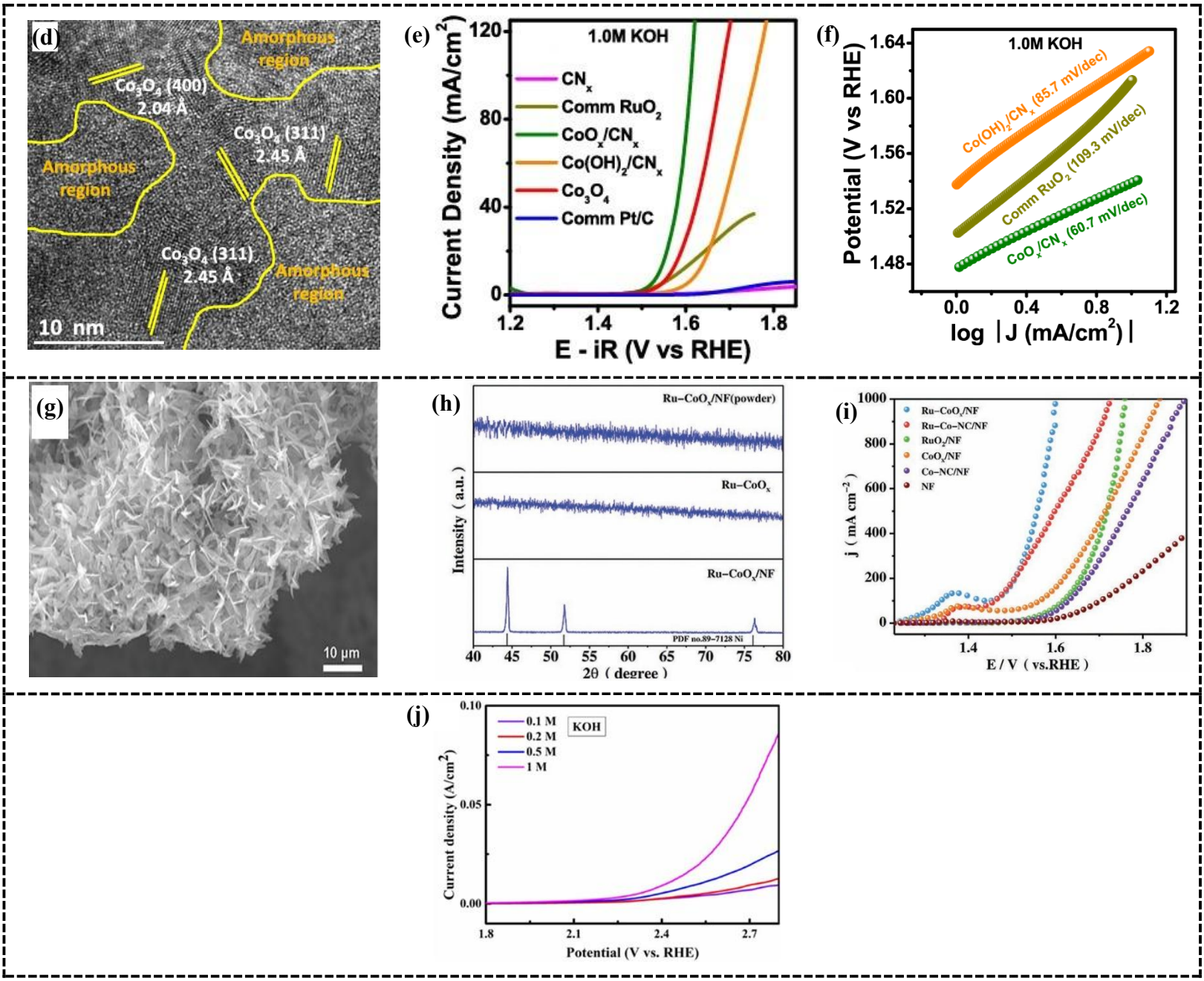

Figure 17. (a) XRD pattern of MnCoB; LSV curves (b) and current density vs. scan rate plot (c) for materials [201]. (d) HRTEM micrograph of CoO_x /CN_x; (e) LSV curves of synthesized materials in 1 M KOH; (f) Tafel slope of synthesized structures [202]. (g) SEM micrograph of Ru-CoO_x/NF; (h) XRD patterns of Ru-CoO_x and Ru-CoO_x/NF; (i) LSV measurement of manufactured structures in 1 M KOH [203]. (j) LSV analyses of MoO_2 in different electrolytes [139].

Amorphous sulfides commonly act as catalysts that restructure to oxy(hydroxide)-like skins under OER, and their initial disorder aids both this transformation and charge transport. This sulfide-to-oxy(hydroxide) skin, pathway has been repeatedly emphasized as the dominant structure-performance rationale for sulfides in alkaline OER, where surface oxidation generates the active oxyhydroxide while the sulfide core/backbone supports conductivity and mechanical integrity [206].

Using a binder-free route, Kale et al. [207] deposited composition-tunable (Co_3Mn_2)S nanosheets. The film remains amorphous post-OER while the surface oxidizes, a behavior that coincides with η_{10}/η_{50} = 243/290 mV (Figure 18a); a "house-of-cards" nanosheet network yields high ECSA (~280 cm^2) and R_{ct} that decreases with bias, rationalizing the kinetics and ~88% Faradaic efficiency. This is also an electrode-structure comparison point, binder-free nanosheet networks on conductive substrates often outperform powder/binder films on planar electrodes at high current density because they provide continuous electronic percolation and reduce bubble-induced site blocking [208].

Pushing hierarchical design, researchers, built sulfate-intercalated FeNiS@FeS LDH nanoflowers (Figure 18c) [209]; without repeating the entire structural suite, the headline results, η_{50}/η_{100} = 226/234 (Figure 18d) mV, $R_{ct} \approx 1.2\ \Omega$ (Figure 18e), and 50 h at 50 mA cm^{-2}, show what interfacial synergy in an amorphous heterostructure can do, including j = 500 mA cm^{-2} at ~322 mV. In terms of structure-performance comparison, this example highlights why heterostructures (FeNiS@FeS coupled with LDH features) are often more effective than single-phase sulfides: interfacial bonding and mixed-valence pathways can accelerate charge transfer during oxyhydroxide formation while the hierarchical morphology maintains electrolyte access at large j.

Additionally, Maghool et al. [210] converted a Ce-doped ZIF-67 into an amorphous Ce-CoS. MOF-derived sulfides are frequently discussed as "pre-organized" architectures in which amorphization plus heteroatom/dopant incorporation creates abundant accessible motifs and short diffusion paths, offering a meaningful comparison against conventional bulk sulfides [211]. At 1.0 M KOH the catalyst reaches η_{100} = 291 mV as it is obvious in Figure 18b and markedly lower R_{ct} (~3.8 Ω) than crystalline intermediates; 10 h chronopotentiometry with preserved morphology supports the view that amorphization and S incorporation improves carrier mobility and site accessibility. More broadly, surveys of transition-metal sulfides for oxidation electrocatalysis also stress that controlled surface oxidation to active oxyhydroxide layers, enabled by conductive sulfide backbones, is a recurring reason sulfides remain competitive OER precatalysts [212].

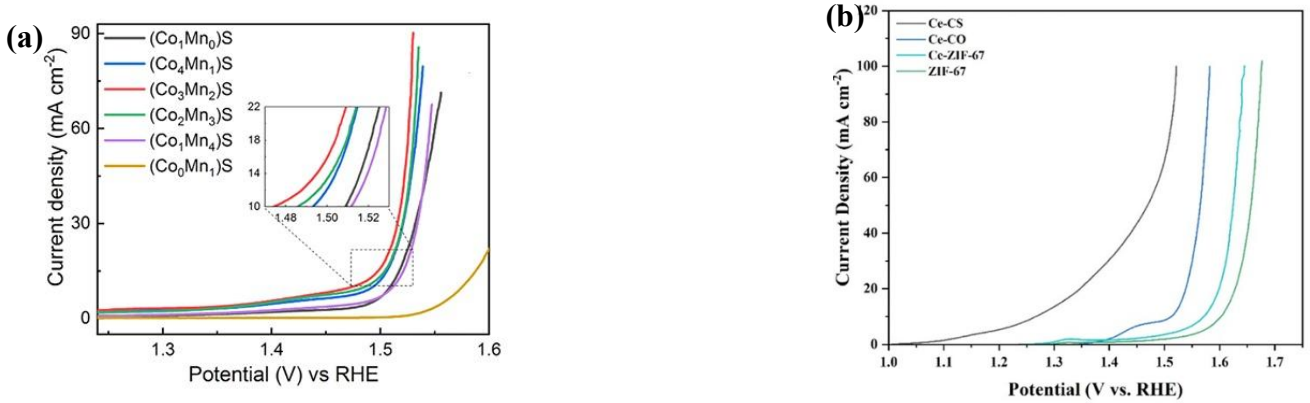

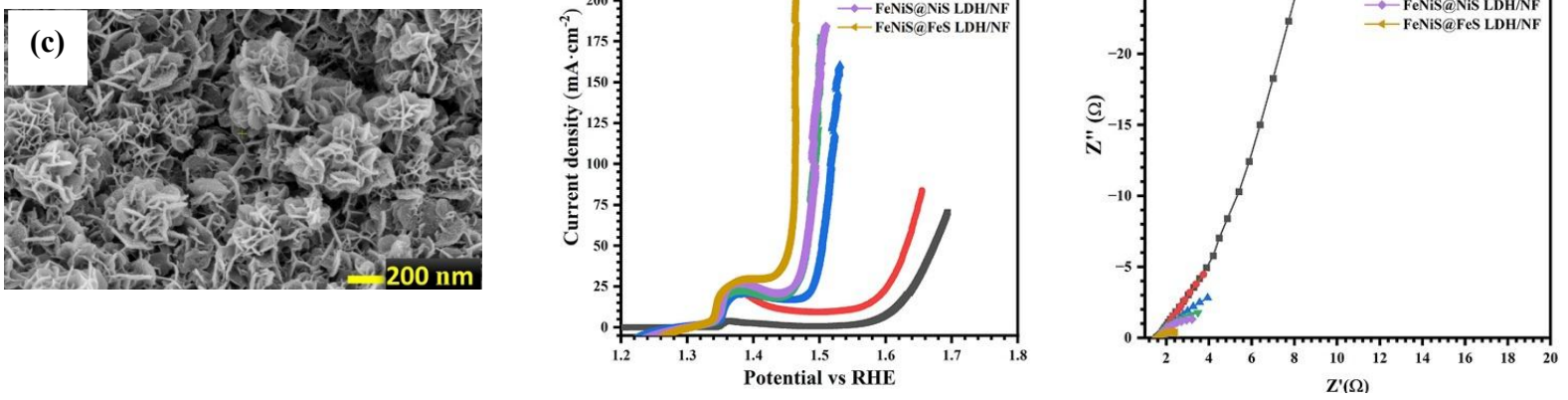

Figure 18. (a) LSV measurement of manufactured materials [207]. (b) LSV polarization of ZIF-67, Ce-ZIF-67, Ce-CO, Ce-CS [210]. (c) SEM image of FeNiS@FeS/NF; LSV curves (d), and Nyquist plots (e) of FeNiS@FeS LDH/NF, FeNiS@NiS LDH/NF, FeNiS LDH/NF, FeS LDH/NF, NiS LDH/NF, and NF [209].

Two multicomponent systems further illustrate disorder-assisted kinetics. Researchers reported amorphous NiFeCo oxyhydroxide from a room-temperature sol-gel [213], as shown in Figure 19a and Figure 29b η_{10} is 234, larger C_{dl}, smaller R_{ct}, and durable ~100 h operation; Co-induced high-valent centers stabilized by the amorphous matrix are implicated, and anion exchange membrane water electrolyzer tests corroborate device-level relevance.

Han et al. [214] pushed to a high entropy limit: FeCoCrMnBS nanosheets on Ni foam (Figure 19b) become explicitly amorphous after B/S co-doping, with enriched oxygen-vacancy signatures; η_{50}/η_{100} = 277/290 mV (Figure 19c), $C_{dl} \approx 6.25$ mF cm^{-2}, and 120 h stability (Figure 19d) underline how heteroatom-driven disorder optimizes intermediate binding. This high-entropy example also strengthens the, electrode-format comparison in OER, constructing an amorphous nanosheet array directly on Ni foam improves electronic percolation and electrolyte/bubble transport relative to powder films on planar substrates, which is especially relevant for the η_{100} and durability metrics emphasized here.

Pooling multiple metals within an amorphous scaffold adds a second lever, site diversity, on top of disorder. In one study, high entropy MOF electrodeposited on Ni foam and phosphidized it to yield amorphous FeCoNiCuY-phosphide/C nanosheets (Figure 19e) [215]. With the amorphous state established by PXRD/HRTEM and local coordination tuned by XANES/EXAFS, the catalyst posts η_{10}/η_{100} = 259/316 mV, R_{ct} ~0.98 Ω, and >150 h durability (Figure 19f). This example also provides an electrode-type comparison: electrodeposition/phosphorization directly on Ni foam minimizes binder/contact penalties and improves current distribution, which is especially important when interpreting long-duration durability in OER [215]. More broadly, phosphide-derived OER catalysts are often discussed as precatalysts that form (oxy)hydroxide-rich skins under bias, so part of the durability advantage can reflect how well the amorphous multimetal backbone maintains adhesion and electronic pathways during this surface evolution [216].

Pushing a trimetal P-O network, Chen et al. grew amorphous NiMoCu-PO directly on Ni foam and achieved η_{10} = 218 mV (Figure 19g), C_{dl} ~16.1 mF cm^{-2}, R_{ct} ~1.58 Ω, and ~100 h stability [217]. This NiMoCu-PO case is a useful structure comparison against the FeCoNiCuY-phosphide/C

nanosheets above, both exploit amorphous multimetal environments, but the P-O framework explicitly incorporates polyanion chemistry that can stabilize high-valent M-O motifs during OER while retaining a disordered backbone [218]. Post OER spectra show reinforced Ni(III)-O features and fading phosphate/MoO_4^{-2} bands, consistent with a robust amorphous backbone that reconstructs into the active skin without losing adhesion. This reconstructs without losing adhesion, point is precisely where amorphous backbones can outperform more brittle crystalline analogues, because disorder can accommodate local strain during repeated oxidation-state cycling [128].

Finally, a metal rich but ligand free example: researchers obtained an amorphous FeCoNi aerogel by spontaneous $NaBH_4$ gelation [219]. Aerogels provide a distinct electrode-structure comparison versus foam-supported coatings: the catalyst itself forms a self-supporting, reducing the reliance on an external scaffold to maintain electronic connectivity. On carbon paper it delivers η_{10} = 235 mV as shown in Figure 19h, R_{ct} ~6.1 Ω, very large C_{dl} ~131 mF cm^{-2}, and 40 h (Figure 19i) / 5000-cycle stability, showing how 3D percolation plus disorder yield both high ECSA and intrinsic activity. Heat-induced crystallization degrades performance at similar morphology, isolating amorphization as the decisive factor. This crystallization degrades at similar morphology, control is particularly valuable for the referee's requested structure–performance comparison, because it helps decouple amorphous-state effects from purely geometric surface-area effects.

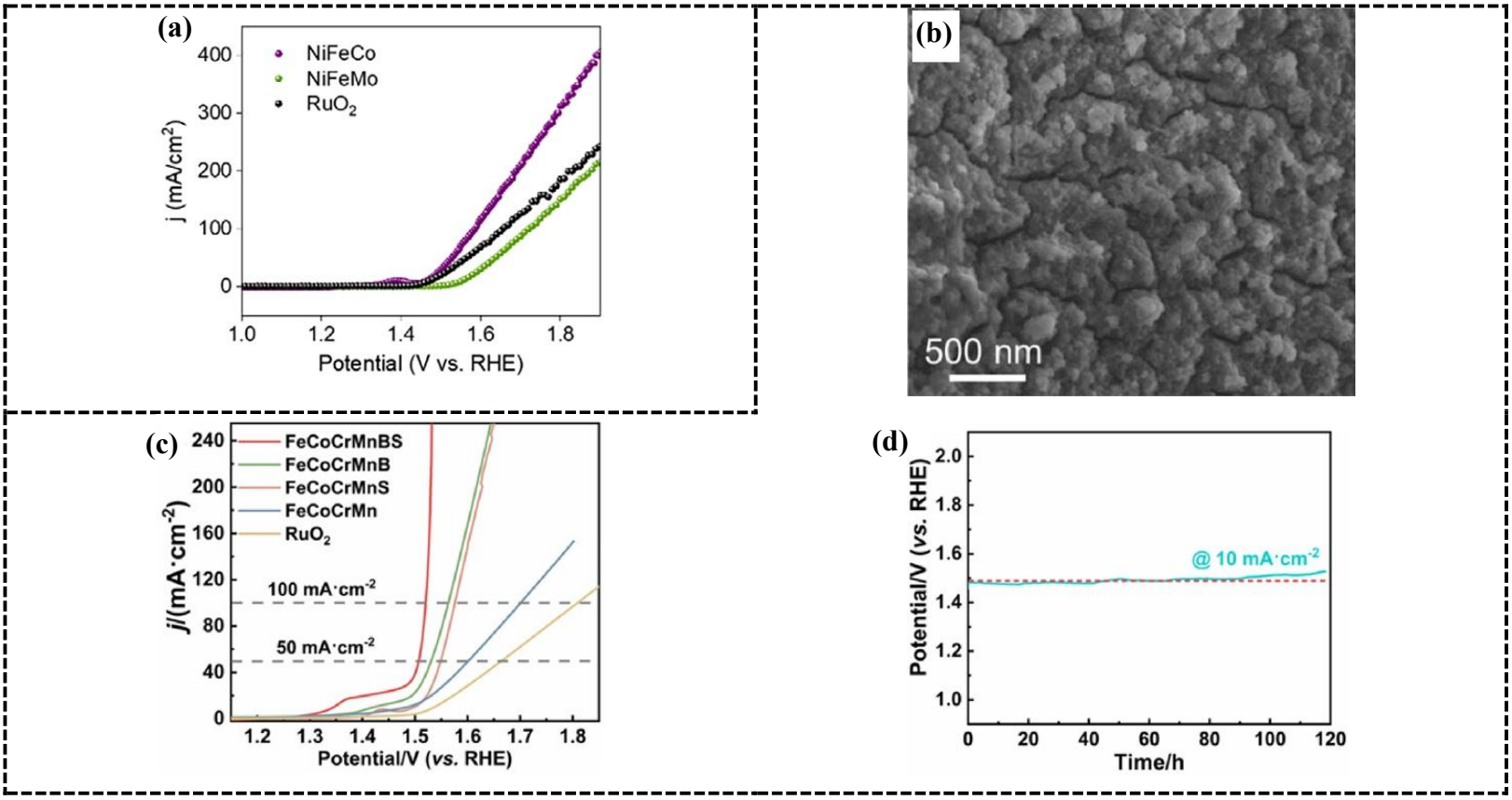

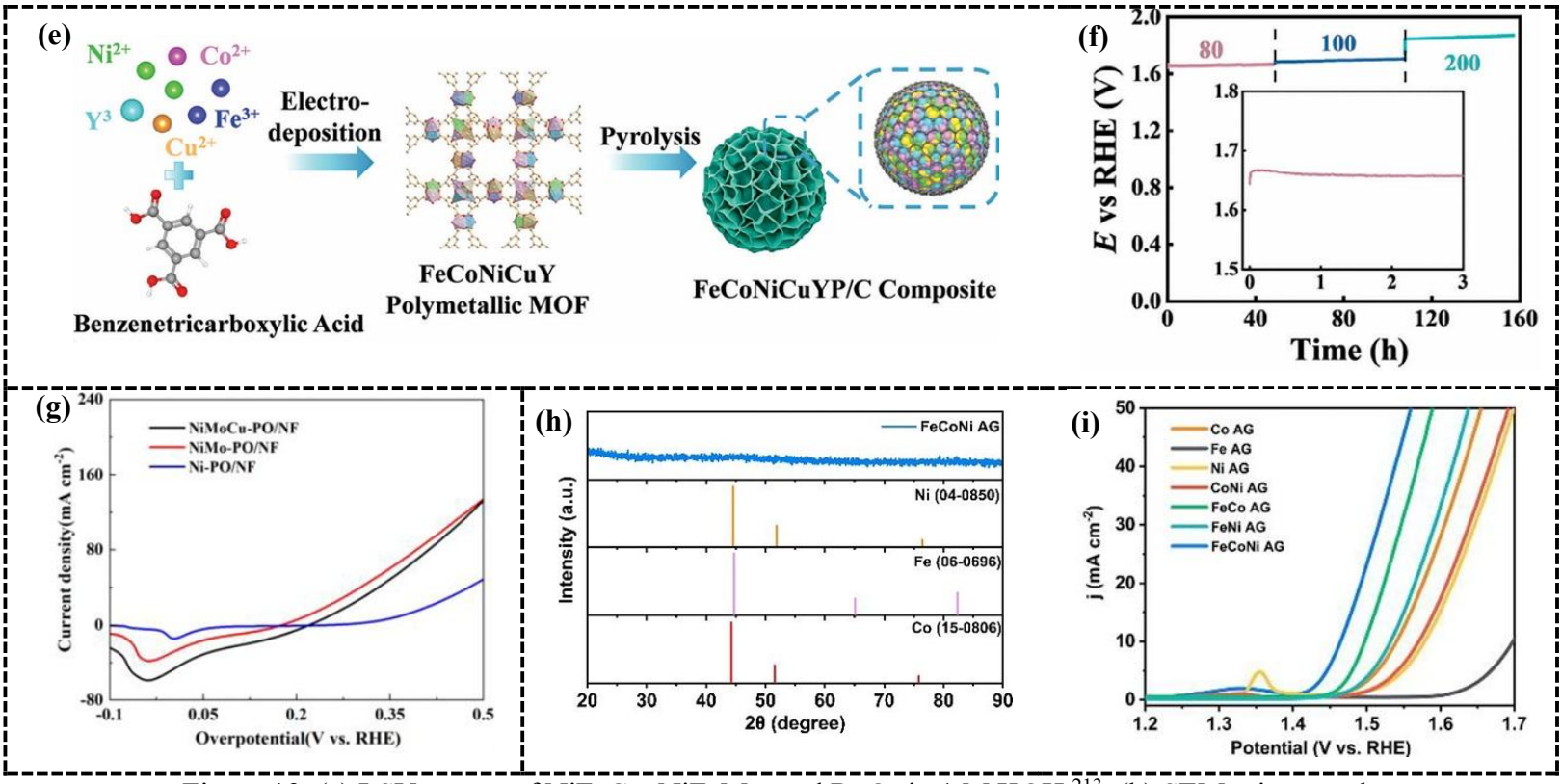

Figure 19. (a) LSV curves of NiFeCo, NiFeMo, and RuO_2 in 1 M KOH [213]. (b) SEM micrograph of FeCoCrMnBS; (c) electrochemical LSV analyses of different structures in 1 M KOH; (d) Chronopotentionetry test of FeCoCrMnBS/NF [214]. (e) FeCoNiCuYP/C synthesis process; (f) Chronopotentiometry test for FeCoNiCuYP/C, inset: local amplification of initial 3 h [215]. (g) LSV curves of NiMoCu-PO/NF, NiMo-PO/NF, and Ni-PO/NF [217]. (h) XRD pattern of FeCoNi; (i) Electrochemical polarization of manufactured structures [219].

All in all, across very different chemistries and synthesis routes, the disordered electrodes reach lower overpotentials at 10 mA cm^{-1}, keep sensible Tafel slopes, and stay stable at high current for long tests, often better than their crystalline counterparts made under similar conditions. The common ingredients behind those gains are straightforward: a defect rich, adaptable lattice; intimate, binder-free contact with the current collector; and, where used, mild composition tuning to balance adsorption. With those elements in place, amorphous design is a reliable and broadly applicable route to efficient, durable OER anodes.

The OER comparison table (Table 3) compiles, for each study, the catalyst (and support), electrolyte, η at 10 mA cm^{-2}, a representative high-current benchmark, and durability. Across amorphous materials, ,η_{10} generally lies in the ~200-320 mV range with moderate Tafel slopes (~50-95 mV dec^{-1}) and stable operation at elevated current densities. Overall, the table underscores the practical advantage of amorphous backbones: they accommodate in-situ reconstruction to active oxy(hydroxide) layers while maintaining adhesion and charge transport, and mild compositional/anion tuning further optimizes intermediate binding and long-term stability.

Table 3. Performance of different amorphous electrocatalysts in OER process in 1.0 M KOH.

Catalyst (Support)	η at 10 mA cm^{-2} (mV)	High-j point (mV)	Stability	Reference

Mo–NiFeP (Ni–Fe foam)	207	η_{1000} = 330	21 h @10 mA cm^{-2}; 20 h @500 mA cm^{-2}	198
Co–$FePO_4$ (GCE)	320	—	32 h @10 mA cm^{-2}	200
MnCoB-1 (GCE)	292	—	12 h @10 mA cm^{-2}	201
CoO_x/CN_x (GCE)	310	—	24 h + 100 h	202
Ru–CoO_x(Ni foam)	220	η_{1000} = 370	100 h i–t + 10000 cycle	203
(Co_3Mn_2)S (stainless steel)	243	η_{50} = 290	100 h @10 mA cm^{-2}	207
FeNiS@FeS–LDH (Ni foam)	—	η_{100} = 234 (η_{500} = 322)	50 h @50 mA cm^{-2}	209
Ce–CoS (Ni foam)	—	η_{100} = 291	10 h @100 mA cm^{-2}	210
NiFeCo oxyhydroxide (Ni felt)	234	η_{100} = 356	100 h @ 20 mA cm^{-2}	213
FeCoCrMnBS HEH (Ni foam)	—	η_{100} = 290 (also η_{50} = 277)	120 h @10 mA cm^{-2}	214
FeCoNiCuYP/C (Ni foam)	259	η100 = 316 mV	≥150 h @100–200 mA cm^{-2}	215
NiMoCu-PO (Ni foam)	218	—	100 h @ mA cm^{-2}	217
FeCoNi aerogel (carbon paper)	235	—	5000 CV cycles	219

1.6.3 Overall water splitting

Overall water splitting provides the most stringent, device level benchmark for electrocatalysts, coupling HER and OER in a two electrode configuration where the practically relevant figures of merit are the cell voltage at defined current densities (e.g., 10 and 100 mA cm^{-2}), Tafel behavior, Faradaic efficiency, and long-term stability. In this section, we synthesize recent advances showing that amorphous architectures deliver competitive overall water splitting by combining high densities of unsaturated active sites with short charge/mass-transport pathways and an intrinsic capacity for benign operando reconstruction into the true active phase. Emphasis is placed on systems that achieve low cell voltages in alkaline media (often ≤1.6–1.7 V at 10 mA cm^{-2}) with multi-hour durability, including both symmetric and asymmetric pairings tailored for bifunctionality. Together, these studies illustrate a clear design rule: leverage amorphicity to decouple site density from transport limitations while permitting controlled surface evolution, thereby converting molecular-scale disorder into device-level performance.

Within the phosphide family, amorphous Co-Ni-P and Ni-Cu-P exemplify how short-range disorder and multimetal coupling can be leveraged to lower the cell voltage for overall water splitting while preserving durability. In the work of Chai et al. [220], a one-step aqueous electrodeposition on Ni foam yields porous, binder-free Co-Ni-P films whose amorphous nature is evident from the absence of Bragg reflections beyond the substrate peaks. This porous morphology

is consistent with dynamic hydrogen-bubble templating during electrodeposition, where transient H2 bubbles act as self-removing templates to generate high-surface-area, binder-free films that are advantageous for two-electrode operation [221]. The hydrogen-bubble templating produces a high-surface-area architecture, and surface XPS signatures consistent with air-exposed phosphides foreshadow the partial in-situ reconstruction that occurs under operation. Such reconstruction is also widely discussed for transition-metal phosphides in OER-containing cells, where the phosphide acts as a conductive precatalyst and forms an (oxy)hydroxide-rich skin under anodic polarization [222]. When configured as a two-electrode alkaline cell (1.0 M KOH), pairing composition-tuned films delivers 1.64 V at 10 mA cm^{-2} (Figure 20a) and retains performance over 10 h with only a modest voltage rise as shown in Figure 20b. This is a meaningful electrode-format comparison, binder-free films on 3D Ni foam typically reduce contact resistance and improve electrolyte/bubble transport relative to drop-cast powder electrodes, which becomes increasingly important in two-electrode operation. The authors argue that the amorphous matrix provides coordinatively unsaturated sites tolerant to reconstruction into (oxy)hydroxide/phosphate shells, while Co↔Ni electronic interactions tune Ni(II/III) redox and depress the OER onset, collectively enabling bifunctionality in a single materials platform.

Building on the same design logic but with a distinct chemistry, Hou et al. [223] prepare amorphous Ni-Cu phosphide (A-NCP) directly on Ni foam using a mixed ethylene-glycol/water solvent to suppress crystal nucleation (Figure 20c). Ni-Cu phosphide systems are a useful structure comparison within P-family bifunctional catalysts because Cu incorporation and amorphization can jointly reshape local bonding and electronic states while preserving conductive backbones for overall water splitting [224]. Here, the transition from crystalline to fully amorphous is captured by the evolution of XRD into broad halos and by diffuse selected area electron diffraction rings; the accompanying blue-shifted, broadened Ni-P/Cu-P Raman bands and core-level shifts in XPS indicate local disorder and charge redistribution between metal and P states. Electrochemically, A-NCP used as both electrodes reaches 1.64 V at 10 mA cm^{-2} as it is obvious in Figure 20d, withstands 5000 CV cycles, and sustains ~50 h of operation with minimal degradation (Figure 20e). This durability trend is consistent with the broader observation that self-supported, foam-integrated phosphide electrodes often retain performance by maintaining adhesion and electronic percolation even as surface chemistry evolves under OER/HER bias. Complementary DFT rationalizes the macroscopic gains: amorphization broadens Ni/Cu 3d states near the Fermi level, shifts the d-band center to optimize intermediate adsorption, equalizes OER barrier distributions, and lowers the water-dissociation barrier governing alkaline HER.

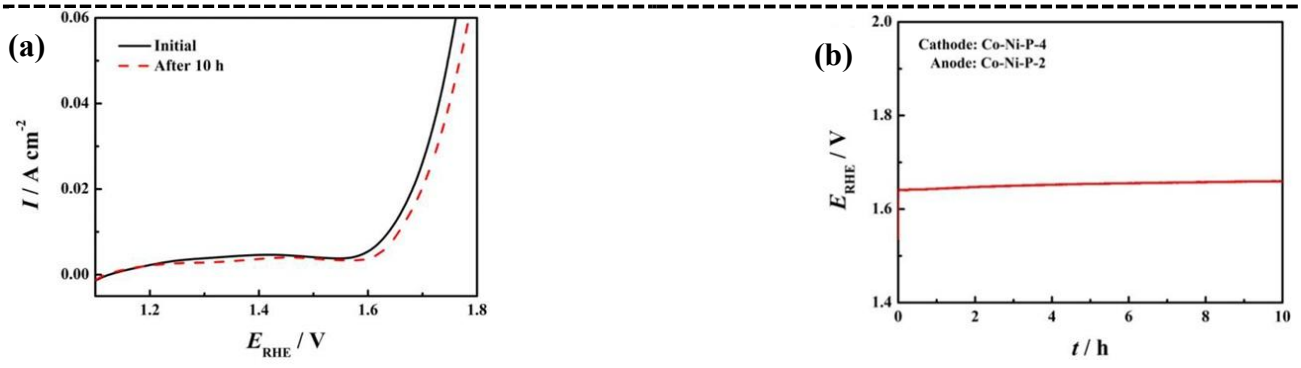

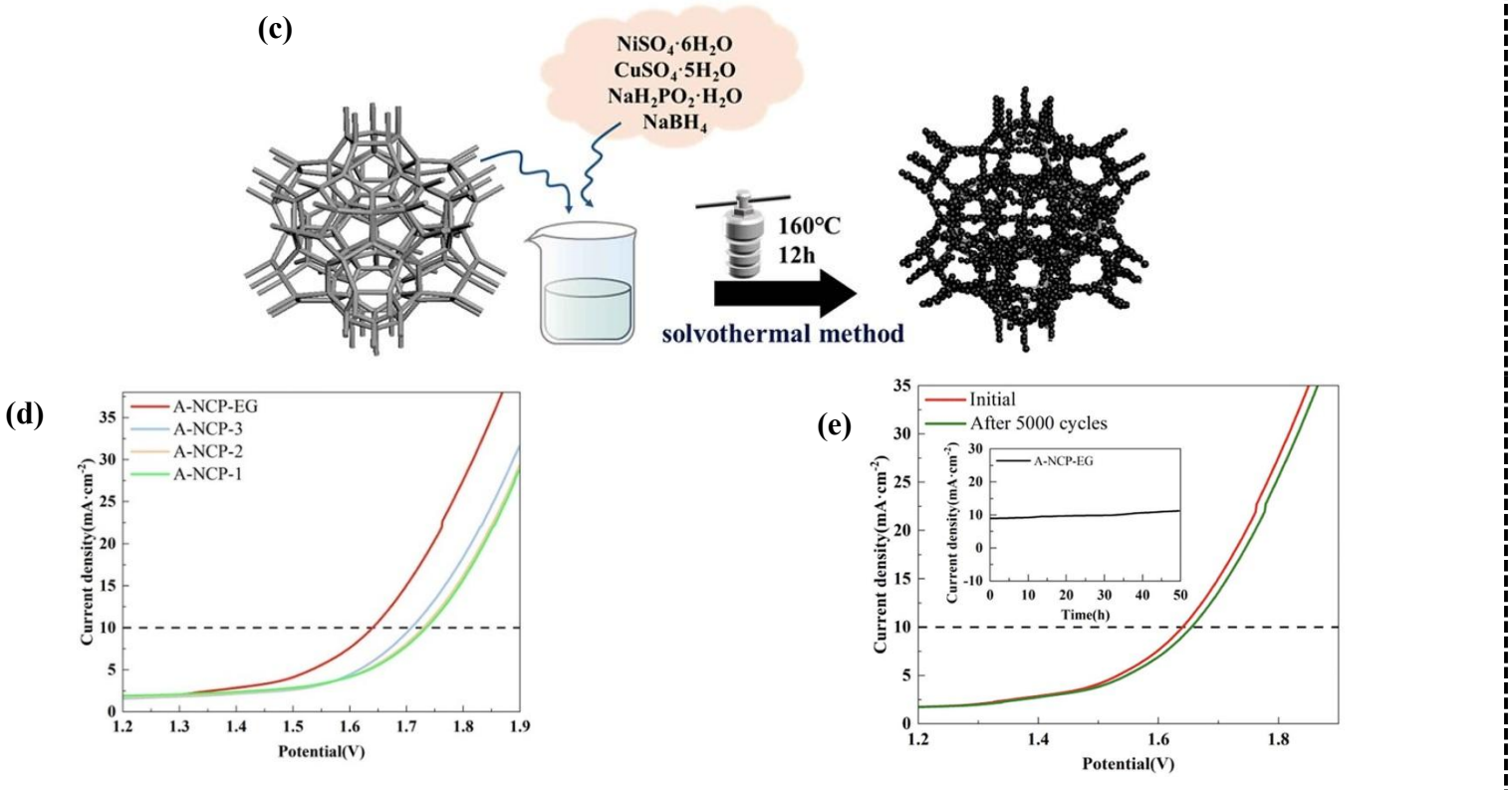

Figure 20. (a) LSV curves of materials before and after the 10 h galvanostatic test; (b) Long-term 10 mA cm^{-2} galvanostatic test of two-electrode system in 1 M KOH [220]. (c) Catalysts synthesis process; (d) Materials LSV curve of overall water splitting; (e) Stability tests of synthesized material in two-electrode system [223].

Across boride families, short-range disorder consistently translates into low cell voltages and durable operation in alkaline two-electrode configurations. This trend is repeatedly attributed to boride behavior, where the conductive boride backbone maintains charge transport while the surface evolves into catalytically competent (oxy)hydroxide layers under OER/HER bias [225]. Two representative studies, by Chen et al. [225] on amorphous CoB and Song et al. [226] on Ni_3P/Ni_3B anchored in an amorphous B-doped carbon layer (B-C) matrix, illustrate how boron-enabled amorphicity, interfacial reconstruction, and conductive backbones can be co-optimized to drive overall water splitting.

As Chen et al. reported. An electrolessly plated, ~4 μm amorphous CoB film on 3D Ni foam exhibits the canonical fingerprints of short-range order (featureless XRD, diffuse SAED, nonstoichiometric Co/B surface states by XPS). Under operating bias, the surface evolves selectively, toward CoOOH nanoplates during anodic polarization and $Co(OH)_2$ in cathodic conditions, while the CoB interior retains a metal-like conductivity. This is a particularly strong structure-performance comparison because it separates roles within the same electrode, the skin provides catalytic functionality, while the amorphous CoB interior preserves electronic percolation during long-term two-electrode operation [225]. This "amorphous shell → (oxy)hydroxide skin" transformation reduces interfacial resistance and expands the electrochemically accessible area, conferring genuine bifunctionality in a symmetric two-electrode cell. In 1 M KOH the device reaches 10 mA cm^{-2} at 1.69 V as it is obvious in Figure 21a, and holds ~36 h at 20 mA cm^{-2} with

only a modest voltage rise (Figure 21b). Because this is a gas-evolving two-electrode configuration, the 3D foam format is also an electrode-type advantage, porous current collectors are well known to reduce bubble-induced blockage and ohmic/mass-transfer losses compared with planar electrodes, improving apparent cell voltage at practical currents [227]. The performance gain is credibly tied to the defect-rich, coordinatively unsaturated environment specific to amorphous CoB, which accommodates rapid formation of catalytically competent $CoOOH/Co(OH)_2$ without compromising charge transport.

Ni_3P/Ni_3B on amorphous B-C (Song et al.). A complementary strategy embeds nanocrystalline Ni_3P/Ni_3B within a boron-doped amorphous carbon lamellae grown throughout Ni foam (Figure 21c). Here, crystallinity is confined to the active nanoparticles (indexed by XRD/HRTEM), while the B-C host remains amorphous and conductive. XPS indicates B-doping and robust Ni-P/Ni-B bonding; partial surface oxidation to (oxy)hydroxides under OER provides additional active moieties. The hierarchical scaffold (macro-porous foam + lamellar B-C + nanoparticle dispersion) minimizes bubble trapping and accelerates charge transfer (low R_{ct}, enlarged C_{dl}). Bubble-management arguments are especially relevant here because hierarchical porous electrodes are widely recognized to mitigate adhered-bubble inactivation during vigorous OER/HER, which directly supports the minimizes bubble trapping, mechanism you describe [228]. In 1 M KOH, a symmetric $Ni_3P/Ni_3B/B\text{-}C \| Ni_3P/Ni_3B/B\text{-}C$ cell requires 1.50 V for 20 mA cm^{-2} and 1.59 V for 50 mA cm^{-2} as shown in Figure 21d, sustaining ~89% of the initial current over 48 h at 1.59 V (Figure 21e), with Faradaic efficiencies near unity for both half-reactions. The central contribution of amorphicity here is twofold: (i) a defect-rich, B-doped carbon network that maintains high conductivity while maximizing interphase contact with the boride/phosphide domains, and (ii) chemical tolerance to in-situ remodeling, enabling stable operation at low voltages.

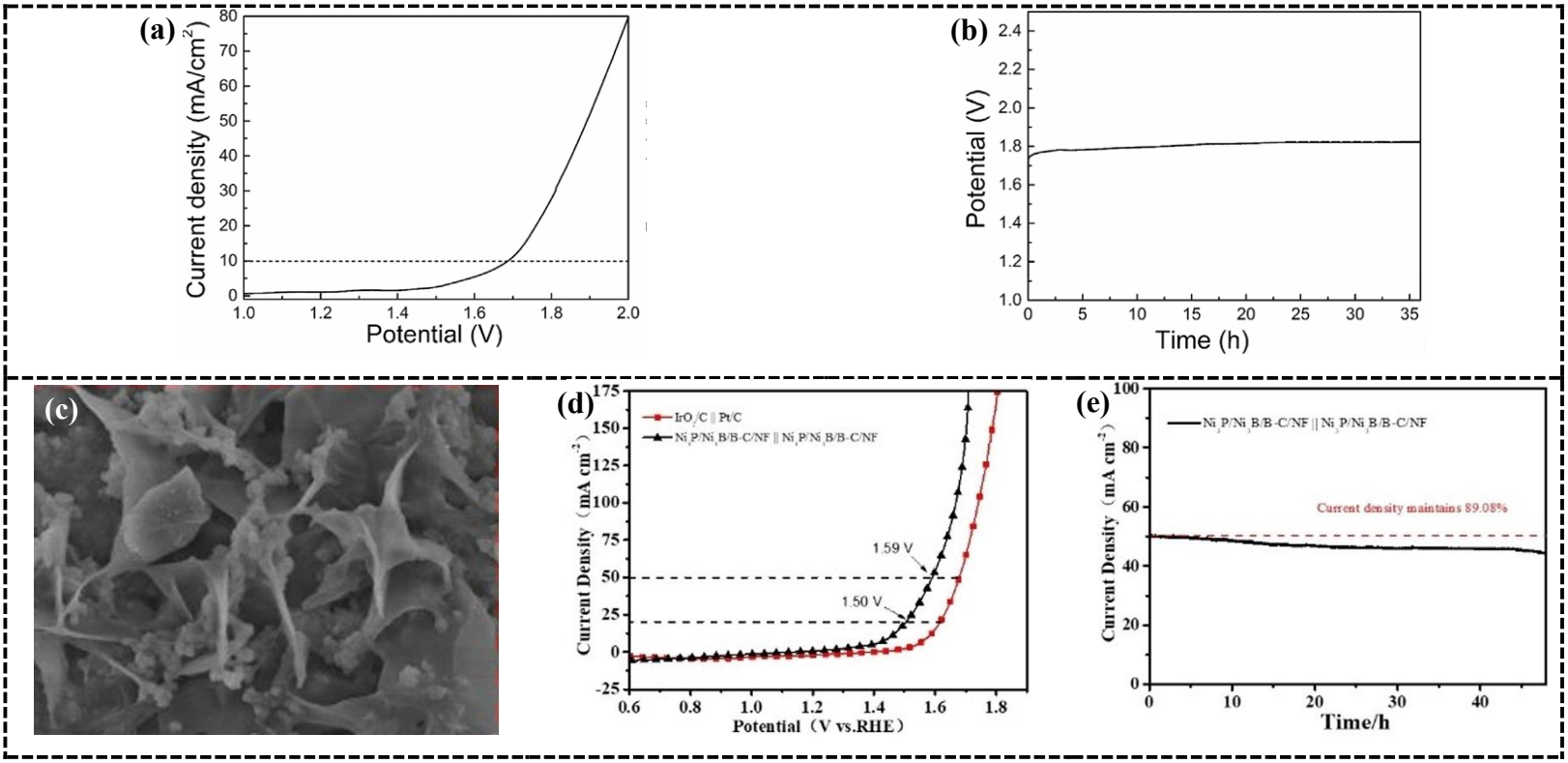

Figure 21. (a) LSV charts of the CoB-derived electrocatalysts in a two electrode configuration; (b) Chronopotentiometric test of synthesized material in two-electrode system [225]. (c) FESEM image of Ni_3P/Ni_3B/B-C/NF; (d) Ni_3P/Ni_3B/B-C/NF|| Ni_3P/Ni_3B/B-C/NF and Pt/C||IrO_2/C LSV curves; (e) i-t chart at1.59V for Ni_3P/Ni_3B/B-C/NF|| Ni_3P/Ni_3B/B-C/NF [226].

Among amorphous chalcogenides, Co-Ni-S nanostructures stand out for delivering bifunctionality without sacrificing transport. In Dong et al. [184], vertically aligned Co-Ni-S nanoflake arrays grown on carbon cloth combine atomic-scale Co/Ni mixing with a defect rich, long range disordered framework. Carbon cloth is also a meaningful electrode-type comparison point here, because its woven filament network can support binder-free growth, high areal loading, and robust mechanical/electrical percolation relative to planar drop-cast electrodes. The result is an electrolyzer that reaches 10 mA cm^{-2} at 1.60 V in 1 M KOH as shown in Figure 22a, surpassing a RuO_2‖Pt/C benchmark. Such cell-voltage advantages in two-electrode tests are often amplified by self-supported nanoflake arrays, because vertically aligned architectures and open porosity improve electrolyte access and mitigate bubble-induced site blocking under vigorous gas evolution [96].

Beyond the headline voltage, the authors show ∼96% voltage retention over 35000 s (Figure 22b) and near quantitative gas evolution (H_2:O_2 ≈ 2:1), indicating that the amorphous phase does not trade activity for durability. Post operando surface analysis captures the characteristic evolution of amorphous sulfides, partial formation of oxyhydroxide motifs, consistent with facile rearrangement under bias. Operando-focused reviews on non-oxide OER catalysts further emphasize that controlled surface reconstruction (rather than complete bulk oxidation) is often the key to sustaining activity while avoiding loss of adhesion or conductivity. Here, amorphicity manifests in three practical levers: (i) dense unsaturated Co/Ni sites, (ii) atomic-level alloying that tunes H*/OH* adsorption, and (iii) mechanical/structural compliance that accommodates reconstruction without passivating the surface.

A complementary strategy is to engineer asymmetric sulfide pairs while preserving disorder. He et al. [229] construct N-doped (Co-Cu)S_x on Cu foam as the OER anode, paired with N-CoS/Cu_2S as the HER cathode. Cu-foam-based electrodes are frequently highlighted as advantageous current collectors for water electrolysis because their three dimension network improves current distribution and mass transport while providing abundant anchoring sites for catalyst growth [230]. Synthesis intentionally induces amorphicity and porosity (electro-oxidation → co-deposition of $Co(OH)_2$ → thiourea-assisted sulfidation and N-doping), yielding super-hydrophilic, 3D nanoarchitectures with strong interfacial electronic coupling between Co and Cu. This "asymmetric electrode pairing" also provides situation that each electrode is separately optimized for its half-reaction while still leveraging disorder-enabled reconstruction. This cell operates at just 1.53 V (10 mA cm^{-2}) (Figure 21c) and sustains ∼20 mA cm^{-2} for 24 h with negligible decay. Mechanistic probes point to operando transformations, CoOOH like species on the anode and $Co(OH)_2$ like motifs on the cathode, supported by N induced electron withdrawal and oxygen vacancy signatures that accelerate OER kinetics. Relative to crystalline controls, the amorphous, defect rich framework provides a larger population of catalytically competent Co sites and lowers charge transfer barriers, explaining the unusually low cell voltage.

Pursuing oxide platform, Li et al. [231] deposit an amorphous Co-Fe oxide conformally on 2D black phosphorus (BP). This CoFeO@BP platform is a useful "electrode-structure" comparison to foam-supported coatings, because a 2D support can enforce ultrathin conformal growth and strong interfacial contact, helping decouple intrinsic phase effects from macroporous current-collector

effects. The thin (~3.5 nm), vacancy-rich amorphous layer uniformly blankets BP and avoids crystallization until forced by high-temperature annealing. In symmetric configuration, based on Figure 22d the cell delivers 10 mA cm^{-2} at 1.58 V and retains ~93% of its initial current over 24 h. This low-voltage symmetric-cell result aligns with the adaptive-mechanism interpretation reported for amorphous CoFe oxide on BP, where the metastable amorphous oxide can access different active states under reducing vs oxidizing bias. Importantly, the amorphous film is mechanistically adaptive: under HER bias it partially phosphidizes to Co_2P at the interface, whereas under OER it engages a lattice oxygen pathway, both enabled by the disorder and oxygen vacancy landscape. Bias-contingent evolution (phosphidation under HER vs oxygen-lattice involvement under OER) is increasingly emphasized as a hallmark of metastable/disordered catalysts, which can reconcile apparently "contradictory" requirements of bifunctionality within a single material. In particular, recent mechanistic discussions distinguish lattice-oxygen participation from purely adsorbate-mediated OER pathways and highlight how oxygen-vacancy chemistry can influence these routes, consistent with your oxygen-vacancy/LOM framing here [232]. This bias contingent evolution, a hallmark of metastable amorphous oxides, helps explain the unusual coupling of low voltage and robustness.

Moreover, Samanta et al. [202] demonstrate that coupling disorder with conductive carbon can substitute for precious-metal cathodes in a two-electrode cell. This CoO_x/CN_x case provides a clear electrode-type comparison because the conductive carbon host supplies continuous electronic percolation for a largely amorphous oxide phase, reducing the need for precious-metal cathodes in alkaline pairings. Their 2D amorphous CoO_x/N-doped carbon sheets, obtained by chemical reduction and mild calcination, show strong CoO_x, carbon interaction and enlarged electrochemically accessible area. In 1 M KOH, the device spans a spectrum of pairings: CoO_x/CN_x‖Pt/C requires 1.65 V (10 mA cm^{-2}) (Figure 22e); pairing the anode with a cycled CoO_x/CN_x cathode (post HER activation) rises to 1.81 V; a fully symmetric CoO_x/CN_x‖CoO_x/CN_x cell operates at 1.93 V. Presenting these three pairings is especially helpful for structure-performance comparison, because it isolates how much of the cell voltage penalty arises from replacing Pt/C with an activated amorphous-carbon-coupled cathode while keeping the anode constant. Chronopotentiometry to ~100 h underscores durability as shown in Figure 22f; notably, the carbon coupled amorphous sheets improve with conditioning, again consistent with controlled reconstruction of non-crystalline oxides into more active surface states. Such conditioning-induced performance gains are consistent with the broader reconstruction literature on amorphous oxides, where the steady-state active surface can differ from the as-synthesized state even when bulk amorphicity is retained [20].

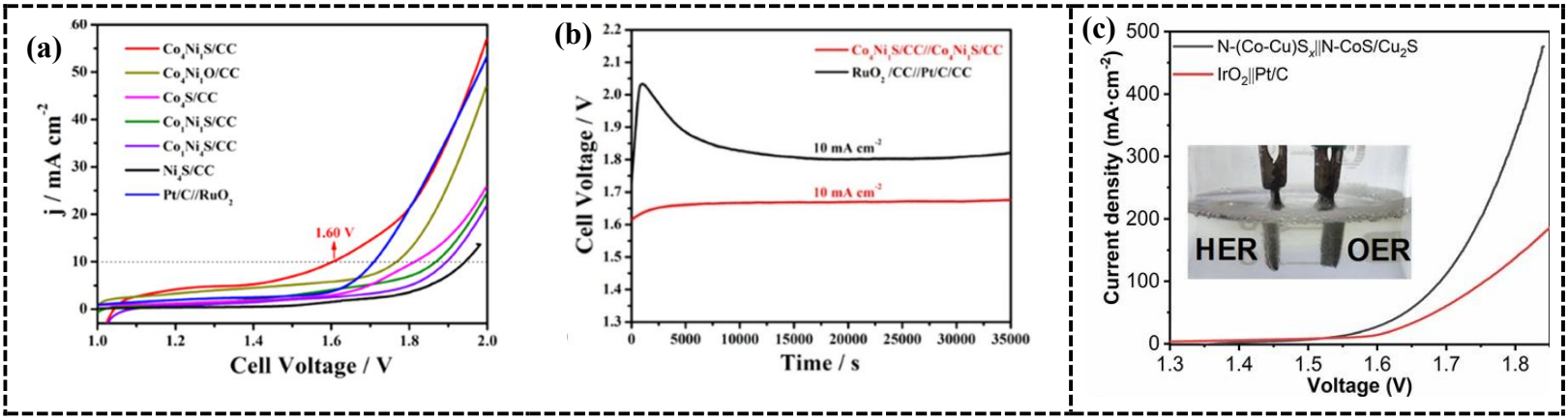

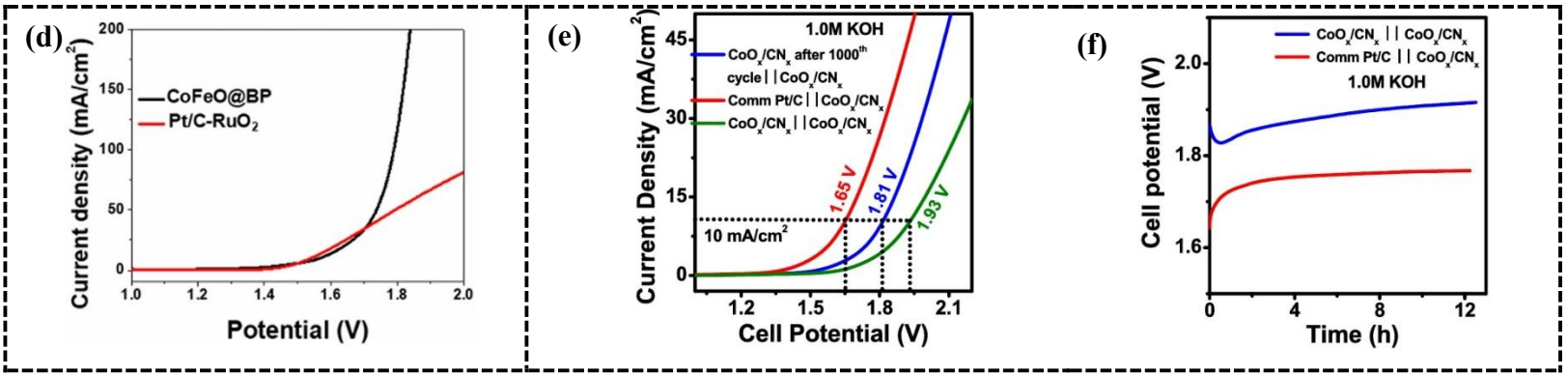

Figure 22. (a) LSV curve of synthesized structures in 1 M KOH; (b) Co_4Ni_1S/CC and Pt/C//RuO_2-based chronopotentiometry curves electrolyzer [184]. (c) Polarization charts of N-(Co Cu)S_x||N-CoS/Cu_2S and noble metal IrO_2||Pt/C electrodes in 1 M KOH and (inset) photo of N-(Co–Cu)S_x||N-CoS/Cu_2S in water splitting process [229]. (d) Polarization curves of CoFeO@BP and Pt/C-RuO_2 [231]. (e) Overall water splitting polarization curves of synthesized materials; (f) chronopotentiometric stability plots of materials [202].

Multi-component intermetallic networks that incorporate controlled disorder can deliver bifunctional activity and durability beyond conventional binary alloys. A representative example is the defect-engineered CoCuMoNi system reported by Wu and co-workers[233] , obtained by arc-melting Co-Cu-Mo-Ni-Al followed by chemical de-alloying to remove Al and unlock a 3D nanoporous, multi-intermetallic heterostructure. This "alloying-dealloying" route to highly porous CoCuMoNi intermetallic alloys with abundant defect sites has been explicitly highlighted as an effective strategy for overall water splitting in the corresponding Advanced Science report. The de-alloyed scaffold exposes a high density of heterojunctions and short-range disordered regions along polycrystalline boundaries, creating internal electric fields and facilitating interfacial charge redistribution. Heterojunction-driven built-in electric fields are widely recognized to promote interfacial electron transfer and improve intrinsic catalytic activity in dual-functional water electrolysis, supporting the internal-field argument made here [234]. These electronic perturbations rationalize the catalyst's multisite behavior under two-electrode operation, in which adsorption energetics at metal-metal interfaces are tuned without sacrificing transport through the open, percolating framework. In alkaline overall electrolysis (1.0 M KOH), symmetric cells employing this single material at both electrodes achieve a cell voltage of ~1.56 V at 10 mA cm^{-2} (Figure 23a). This cell-voltage level is consistent with the reported performance of defect-engineered nanoporous CoCuMoNi multi-intermetallic heterostructures in symmetric overall water splitting tests. Faradaic efficiencies approach the theoretical values and multistep chronopotentiometry shows rapid stabilization with minimal drift over day-scale operation. The key message is that interfacial engineering in multi-intermetallic matrices, together with defect-assisted short-range disorder, delivers intrinsically bifunctional sites and robust charge transfer, enabling low overpotentials at practical current densities in full-cell mode.

A complementary strategy is to leverage fully amorphous matrices that stabilize active sites and buffer structural reorganization under bias. Vijayarangan and colleagues[157] convert a crystalline Co-pyridine precursor into amorphous cobalt-impregnated, nitrogen-doped carbon nanochains (Co@NC) by thermal treatment at 500 °C. This Co@NC nanochain platform is also a clear electrode-structure comparison to powder catalysts, the percolating carbon nanochain network provides continuous electronic pathways and mechanically anchors Co sites, which helps preserve

conductivity and suppress catalyst detachment during vigorous gas evolution in two-electrode operation. The resulting percolating nanochain network encapsulates Co domains within an N-doped carbon matrix, increasing the density of defect sites while maintaining electronic connectivity. Only a subset of characterization is essential to make the point: loss of long-range order (XRD/SAED) confirms amorphization; XPS evidences mixed Co^{2+}/Co^{3++} states and multiple N configurations that support strong Co-N-C coordination. In a symmetric alkaline cell (1.0 M KOH), Co@NC reaches 1.60 V at 10 mA cm^{-2} as it is obvious in Figure 23b, surpassing Pt/C||IrO2 and the crystalline precursor couple; stability is sustained for ≥120 h with only minor potential growth (Figure 23c), and gas evolution remains near-stoichiometric. Here, amorphization is not a passive by-product: short-range disorder and Co-N-C coordination jointly modulate adsorption at H_2/O_2 evolution sites while the carbon sheath mitigates corrosion, yielding durable, bifunctional performance in overall electrolysis.

In an earlier but instructive study, Yang et al.[235] embed ultrasmall Ru/Cu-doped RuO_2 nanodomains in an amorphous carbon skeleton derived from a Ru-modified Cu-BTC MOF. This MOF-derived "Ru/Cu-RuO_2 nanodomain + amorphous carbon skeleton" architecture is a useful structure-format comparison to conventional RuO_2 particles, because nanoscale confinement in an amorphous carbon host increases dispersion and shortens transport lengths while preserving robust conductive pathways at the device. A brief oxidative step followed by selective etching establishes Ru/RuO_2 interfaces while retaining a disordered carbon framework with open mesoporosity. Rather than detailing every measurement, it suffices to note two pillars: (i) the amorphous scaffold ensures high dispersion and mass-transport channels, and (ii) Cu incorporation downshifts the Ru d-band center on RuO_2(110), reducing the theoretical OER overpotential. This "Cu-tuned RuO_2 electronic structure" rationale is consistent with broader RuO_2-doping analyses, where Cu dopants shift Ru electronic states and can weaken overly strong Ru-O interactions while introducing oxygen vacancies/unsaturated Ru sites that improve OER kinetics [236]. In two-electrode alkaline tests (1.0 M KOH), the optimized sample delivers ~1.47 V at 10 mA cm^{-2} and ~1.67 V at 100 mA cm^{-2} as it is obvious in Figure 23d, with long-term current retention under constant cell bias (Figure 23e). For context, recent Ru-based bifunctional systems that combine RuO_2-derived domains with oxide/carbon coupling also report ~1.49 V at 10 mA cm^{-2} and high-current durability, reinforcing that "RuO_2 + engineered amorphous/heterointerfaces" is an effective pathway to device-level performance at reduced noble loading. This work shows that: short-range disorder, when coupled to judicious electronic tuning (here via Cu on RuO_2) and nanoscale confinement in amorphous carbon, yields a coherent pathway to bifunctional improvement that is visible at the device level.

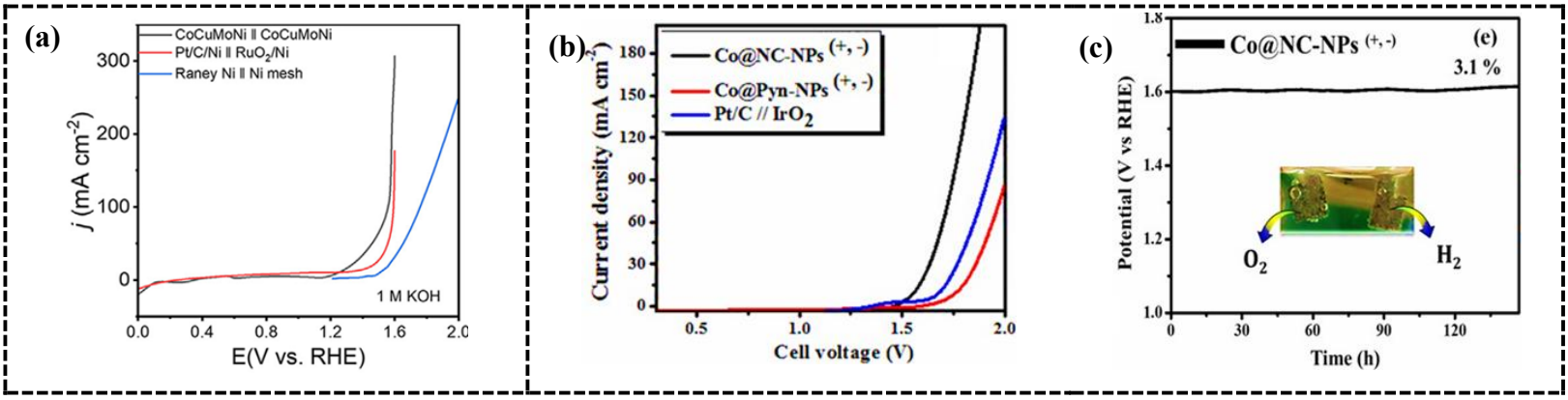

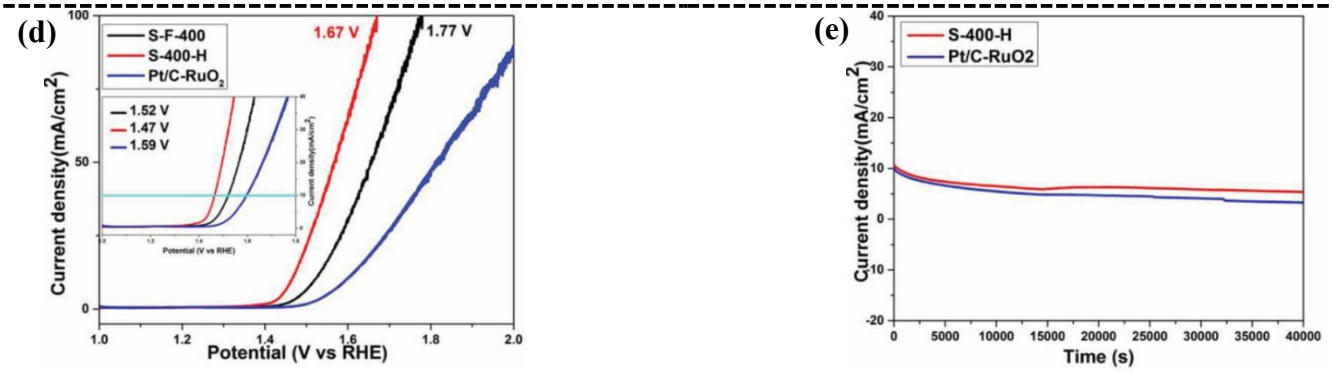

Figure 23. (a) Polarization curves of CoCuMoNi || CoCuMoNi and other electrodes [233]. (b) Polarization curves of synthesized materials; (c) Stability analysis of Co@NC-NPs$^{(+,-)}$[157]. (d) Overall water splitting polarization curves of synthesized materials; (e) chronoamperometric stability plots of materials [235].

All told, spanning different amorphous structures, the overall water-splitting cells converge on the same practical outcome: lower cell voltages at the 10 mA cm^{-2} benchmark, and hour-to-day-scale durability even as current is stepped to higher loads, often matching or surpassing crystalline analogues prepared under comparable conditions. The recurring enablers are clear: a defect-rich, short-range-ordered backbone that tolerates electrochemical reconstruction; intimate, binder-free electrical contact and open porosity for mass transport; and purposeful interfacial/electronic tuning (via multi-metal junctions, mild doping, or encapsulation in N-doped carbon) to balance adsorption energetics on both electrodes. Taken together, amorphous structure is a strong device-level design lever for overall water splitting across many chemistries, while acknowledging regimes where crystalline benchmarks remain preferred.

In Table 4 results for the two-electrode systems described for overall water splitting are presented to facilitate comparison.

Table 4. Performance of different amorphous electrocatalysts in overall water splitting process.

Catalyst (Support)	Performance at 10 mA cm^{-2} (V)	Performance high-j point (V)	Stability	Referenence
Co-Ni-P (Ni foam)	1.64	—	10 h @10 mA cm^{-2}	[220]
Ni-Cu-P (Ni foam)	1.64	—	50 h @10 mA cm^{-2} + 5000 cycle	[223]
CoB (Ni foam)	1.69	—	36 h @20 mA cm^{-2}	[225]
Ni_3P/Ni_3B/B-C (Ni foam)	1.50 @20 mA cm^{-2}	1.59 @50 mA cm^{-2}	50 h @50 mA cm^{-2}	[226]
Co-Ni-S (Carbon cloth)	1.60	—	35000 s @10 mA cm^{-2}	[184]
N-CoS/Cu_2S (Cu foam)	1.53	—	24 h @20 mA cm^{-2}	[229]
CoFeO@BP (Glassy carbon)	1.58	—	24 h @10 mA cm^{-2}	[231]

CoO_x/CN_x (Carbon sheet)	1.93	—	12 h @10 mA cm^{-2}	202
CoCuMoNi	1.56	—	24 h @ 20 mA cm^{-2} 24 h @ 200 mA cm^{-2} 24 h @ 400 mA cm^{-2}	233
Co@NC-NPs (Ni foam)	1.60	—	120 h @10 mA cm^{-2}	157
Ru/Cu-doped RuO_2	1.47	1.67 @100 mA cm^{-2}	40000 s @10 mA cm^{-2}	235

1.7 Summary and outlook

Across the literature surveyed in this review, amorphous structures often emerge as a practical lever for improving electrochemical water splitting. Across many composition families, the absence of long-range order correlates with features that matter at the electrode: dense populations of under-coordinated sites, flexible local bonding that moderates adsorption energetics, and short transport length scales, when implemented as thin layers or hybrids on conductive backbone. When these disordered phases are implemented as thin films, nanosheets, or nanoparticle carpets directly on conductive scaffolds, they also minimize interfacial resistance and, when paired with favorable surface chemistry and multiscale rough/porous architectures, can improve electrolyte wetting and gas-bubble removal at practically relevant current densities, and maintain performance at practically relevant current densities. Taken together, these attributes translate, on average, into lower overpotentials, more favorable Tafel behavior, and durable operation for both HER and OER relative to crystalline counterparts prepared from similar chemistries.

Moreover, durability should not be conflated with structural invariance. OER/HER catalysts, amorphous included, operate through dynamic reconstruction and/or dissolution-redeposition processes, meaning that performance retention can reflect establishment of a steady-state active surface rather than persistence of the as-prepared phase. Future studies and fair comparisons will therefore benefit from explicitly reporting both electrochemical durability metrics and evidence for (or against) structural/compositional evolution (post-mortem and operando), particularly when amorphous materials are used as precatalysts that readily evolve under bias.

At the same time, amorphization is not a single design trick but a platform that couples naturally with other levers. Compositional freedom (multi-metal and multi-anion chemistries) allows tuning of the local electronic structure beyond the constraints of a rigid lattice; texturing and porosity provide additional mass-transport advantages; and binder free integration with foams, meshes, or carbon textiles reduces ohmic and contact losses. A recurring theme is that improvements persist after intrinsic normalization, indicating that the gains are not merely geometric but are rooted in the short-range order and defect chemistry of the amorphous state. These trends appear robust across alkaline, neutral, and acidic environments and extend to more challenging media such as alkaline seawater.

Looking forward, several priorities can accelerate the maturation of amorphous electrocatalysts from promising materials to deployable technologies. First, structure property mapping needs to move beyond “amorphous vs crystalline” labels toward quantitative descriptors of disorder and local coordination, ideally supported by operando spectroscopy to connect changing coordination

environments with kinetic signatures. Second, synthetic control over thickness, defect density, and heteroatom content will be crucial: scalable routes (electrodeposition, chemical bath/sol–gel, low-temperature phosphidation/sulfidation, sputtering) already exist, but tighter control of film continuity, adhesion, and porosity will improve reproducibility and device integration. Third, compositionally complex designs remain underexplored; high-entropy amorphous networks and multi-anion frameworks offer vast, still sparsely sampled spaces for optimizing binding energies and conductivity while maintaining corrosion tolerance. Finally, device-level validation, integration into membrane-electrode assemblies, assessment under differential pressure, and impurity tolerance will provide the most meaningful proof of value.

In summary, amorphous structural design offers a coherent, generalizable strategy to unlock high activity and stability in water splitting by uniting abundant accessible sites, tunable local chemistry, favorable interfacial physics, and scalable electrode architectures. With rigorous benchmarking, deeper structural quantification, and continued advances in synthesis and device integration, disordered catalysts are well positioned to move from compelling laboratory demonstrations toward the performance, durability, and manufacturability required for practical hydrogen technologies.

References

(1) Islam, S.; Weerasinghe, H.; Prado, D. M.; Gonzaga, A. N.; Burda, C. Diversifying the Materials and Technologies for the Future of Energy Storage. *Energy & Fuels* **2025**, *39* (18), 8369–8390. https://doi.org/10.1021/acs.energyfuels.5c00468.

(2) Maghool, S.; Asgharinezhad, A. A.; Larimi, A.; Ghotbi, C.; Khorasheh, F. Enhanced Oxygen Evolution Reaction Performance Using Amorphous Hollow Cerium-Doped Cobalt Phosphate Derived from ZIF-67 Structures. *J. Alloys Compd.* **2024**, *1008*, 176697. https://doi.org/10.1016/j.jallcom.2024.176697.

(3) Gan, J.-C.; Jiang, Z.-F.; Fang, K.-M.; Li, X.-S.; Zhang, L.; Feng, J.-J.; Wang, A.-J. Low Rh Doping Accelerated HER/OER Bifunctional Catalytic Activities of Nanoflower-like Ni-Co Sulfide for Greatly Boosting Overall Water Splitting. *J. Colloid Interface Sci.* **2025**, *677*, 221–231. https://doi.org/10.1016/j.jcis.2024.08.050.

(4) Molaei, Z.; Asgharinezhad, A. A.; Larimi, A.; Ghotbi, C.; Khorasheh, F. Incorporation of CeO 2 Nanosheets into MnCoSx Hollow Nanorods for Next Generation Supercapacitors. *Energy & Fuels* **2025**. https://doi.org/10.1021/acs.energyfuels.4c05048.

(5) Panwar, N. L.; Kaushik, S. C.; Kothari, S. Role of Renewable Energy Sources in Environmental Protection: A Review. *Renew. Sustain. Energy Rev.* **2011**, *15* (3), 1513–1524. https://doi.org/10.1016/j.rser.2010.11.037.

(6) Usman, M. R. Hydrogen Storage Methods: Review and Current Status. *Renew. Sustain. Energy Rev.* **2022**, *167*, 112743. https://doi.org/10.1016/j.rser.2022.112743.

(7) Javaid, R. Catalytic Hydrogen Production, Storage and Application. *Catalysts* **2021**, *11* (7), 836. https://doi.org/10.3390/catal11070836.

(8) Pan, A.; Liu, J.; Liu, Z.; Yang, Y.; Yang, X.; Zhang, M. Application of Hydrogen Energy and Review of Current Conditions. *IOP Conf. Ser. Earth Environ. Sci.* **2020**, *526* (1), 012124. https://doi.org/10.1088/1755-1315/526/1/012124.

(9) SIMPSON, A.; LUTZ, A. Exergy Analysis of Hydrogen Production via Steam Methane

Reforming. *Int. J. Hydrogen Energy* **2007**, *32* (18), 4811–4820. https://doi.org/10.1016/j.ijhydene.2007.08.025.

(10) Gong, Y.; Yao, J.; Wang, P.; Li, Z.; Zhou, H.; Xu, C. Perspective of Hydrogen Energy and Recent Progress in Electrocatalytic Water Splitting. *Chinese J. Chem. Eng.* **2022**, *43*, 282–296. https://doi.org/10.1016/j.cjche.2022.02.010.

(11) Sharma, S.; Agarwal, S.; Jain, A. Significance of Hydrogen as Economic and Environmentally Friendly Fuel. *Energies* **2021**, *14* (21), 7389. https://doi.org/10.3390/en14217389.

(12) Li, X.; Zhao, L.; Yu, J.; Liu, X.; Zhang, X.; Liu, H.; Zhou, W. Water Splitting: From Electrode to Green Energy System. *Nano-Micro Lett.* **2020**, *12* (1), 131. https://doi.org/10.1007/s40820-020-00469-3.

(13) Asgharinezhad, A. A.; Bahmani, A.; Larimi, A.; Khorasheh, F.; Ghotbi, C. Trimetallic (Cobalt-Nickel-Copper) Phosphates with Cake Ball-Like Morphology for Highly Efficient Oxygen Evolution Reaction. *J. Alloys Compd.* **2025**, *1024*, 180102. https://doi.org/10.1016/j.jallcom.2025.180102.

(14) Sun, H.; Xu, X.; Kim, H.; Jung, W.; Zhou, W.; Shao, Z. Electrochemical Water Splitting: Bridging the Gaps Between Fundamental Research and Industrial Applications. *ENERGY Environ. Mater.* **2023**, *6* (5). https://doi.org/10.1002/eem2.12441.

(15) Hemmerling, J. R.; Mathur, A.; Linic, S. Design Principles for Efficient and Stable Water Splitting Photoelectrocatalysts. *Acc. Chem. Res.* **2021**, *54* (8), 1992–2002. https://doi.org/10.1021/acs.accounts.1c00072.

(16) Li, S.; Liu, Y.; Feng, K.; Li, C.; Xu, J.; Lu, C.; Lin, H.; Feng, Y.; Ma, D.; Zhong, J. High Valence State Sites as Favorable Reductive Centers for High-Current-Density Water Splitting. *Angew. Chemie* **2023**, *135* (39). https://doi.org/10.1002/ange.202308670.

(17) Li, J.; Hu, J.; Zhang, M.; Gou, W.; Zhang, S.; Chen, Z.; Qu, Y.; Ma, Y. A Fundamental Viewpoint on the Hydrogen Spillover Phenomenon of Electrocatalytic Hydrogen Evolution. *Nat. Commun.* **2021**, *12* (1), 3502. https://doi.org/10.1038/s41467-021-23750-4.

(18) Bairami, Z.; Asgharinezhad, A. A.; Courtney, J. M.; Larimi, A.; Khorasheh, F. A Novel CoCuNi-Sulfide Nanocatalyst Derived from Trimetallic Zeolitic Imidazolate Framework for Boosting Oxygen Evolution Reaction Performance: Comparison Study of Sulfides and Oxides. *Mater. Today Chem.* **2024**, *42*, 102398. https://doi.org/10.1016/j.mtchem.2024.102398.

(19) Liu, J.; Nai, J.; You, T.; An, P.; Zhang, J.; Ma, G.; Niu, X.; Liang, C.; Yang, S.; Guo, L. The Flexibility of an Amorphous Cobalt Hydroxide Nanomaterial Promotes the Electrocatalysis of Oxygen Evolution Reaction. *Small* **2018**, *14* (17). https://doi.org/10.1002/smll.201703514.

(20) Wang, X.; Tian, H.; Yu, X.; Chen, L.; Cui, X.; Shi, J. Advances and Insights in Amorphous Electrocatalyst towards Water Splitting. *Chinese J. Catal.* **2023**, *51*, 5–48. https://doi.org/10.1016/S1872-2067(23)64486-9.

(21) Chen, J.; Wang, X.; Sun, C.; Li, Z.; Zhou, Y.; Li, Z.; Qian, Y.; Wang, M.; Li, S.; Lai, Y.; Wang, S. Surface Amorphization Enables Robust Catalyst for Industrial-Level Low-

Potential Electrooxidation Reactions. *Nat. Commun.* **2025**, *16* (1), 6932. https://doi.org/10.1038/s41467-025-62293-w.

(22) Wang, J.; Han, L.; Huang, B.; Shao, Q.; Xin, H. L.; Huang, X. Amorphization Activated Ruthenium-Tellurium Nanorods for Efficient Water Splitting. *Nat. Commun.* **2019**, *10* (1), 5692. https://doi.org/10.1038/s41467-019-13519-1.

(23) Ye, L.; Wang, J.; Zhang, Y.; Zhang, M.; Jing, X.; Gong, Y. A Self-Supporting Electrode with in-Situ Partial Transformation of Fe-MOF into Amorphous NiFe-LDH for Efficient Oxygen Evolution Reaction. *Appl. Surf. Sci.* **2021**, *556*, 149781. https://doi.org/10.1016/j.apsusc.2021.149781.

(24) Liang, J.; Cai, Z.; Li, Z.; Yao, Y.; Luo, Y.; Sun, S.; Zheng, D.; Liu, Q.; Sun, X.; Tang, B. Efficient Bubble/Precipitate Traffic Enables Stable Seawater Reduction Electrocatalysis at Industrial-Level Current Densities. *Nat. Commun.* **2024**, *15* (1), 2950. https://doi.org/10.1038/s41467-024-47121-x.

(25) Zhao, H.-F.; Li, L.; Zhang, T.; Yao, J.-Q.; Peng, X.; Peng, J.; Zhu, M.; Xu, B.-B.; Liu, X.-W.; Yu, H.-B. Discovering High-Entropy Electrocatalysts through a Batch-Alloy Targeting Approach. *Sci. Adv.* **2025**, *11* (28). https://doi.org/10.1126/sciadv.adx6121.

(26) Wu, G.; Han, X.; Hong, X. Short-to-Medium-Range Order in Amorphous Nanocatalysts. *Mater. Today Catal.* **2023**, *3*, 100025. https://doi.org/https://doi.org/10.1016/j.mtcata.2023.100025.

(27) Zhang, Y.; Gao, F.; Wang, D.; Li, Z.; Wang, X.; Wang, C.; Zhang, K.; Du, Y. Amorphous/Crystalline Heterostructure Transition-Metal-Based Catalysts for High-Performance Water Splitting. *Coord. Chem. Rev.* **2023**, *475*, 214916. https://doi.org/https://doi.org/10.1016/j.ccr.2022.214916.

(28) Kong, Z.; Li, J.; Guo, D. Engineering Crystalline–Amorphous Interfaces in Nickel Oxide/Porous Carbon Hybrids for Enhanced Electrocatalytic Water Splitting. *New J. Chem.* **2025**, *49* (28), 12271–12278. https://doi.org/10.1039/D5NJ01646K.

(29) Park, J.; Lee, S.; Kim, S. Recent Advances in Amorphous Electrocatalysts for Oxygen Evolution Reaction. *Front. Chem.* **2022**, *10*. https://doi.org/10.3389/fchem.2022.1030803.

(30) Singh, M.; Cha, D. C.; Singh, T. I.; Maibam, A.; Paudel, D. R.; Nam, D. H.; Kim, T. H.; Yoo, S.; Lee, S. A Critical Review on Amorphous–Crystalline Heterostructured Electrocatalysts for Efficient Water Splitting. *Mater. Chem. Front.* **2023**, *7* (24), 6254–6280. https://doi.org/10.1039/D3QM00940H.

(31) Fan, X.; Yin, K.; Wang, H.; Zheng, J.; Lin, J.; Jia, B.; Xu, M.; Ye, L. The Advances in Innovative Amorphous Noble-Metal-Based Electrocatalysts. *Chem Catal.* **2025**, *5* (5), 101324. https://doi.org/10.1016/j.checat.2025.101324.

(32) Wang, G.; Chen, Z.; Zhu, J.; Xie, J.; Wei, W.; Yan, Y.-M.; Ni, B.-J. High-Entropy Amorphous Catalysts for Water Electrolysis: A New Frontier. *Nano-Micro Lett.* **2025**, *18* (1), 77. https://doi.org/10.1007/s40820-025-01936-5.

(33) Yu, Z.; Sun, Q.; Zhang, L.; Yang, H.; Chen, Y.; Guo, J.; Zhang, M.; Zhang, Z.; Jiang, Y. Research Progress of Amorphous Catalysts in the Field of Electrocatalysis. *Microstructures* **2024**, *4* (2). https://doi.org/10.20517/microstructures.2023.66.

(34) Pawar, S. M.; Pawar, B. S.; Hou, B.; Kim, J.; Aqueel Ahmed, A. T.; Chavan, H. S.; Jo, Y.; Cho, S.; Inamdar, A. I.; Gunjakar, J. L.; Kim, H.; Cha, S.; Im, H. Self-Assembled Two-Dimensional Copper Oxide Nanosheet Bundles as an Efficient Oxygen Evolution Reaction (OER) Electrocatalyst for Water Splitting Applications. *J. Mater. Chem. A* **2017**, *5* (25), 12747–12751. https://doi.org/10.1039/C7TA02835K.

(35) Zou, X.; Zhang, Y. Noble Metal-Free Hydrogen Evolution Catalysts for Water Splitting. *Chem. Soc. Rev.* **2015**, *44* (15), 5148–5180. https://doi.org/10.1039/C4CS00448E.

(36) Yan, Y.; Xia, B. Y.; Zhao, B.; Wang, X. A Review on Noble-Metal-Free Bifunctional Heterogeneous Catalysts for Overall Electrochemical Water Splitting. *J. Mater. Chem. A* **2016**, *4* (45), 17587–17603. https://doi.org/10.1039/C6TA08075H.

(37) Araújo, H. F.; Gómez, J. A.; Santos, D. M. F. Proton-Exchange Membrane Electrolysis for Green Hydrogen Production: Fundamentals, Cost Breakdown, and Strategies to Minimize Platinum-Group Metal Content in Hydrogen Evolution Reaction Electrocatalysts. *Catalysts* **2024**, *14* (12), 845. https://doi.org/10.3390/catal14120845.

(38) Jadhav, H. S.; Bandal, H. A.; Ramakrishna, S.; Kim, H. Critical Review, Recent Updates on Zeolitic Imidazolate Framework-67 (ZIF-67) and Its Derivatives for Electrochemical Water Splitting. *Adv. Mater.* **2022**, *34* (11). https://doi.org/10.1002/adma.202107072.

(39) You, B.; Sun, Y. Innovative Strategies for Electrocatalytic Water Splitting. *Acc. Chem. Res.* **2018**, *51* (7), 1571–1580. https://doi.org/10.1021/acs.accounts.8b00002.

(40) Browne, M. P.; Sofer, Z.; Pumera, M. Layered and Two Dimensional Metal Oxides for Electrochemical Energy Conversion. *Energy Environ. Sci.* **2019**, *12* (1), 41–58. https://doi.org/10.1039/C8EE02495B.

(41) Yu, J.; He, Q.; Yang, G.; Zhou, W.; Shao, Z.; Ni, M. Recent Advances and Prospective in Ruthenium-Based Materials for Electrochemical Water Splitting. *ACS Catal.* **2019**, *9* (11), 9973–10011. https://doi.org/10.1021/acscatal.9b02457.

(42) Nørskov, J. K.; Bligaard, T.; Logadottir, A.; Kitchin, J. R.; Chen, J. G.; Pandelov, S.; Stimming, U. Trends in the Exchange Current for Hydrogen Evolution. *J. Electrochem. Soc.* **2005**, *152* (3), J23. https://doi.org/10.1149/1.1856988.

(43) Liu, P. F.; Yin, H.; Fu, H. Q.; Zu, M. Y.; Yang, H. G.; Zhao, H. Activation Strategies of Water-Splitting Electrocatalysts. *J. Mater. Chem. A* **2020**, *8* (20), 10096–10129. https://doi.org/10.1039/D0TA01680B.

(44) Yuan, L.; Liu, S.; Xu, S.; Yang, X.; Bian, J.; Lv, C.; Yu, Z.; He, T.; Huang, Z.; Boukhvalov, D. W.; Cheng, C.; Huang, Y.; Zhang, C. Modulation of Volmer Step for Efficient Alkaline Water Splitting Implemented by Titanium Oxide Promoting Surface Reconstruction of Cobalt Carbonate Hydroxide. *Nano Energy* **2021**, *82*, 105732. https://doi.org/10.1016/j.nanoen.2020.105732.

(45) Yan, Y.; Xia, B.; Xu, Z.; Wang, X. Recent Development of Molybdenum Sulfides as Advanced Electrocatalysts for Hydrogen Evolution Reaction. *ACS Catal.* **2014**, *4* (6), 1693–1705. https://doi.org/10.1021/cs500070x.

(46) Xiao, Z.; Qian, Y.; Tan, T.; Lu, H.; Liu, C.; Wang, B.; Zhang, Q.; Sarwar, M. T.; Gao, R.; Tang, A.; Yang, H. Energy-Saving Hydrogen Production by Water Splitting Coupling Urea

Decomposition and Oxidation Reactions. *J. Mater. Chem. A* **2023**, *11* (1), 259–267. https://doi.org/10.1039/D2TA07152E.

(47) Peng, Z.; Jia, D.; Al-Enizi, A. M.; Elzatahry, A. A.; Zheng, G. From Water Oxidation to Reduction: Homologous Ni–Co Based Nanowires as Complementary Water Splitting Electrocatalysts. *Adv. Energy Mater.* **2015**, *5* (9). https://doi.org/10.1002/aenm.201402031.

(48) Singha Roy, S.; Madhu, R.; Karmakar, A.; Kundu, S. From Theory to Practice: A Critical and Comparative Assessment of Tafel Slope Analysis Techniques in Electrocatalytic Water Splitting. *ACS Mater. Lett.* **2024**, *6* (7), 3112–3123. https://doi.org/10.1021/acsmaterialslett.4c00831.

(49) Abdelwahab, M. A.; Mohamed, G. G.; Zayed, M. A.; Eliwa, A. S. Synthesis and Characterization of Cobalt–Organic Framework as an Electrocatalyst for Water Splitting Application. *Appl. Organomet. Chem.* **2025**, *39* (3). https://doi.org/10.1002/aoc.7889.

(50) Lee, S.; Lee, S.; Kim, C.; Han, Y.-K. Origin of Hydrogen Adsorption Free Energy Variation in Electrochemical Hydrogen Evolution in Transition-Metal Dichalcogenides. *Mater. Today Energy* **2024**, *43*, 101581. https://doi.org/10.1016/j.mtener.2024.101581.

(51) Exner, K. S. Does a Thermoneutral Electrocatalyst Correspond to the Apex of a Volcano Plot for a Simple Two-Electron Process? *Angew. Chemie* **2020**, *132* (26), 10320–10324. https://doi.org/10.1002/ange.202003688.

(52) Zhu, Y.-P.; Xu, X.; Su, H.; Liu, Y.-P.; Chen, T.; Yuan, Z.-Y. Ultrafine Metal Phosphide Nanocrystals in Situ Decorated on Highly Porous Heteroatom-Doped Carbons for Active Electrocatalytic Hydrogen Evolution. *ACS Appl. Mater. Interfaces* **2015**, *7* (51), 28369–28376. https://doi.org/10.1021/acsami.5b09092.

(53) Wei, J.; Zhou, M.; Long, A.; Xue, Y.; Liao, H.; Wei, C.; Xu, Z. J. Heterostructured Electrocatalysts for Hydrogen Evolution Reaction Under Alkaline Conditions. *Nano-Micro Lett.* **2018**, *10* (4), 75. https://doi.org/10.1007/s40820-018-0229-x.

(54) Liu, R.; Fei, H.-L.; Ye, G.-L. Recent Advances in Single Metal Atom-Doped MoS2 as Catalysts for Hydrogen Evolution Reaction. *Tungsten* **2020**, *2* (2), 147–161. https://doi.org/10.1007/s42864-020-00045-7.

(55) Duan, Y.; Dubouis, N.; Huang, J.; Dalla Corte, D. A.; Pimenta, V.; Xu, Z. J.; Grimaud, A. Revealing the Impact of Electrolyte Composition for Co-Based Water Oxidation Catalysts by the Study of Reaction Kinetics Parameters. *ACS Catal.* **2020**, *10* (7), 4160–4170. https://doi.org/10.1021/acscatal.0c00490.

(56) Exner, K. S. Four Generations of Volcano Plots for the Oxygen Evolution Reaction: Beyond Proton-Coupled Electron Transfer Steps? *Acc. Chem. Res.* **2024**, *57* (9), 1336–1345. https://doi.org/10.1021/acs.accounts.4c00048.

(57) Zhang, K.; Zou, R. Advanced Transition Metal-Based OER Electrocatalysts: Current Status, Opportunities, and Challenges. *Small* **2021**, *17* (37). https://doi.org/10.1002/smll.202100129.

(58) Liang, Q.; Brocks, G.; Bieberle-Hütter, A. Oxygen Evolution Reaction (OER) Mechanism under Alkaline and Acidic Conditions. *J. Phys. Energy* **2021**, *3* (2), 026001. https://doi.org/10.1088/2515-7655/abdc85.

(59) Christensen, R.; Hansen, H. A.; Dickens, C. F.; Nørskov, J. K.; Vegge, T. Functional Independent Scaling Relation for ORR/OER Catalysts. *J. Phys. Chem. C* **2016**, *120* (43), 24910–24916. https://doi.org/10.1021/acs.jpcc.6b09141.

(60) Lei, Z.; Wang, T.; Zhao, B.; Cai, W.; Liu, Y.; Jiao, S.; Li, Q.; Cao, R.; Liu, M. Recent Progress in Electrocatalysts for Acidic Water Oxidation. *Adv. Energy Mater.* **2020**, *10* (23). https://doi.org/10.1002/aenm.202000478.

(61) Park, J.; Kang, S.; Lee, J. Non-Noble Electrocatalysts Discovered by Scaling Relations of Gibbs-Free Energies of Key Oxygen Adsorbates in Water Oxidation. *J. Mater. Chem. A* **2022**, *10* (30), 15975–15980. https://doi.org/10.1039/D2TA02594A.

(62) Exner, K. S. Overpotential-Dependent Volcano Plots to Assess Activity Trends in the Competing Chlorine and Oxygen Evolution Reactions. *ChemElectroChem* **2020**, *7* (6), 1448–1455. https://doi.org/10.1002/celc.202000120.

(63) Exner, K. S. Importance of the Walden Inversion for the Activity Volcano Plot of Oxygen Evolution. *Adv. Sci.* **2023**, *10* (36). https://doi.org/10.1002/advs.202305505.

(64) Gyanprakash D, M. Investigation of the Shift in Volcano Peak for the Oxygen Evolution Reaction at a High Reaction Rate. *J. Phys. Chem. C* **2023**, *127* (44), 21526–21533. https://doi.org/10.1021/acs.jpcc.3c03472.

(65) Exner, K. S. On the Mechanistic Complexity of Oxygen Evolution: Potential-Dependent Switching of the Mechanism at the Volcano Apex. *Mater. Horizons* **2023**, *10* (6), 2086–2095. https://doi.org/10.1039/D3MH00047H.

(66) Ying, J.; Chen, J.-B.; Xiao, Y.-X.; Cordoba de Torresi, S. I.; Ozoemena, K. I.; Yang, X.-Y. Recent Advances in Ru-Based Electrocatalysts for Oxygen Evolution Reaction. *J. Mater. Chem. A* **2023**, *11* (4), 1634–1650. https://doi.org/10.1039/D2TA07196G.

(67) Chen, S.; Wang, Y.; Wang, Z.; Zhang, K. Advances in Nonprecious Metal Catalysts for Efficient Water Oxidation in Alkaline Media. *Ionics (Kiel).* **2023**, *29* (1), 9–32. https://doi.org/10.1007/s11581-022-04774-2.

(68) Liu, K.; Cao, P.; Chen, W.; Ezeh, C. I.; Chen, Z.; Luo, Y.; Liu, Q.; Zhao, H.; Rui, Z.; Gao, S.; Yin, Z.; Sun, X.; Yu, X. Electrocatalysis Enabled Transformation of Earth-Abundant Water, Nitrogen and Carbon Dioxide for a Sustainable Future. *Mater. Adv.* **2022**, *3* (3), 1359–1400. https://doi.org/10.1039/D1MA00814E.

(69) Man, I. C.; Su, H.-Y.; Calle-Vallejo, F.; Hansen, H. A.; Martínez, J. I.; Inoglu, N. G.; Kitchin, J.; Jaramillo, T. F.; Nørskov, J. K.; Rossmeisl, J. Universality in Oxygen Evolution Electrocatalysis on Oxide Surfaces. *ChemCatChem* **2011**, *3* (7), 1159–1165. https://doi.org/https://doi.org/10.1002/cctc.201000397.

(70) Zou, Y.; Jing, L.; Zhang, J.; Luo, S.; Wang, L.; Li, Y.; Goei, R.; Tan, K. W.; Yoong Tok, A. I. ALD-Made Noble Metal High Entropy Alloy Nanofilm with Sub-Surface Amorphization for Enhanced Hydrogen Evolution. *J. Mater. Chem. A* **2024**, *12* (10), 5668–5678. https://doi.org/10.1039/D3TA05908A.

(71) Liang, C.; Rao, R. R.; Svane, K. L.; Hadden, J. H. L.; Moss, B.; Scott, S. B.; Sachs, M.; Murawski, J.; Frandsen, A. M.; Riley, D. J.; Ryan, M. P.; Rossmeisl, J.; Durrant, J. R.; Stephens, I. E. L. Unravelling the Effects of Active Site Density and Energetics on the Water

Oxidation Activity of Iridium Oxides. *Nat. Catal.* **2024**, *7* (7), 763–775. https://doi.org/10.1038/s41929-024-01168-7.

(72) Fu, Q.; Wong, L. W.; Zheng, F.; Zheng, X.; Tsang, C. S.; Lai, K. H.; Shen, W.; Ly, T. H.; Deng, Q.; Zhao, J. Unraveling and Leveraging in Situ Surface Amorphization for Enhanced Hydrogen Evolution Reaction in Alkaline Media. *Nat. Commun.* **2023**, *14* (1), 6462. https://doi.org/10.1038/s41467-023-42221-6.

(73) Shinde, N.; Shinde, P.; Xia, Q. X.; Yun, J. M.; Mane, R.; Kim, K. H. Electrocatalytic Water Splitting through the Ni x S y Self-Grown Superstructures Obtained via a Wet Chemical Sulfurization Process. *ACS Omega* **2019**, *4* (4), 6486–6491. https://doi.org/10.1021/acsomega.9b00132.

(74) Zeng, K.; Zhang, D. Recent Progress in Alkaline Water Electrolysis for Hydrogen Production and Applications. *Prog. Energy Combust. Sci.* **2010**, *36* (3), 307–326. https://doi.org/10.1016/j.pecs.2009.11.002.

(75) Shi, Y.; Zhang, B. Recent Advances in Transition Metal Phosphide Nanomaterials: Synthesis and Applications in Hydrogen Evolution Reaction. *Chem. Soc. Rev.* **2016**, *45* (6), 1529–1541. https://doi.org/10.1039/C5CS00434A.

(76) Song, Y.; Xu, B.; Liao, T.; Guo, J.; Wu, Y.; Sun, Z. Electronic Structure Tuning of 2D Metal (Hydr)Oxides Nanosheets for Electrocatalysis. *Small* **2021**, *17* (9). https://doi.org/10.1002/smll.202002240.

(77) Nicholson, R. S.; Shain, I. Theory of Stationary Electrode Polarography for a Chemical Reaction Coupled between Two Charge Transfers. *Anal. Chem.* **1965**, *37* (2), 178–190. https://doi.org/10.1021/ac60221a002.

(78) Anantharaj, S.; Noda, S. How Properly Are We Interpreting the Tafel Lines in Energy Conversion Electrocatalysis? *Mater. Today Energy* **2022**, *29*, 101123. https://doi.org/10.1016/j.mtener.2022.101123.

(79) Murthy, A. P.; Theerthagiri, J.; Madhavan, J. Insights on Tafel Constant in the Analysis of Hydrogen Evolution Reaction. *J. Phys. Chem. C* **2018**, *122* (42), 23943–23949. https://doi.org/10.1021/acs.jpcc.8b07763.

(80) Lyu, F.; Wang, Q.; Choi, S. M.; Yin, Y. Noble-Metal-Free Electrocatalysts for Oxygen Evolution. *Small* **2019**, *15* (1). https://doi.org/10.1002/smll.201804201.

(81) Karmakar, A.; Nagappan, S.; Das, A.; Kalloorkal, A.; Kundu, S. Exploring the Linear Relationship between Potential Dynamics and Interfacial Capacitance: Implications for Enhancing the Turnover Frequency in Electrochemical Water Splitting. *J. Mater. Chem. A* **2023**, *11* (29), 15635–15642. https://doi.org/10.1039/D3TA02540C.

(82) Xiong, B.; Chen, L.; Shi, J. Anion-Containing Noble-Metal-Free Bifunctional Electrocatalysts for Overall Water Splitting. *ACS Catal.* **2018**, *8* (4), 3688–3707. https://doi.org/10.1021/acscatal.7b04286.

(83) Anantharaj, S.; Karthik, P. E.; Noda, S. The Significance of Properly Reporting Turnover Frequency in Electrocatalysis Research. *Angew. Chemie Int. Ed.* **2021**, *60* (43), 23051–23067. https://doi.org/10.1002/anie.202110352.

(84) Yoo, J.-S.; Park, S.-M. An Electrochemical Impedance Measurement Technique Employing

Fourier Transform. *Anal. Chem.* **2000**, *72* (9), 2035–2041. https://doi.org/10.1021/ac9907540.

(85) Anantharaj, S.; Noda, S. Appropriate Use of Electrochemical Impedance Spectroscopy in Water Splitting Electrocatalysis. *ChemElectroChem* **2020**, *7* (10), 2297–2308. https://doi.org/10.1002/celc.202000515.

(86) Bredar, A. R. C.; Chown, A. L.; Burton, A. R.; Farnum, B. H. Electrochemical Impedance Spectroscopy of Metal Oxide Electrodes for Energy Applications. *ACS Appl. Energy Mater.* **2020**, *3* (1), 66–98. https://doi.org/10.1021/acsaem.9b01965.

(87) Yin, J.; Jin, J.; Lu, M.; Huang, B.; Zhang, H.; Peng, Y.; Xi, P.; Yan, C.-H. Iridium Single Atoms Coupling with Oxygen Vacancies Boosts Oxygen Evolution Reaction in Acid Media. *J. Am. Chem. Soc.* **2020**, *142* (43), 18378–18386. https://doi.org/10.1021/jacs.0c05050.

(88) Li, D.; Liu, H.; Feng, L. A Review on Advanced FeNi-Based Catalysts for Water Splitting Reaction. *Energy & Fuels* **2020**, *34* (11), 13491–13522. https://doi.org/10.1021/acs.energyfuels.0c03084.

(89) Yousefi, Z.; Asgharinezhad, A. A.; Larimi, A.; Ghotbi, C. Highly Efficient Electrocatalytic Water Oxidation Based on Non-Precious Metal Oxides/Sulfides Derived from a FeCoNi-Metal Organic Framework. *J. Alloys Compd.* **2024**, *1002*, 175214. https://doi.org/10.1016/j.jallcom.2024.175214.

(90) Yin, J.; Jin, J.; Zhang, H.; Lu, M.; Peng, Y.; Huang, B.; Xi, P.; Yan, C. Atomic Arrangement in Metal-Doped NiS 2 Boosts the Hydrogen Evolution Reaction in Alkaline Media. *Angew. Chemie* **2019**, *131* (51), 18849–18855. https://doi.org/10.1002/ange.201911470.

(91) Salah, A.; Ren, H.-D.; Al-Ansi, N.; Yu, F.-Y.; Lang, Z.-L.; Tan, H.; Li, Y.-G. Ru/Mo 2 C@NC Schottky Junction-Loaded Hollow Nanospheres as an Efficient Hydrogen Evolution Electrocatalyst. *J. Mater. Chem. A* **2021**, *9* (36), 20518–20529. https://doi.org/10.1039/D1TA05876B.

(92) Yu, P.; Wang, F.; Shifa, T. A.; Zhan, X.; Lou, X.; Xia, F.; He, J. Earth Abundant Materials beyond Transition Metal Dichalcogenides: A Focus on Electrocatalyzing Hydrogen Evolution Reaction. *Nano Energy* **2019**, *58*, 244–276. https://doi.org/10.1016/j.nanoen.2019.01.017.

(93) Anantharaj, S.; Ede, S. R.; Sakthikumar, K.; Karthick, K.; Mishra, S.; Kundu, S. Recent Trends and Perspectives in Electrochemical Water Splitting with an Emphasis on Sulfide, Selenide, and Phosphide Catalysts of Fe, Co, and Ni: A Review. *ACS Catal.* **2016**, *6* (12), 8069–8097. https://doi.org/10.1021/acscatal.6b02479.

(94) Wacławek, S.; Padil, V. V. T.; Černík, M. Major Advances and Challenges in Heterogeneous Catalysis for Environmental Applications: A Review. *Ecol. Chem. Eng. S* **2018**, *25* (1), 9–34. https://doi.org/10.1515/eces-2018-0001.

(95) Chen, F.-Y.; Wu, Z.-Y.; Adler, Z.; Wang, H. Stability Challenges of Electrocatalytic Oxygen Evolution Reaction: From Mechanistic Understanding to Reactor Design. *Joule* **2021**, *5* (7), 1704–1731. https://doi.org/https://doi.org/10.1016/j.joule.2021.05.005.

(96) Gao, L.; Cui, X.; Sewell, C. D.; Li, J.; Lin, Z. Recent Advances in Activating Surface

Reconstruction for the High-Efficiency Oxygen Evolution Reaction. *Chem. Soc. Rev.* **2021**, *50* (15), 8428–8469. https://doi.org/10.1039/D0CS00962H.

(97) Li, H.; Lin, Y.; Duan, J.; Wen, Q.; Liu, Y.; Zhai, T. Stability of Electrocatalytic OER: From Principle to Application. *Chem. Soc. Rev.* **2024**, *53* (21), 10709–10740. https://doi.org/10.1039/D3CS00010A.

(98) Marquez, R. A.; Espinosa, M.; Kalokowski, E.; Son, Y. J.; Kawashima, K.; Le, T. V.; Chukwuneke, C. E.; Mullins, C. B. A Guide to Electrocatalyst Stability Using Lab-Scale Alkaline Water Electrolyzers. *ACS Energy Lett.* **2024**, *9* (2), 547–555. https://doi.org/10.1021/acsenergylett.3c02758.

(99) Li, J.; Gong, J. Operando Characterization Techniques for Electrocatalysis. *Energy Environ. Sci.* **2020**, *13* (11), 3748–3779. https://doi.org/10.1039/D0EE01706J.

(100) Cherevko, S. Stability and Dissolution of Electrocatalysts: Building the Bridge between Model and "Real World" Systems. *Curr. Opin. Electrochem.* **2018**, *8*, 118–125. https://doi.org/https://doi.org/10.1016/j.coelec.2018.03.034.

(101) Chen, C.; Wang, X.; Huang, Z.; Mo, J.; Zhang, X.; Peng, C.; Khairy, M.; Ge, J.; Long, Z. Engineering of Self-Supported Electrocatalysts on a Three-Dimensional Nickel Foam Platform for Efficient Water Electrolysis. *Trans. Tianjin Univ.* **2024**, *30* (2), 103–116. https://doi.org/10.1007/s12209-024-00389-y.

(102) Zhai, W.; Sakthivel, T.; Chen, F.; Du, C.; Yu, H.; Dai, Z. Amorphous Materials for Elementary-Gas-Involved Electrocatalysis: An Overview. *Nanoscale* **2021**, *13* (47), 19783–19811. https://doi.org/10.1039/D1NR06764H.

(103) Wang, H.; Qi, J.; Yang, N.; Cui, W.; Wang, J.; Li, Q.; Zhang, Q.; Yu, X.; Gu, L.; Li, J.; Yu, R.; Huang, K.; Song, S.; Feng, S.; Wang, D. Dual-Defects Adjusted Crystal-Field Splitting of LaCo 1− x Ni x O 3− δ Hollow Multishelled Structures for Efficient Oxygen Evolution. *Angew. Chemie Int. Ed.* **2020**, *59* (44), 19691–19695. https://doi.org/10.1002/anie.202007077.

(104) Zhang, D.; Soo, J. Z.; Tan, H. H.; Jagadish, C.; Catchpole, K.; Karuturi, S. K. Earth-Abundant Amorphous Electrocatalysts for Electrochemical Hydrogen Production: A Review. *Adv. Energy Sustain. Res.* **2021**, *2* (3). https://doi.org/10.1002/aesr.202000071.

(105) Koshy, S. S.; Rath, J.; Kiani, A. Fabrication of Binder-Less Metal Electrodes for Electrochemical Water Splitting – A Review. *Heliyon* **2024**, *10* (17), e37188. https://doi.org/https://doi.org/10.1016/j.heliyon.2024.e37188.

(106) Menezes, P. W.; Panda, C.; Walter, C.; Schwarze, M.; Driess, M. A Cobalt-Based Amorphous Bifunctional Electrocatalysts for Water-Splitting Evolved from a Single-Source Lazulite Cobalt Phosphate. *Adv. Funct. Mater.* **2019**, *29* (32). https://doi.org/10.1002/adfm.201808632.

(107) Liu, T.; Liu, Q.; Asiri, A. M.; Luo, Y.; Sun, X. An Amorphous CoSe Film Behaves as an Active and Stable Full Water-Splitting Electrocatalyst under Strongly Alkaline Conditions. *Chem. Commun.* **2015**, *51* (93), 16683–16686. https://doi.org/10.1039/C5CC06892D.

(108) Thangavel, P.; Kim, G.; Kim, K. S. Electrochemical Integration of Amorphous NiFe (Oxy)Hydroxides on Surface-Activated Carbon Fibers for High-Efficiency Oxygen

Evolution in Alkaline Anion Exchange Membrane Water Electrolysis. *J. Mater. Chem. A* **2021**, *9* (24), 14043–14051. https://doi.org/10.1039/D1TA02883A.

(109) Zhao, H.; Ma, K.; Gao, S.; Wang, B.; Wang, Y. Advances in Understanding and Manipulating Electrode Wettability for Electrocatalytic Performance Enhancement. *Mater. Today Catal.* **2025**, *9*, 100101. https://doi.org/https://doi.org/10.1016/j.mtcata.2025.100101.

(110) Ren, Q.; Tran, C.; Zhang, K.; Zhu, C.; Li, Y. Synergizing Superwetting and Architected Electrodes for High-Rate Water Splitting. *Nanoscale* **2025**, *17* (7), 3600–3615. https://doi.org/10.1039/D4NR03836C.

(111) Li, M.; Wei, J.; Ren, L.; Zhao, Y.; Shang, Z.; Zhou, D.; Liu, W.; Luo, L.; Sun, X. Superwetting Behaviors at the Interface between Electrode and Electrolyte. *Cell Reports Phys. Sci.* **2021**, *2* (3), 100374. https://doi.org/https://doi.org/10.1016/j.xcrp.2021.100374.

(112) Liu, G.; Wong, W. S. Y.; Kraft, M.; Ager, J. W.; Vollmer, D.; Xu, R. Wetting-Regulated Gas-Involving (Photo)Electrocatalysis: Biomimetics in Energy Conversion. *Chem. Soc. Rev.* **2021**, *50* (18), 10674–10699. https://doi.org/10.1039/D1CS00258A.

(113) Duan, Y.; Yu, Z.; Hu, S.; Zheng, X.; Zhang, C.; Ding, H.; Hu, B.; Fu, Q.; Yu, Z.; Zheng, X.; Zhu, J.; Gao, M.; Yu, S. Scaled-Up Synthesis of Amorphous NiFeMo Oxides and Their Rapid Surface Reconstruction for Superior Oxygen Evolution Catalysis. *Angew. Chemie Int. Ed.* **2019**, *58* (44), 15772–15777. https://doi.org/10.1002/anie.201909939.

(114) Anantharaj, S.; Noda, S. Amorphous Catalysts and Electrochemical Water Splitting: An Untold Story of Harmony. *Small* **2020**, *16* (2). https://doi.org/10.1002/smll.201905779.

(115) Chen, C.; Jin, H.; Wang, P.; Sun, X.; Jaroniec, M.; Zheng, Y.; Qiao, S.-Z. Local Reaction Environment in Electrocatalysis. *Chem. Soc. Rev.* **2024**, *53* (4), 2022–2055. https://doi.org/10.1039/D3CS00669G.

(116) Marshall, G. W.; Lewis, D. B.; Dodds, B. E. Electroless Deposition of Ni-P Alloys with and without the Use of Superimposed Pulsed Current. *Surf. Coatings Technol.* **1992**, *53* (3), 223–230. https://doi.org/10.1016/0257-8972(92)90380-S.

(117) Jo, W.; Jeong, D.; Jeong, J.; Kim, T.; Han, S.; Son, M.; Kim, Y.; Park, Y. H.; Jung, H. Electrocatalytic Properties of Pulse-Reverse Electrodeposited Nickel Phosphide for Hydrogen Evolution Reaction. *Front. Chem.* **2021**, *9*. https://doi.org/10.3389/fchem.2021.781838.

(118) Guo, K.; Kunimoto, M.; Homma, T. Electroless-Deposited NiFeP Catalyst-Coated-Membrane Cathodes for Anion Exchange Membrane Water Electrolysis. *J. Mater. Chem. A* **2025**, *13* (10), 7313–7323. https://doi.org/10.1039/D4TA06868H.

(119) Parakh, A.; Kiani, M. T.; Lindgren, E.; Colmenares, A.; Lee, A. C.; Suzuki, Y.; Gu, X. W. Synthesis of Multifunctional Amorphous Metallic Shell on Crystalline Metallic Nanoparticles. *RSC Adv.* **2023**, *13* (43), 30491–30498. https://doi.org/10.1039/D3RA06093D.

(120) Zechel, F.; Hutár, P.; Vretenár, V.; Végsö, K.; Šiffalovič, P.; Sýkora, M. Green Colloidal Synthesis of MoS 2 Nanoflakes. *Inorg. Chem.* **2023**, *62* (40), 16554–16563. https://doi.org/10.1021/acs.inorgchem.3c02420.

(121) Standish, T.; Chen, J.; Jacklin, R.; Jakupi, P.; Ramamurthy, S.; Zagidulin, D.; Keech, P.; Shoesmith, D. CORROSION OF COPPER-COATED STEEL HIGH LEVEL NUCLEAR WASTE CONTAINERS UNDER PERMANENT DISPOSAL CONDITIONS. *Electrochim. Acta* **2016**, *211*, 331–342. https://doi.org/10.1016/j.electacta.2016.05.135.

(122) Ma, S.; Liu, Z.-P. Machine Learning for Atomic Simulation and Activity Prediction in Heterogeneous Catalysis: Current Status and Future. *ACS Catal.* **2020**, *10* (22), 13213–13226. https://doi.org/10.1021/acscatal.0c03472.

(123) Reuter, K.; Frenkel, D.; Scheffler, M. The Steady State of Heterogeneous Catalysis, Studied by First-Principles Statistical Mechanics. *Phys. Rev. Lett.* **2004**, *93* (11), 116105. https://doi.org/10.1103/PhysRevLett.93.116105.

(124) Nkabinde, S. S.; Ndala, Z. B.; Shumbula, N. P.; Kolokoto, T.; Nchoe, O.; Ngubeni, G. N.; Mubiayi, K. P.; Moloto, N. Delineating the Role of Crystallinity in the Electrocatalytic Activity of Colloidally Synthesized MoP Nanocrystals. *New J. Chem.* **2020**, *44* (33), 14041–14049. https://doi.org/10.1039/D0NJ02800B.

(125) Amber, H.; Balčiūnaitė, A.; Sukackienė, Z.; Tamašauskaitė-Tamašiūnaitė, L.; Norkus, E. Electrolessly Deposited Cobalt–Phosphorus Coatings for Efficient Hydrogen and Oxygen Evolution Reactions. *Catalysts* **2024**, *15* (1), 8. https://doi.org/10.3390/catal15010008.

(126) Wang, R.; Li, Z.; Li, Z.; Wen, M.; Wang, G.; Xie, G.; Liu, X.; Jiang, L. Electroless Deposition Synthesis of Composite Catalysts Ni-Fe-P-WO3/NF with Superior Oxygen Evolution Performance. *Int. J. Hydrogen Energy* **2022**, *47* (68), 29305–29314. https://doi.org/10.1016/j.ijhydene.2022.06.266.

(127) Battiato, S.; Urso, M.; Cosentino, S.; Pellegrino, A. L.; Mirabella, S.; Terrasi, A. Optimization of Oxygen Evolution Reaction with Electroless Deposited Ni–P Catalytic Nanocoating. *Nanomaterials* **2021**, *11* (11), 3010. https://doi.org/10.3390/nano11113010.

(128) Moloudi, M.; Noori, A.; Rahmanifar, M. S.; El-Kady, M. F.; Mousali, E.; Mohamed, N. B.; Xia, X.; Zhang, Y.; Vinu, A.; Vincent, M.; Kowalski, D.; Kaner, R. B.; Mousavi, M. F. Nanostructured Amorphous Ni–Co–Fe Phosphide as a Versatile Electrocatalyst towards Seawater Splitting and Aqueous Zinc–Air Batteries. *Chem. Sci.* **2025**, *16* (21), 9484–9500. https://doi.org/10.1039/D5SC01249J.

(129) Kang, H.; Lee, T.; Park, Y.; Hong, Y.-K.; Choi, M.; Cho, J.; Ha, D.-H. Colloidal Synthetic Methods of Amorphous Molybdenum Phosphide Nanoparticles for Hydrogen Evolution Reaction Catalysts. *Korean J. Chem. Eng.* **2020**, *37* (8), 1419–1426. https://doi.org/10.1007/s11814-020-0576-4.

(130) Liu, X.; Yang, W.; Liu, Z.; Fan, H.; Zheng, W. In-Situ Synthesis of Coral-Like Molybdenum Phosphide (MoP) Microspheres for Lithium-Ion Battery. *Acta Metall. Sin. (English Lett.* **2021**, *34* (3), 401–409. https://doi.org/10.1007/s40195-020-01160-7.

(131) Wang, L.; Gu, C.; Ge, X.; Zhang, J.; Zhu, H.; Tu, J. Anchoring Ni 2 P Sheets on NiCo 2 O 4 Nanocone Arrays as Optimized Bifunctional Electrocatalyst for Water Splitting. *Adv. Mater. Interfaces* **2017**, *4* (20). https://doi.org/10.1002/admi.201700481.

(132) Ledendecker, M.; Krick Calderón, S.; Papp, C.; Steinrück, H.; Antonietti, M.; Shalom, M. The Synthesis of Nanostructured Ni 5 P 4 Films and Their Use as a Non-Noble Bifunctional Electrocatalyst for Full Water Splitting. *Angew. Chemie Int. Ed.* **2015**, *54* (42), 12361–

12365. https://doi.org/10.1002/anie.201502438.

(133) Dincă, M.; Surendranath, Y.; Nocera, D. G. Nickel-Borate Oxygen-Evolving Catalyst That Functions under Benign Conditions. *Proc. Natl. Acad. Sci.* **2010**, *107* (23), 10337–10341. https://doi.org/10.1073/pnas.1001859107.

(134) Li, L.; Deng, Z.; Yu, L.; Lin, Z.; Wang, W.; Yang, G. Amorphous Transitional Metal Borides as Substitutes for Pt Cocatalysts for Photocatalytic Water Splitting. *Nano Energy* **2016**, *27*, 103–113. https://doi.org/10.1016/j.nanoen.2016.06.054.

(135) Wang, N.; Xu, A.; Ou, P.; Hung, S.-F.; Ozden, A.; Lu, Y.-R.; Abed, J.; Wang, Z.; Yan, Y.; Sun, M.-J.; Xia, Y.; Han, M.; Han, J.; Yao, K.; Wu, F.-Y.; Chen, P.-H.; Vomiero, A.; Seifitokaldani, A.; Sun, X.; Sinton, D.; Liu, Y.; Sargent, E. H.; Liang, H. Boride-Derived Oxygen-Evolution Catalysts. *Nat. Commun.* **2021**, *12* (1), 6089. https://doi.org/10.1038/s41467-021-26307-7.

(136) Zhang, N.; Chai, Y. Lattice Oxygen Redox Chemistry in Solid-State Electrocatalysts for Water Oxidation. *Energy Environ. Sci.* **2021**, *14* (9), 4647–4671. https://doi.org/10.1039/D1EE01277K.

(137) Qiu, P.; Fang, Z.; Yuan, L.; Hou, J.; Zhu, J.; Ke, C.; Zhang, L.; Zhuang, X. Amorphous NiFeCo Oxyhydroxide as a High-Performance Electrocatalyst for Alkaline Oxygen Evolution Reaction. *ChemCatChem* **2025**, *17* (17). https://doi.org/10.1002/cctc.202500454.

(138) Li, Y.; Gao, Y.; Liu, M.; Wang, T.; Wang, X.; Hu, H. One-Step Hydrothermal Synthesis of Amorphous Nickel/Iron Oxide and Its Application as Catalyst for Efficient Oxygen Evolution Reaction. *Int. J. Electrochem. Sci.* **2022**, *17* (3), 220338. https://doi.org/10.20964/2022.03.29.

(139) Tao, J.; Liu, S.; Liao, Y.; Qiao, H.; Liao, G.; Zou, Z.; Lang, L.; Li, C.; Wang, Z.; Qi, X. Amorphous MoO2 with a Porous Nanostructure as a Highly Efficient Electrocatalyst for Overall Water Splitting. *Appl. Phys. A* **2022**, *128* (7), 618. https://doi.org/10.1007/s00339-022-05734-3.

(140) Bachvarov, V.; Lefterova, E.; Rashkov, R. Electrodeposited NiFeCo and NiFeCoP Alloy Cathodes for Hydrogen Evolution Reaction in Alkaline Medium. *Int. J. Hydrogen Energy* **2016**, *41* (30), 12762–12771. https://doi.org/10.1016/j.ijhydene.2016.05.164.

(141) Ding, J.; Fan, T.; Shen, K.; Li, Y. Electrochemical Synthesis of Amorphous Metal Hydroxide Microarrays with Rich Defects from MOFs for Efficient Electrocatalytic Water Oxidation. *Appl. Catal. B Environ.* **2021**, *292*, 120174. https://doi.org/10.1016/j.apcatb.2021.120174.

(142) Xia, C.; Li, F.-M.; He, C.; Zaman, S.; Guo, W.; Xia, B. Y. Structural Reconstruction of Electrocatalysts. *Fundam. Res.* **2024**. https://doi.org/10.1016/j.fmre.2024.04.017.

(143) Wang, K.; Xu, Y.; Daneshvariesfahlan, V.; Rafique, M.; Fu, Q.; Wei, H.; Zhang, Y.; Zhang, J.; Zhang, B.; Song, B. Insight into the Structural Reconstruction of Alkaline Water Oxidation Electrocatalysts. *Nanoscale* **2025**, *17* (11), 6287–6307. https://doi.org/10.1039/D4NR05426A.

(144) Yuan, H.; Zheng, J.; Lu, G.; Zhang, L.; Yan, T.; Luo, J.; Wang, Y.; Liu, Y.; Guo, T.; Wang, Z.; Nai, J.; Tao, X. Formation of 2D Amorphous Lithium Sulfide Enabled by Mo 2 C

Clusters Loaded Carbon Scaffold for High-Performance Lithium Sulfur Batteries. *Adv. Mater.* **2024**, *36* (28). https://doi.org/10.1002/adma.202400639.

(145) Liao, M.; Zhang, K.; Yan, W.; Yue, H.; Luo, C.; Wu, G.; Zeng, H. Constructing Amorphous/Crystalline Heterointerface in Cobalt Sulfide for High-Performance Supercapacitors. *J. Power Sources* **2025**, *625*, 235663. https://doi.org/10.1016/j.jpowsour.2024.235663.

(146) Jaramillo, T. F.; Jørgensen, K. P.; Bonde, J.; Nielsen, J. H.; Horch, S.; Chorkendorff, I. Identification of Active Edge Sites for Electrochemical H 2 Evolution from MoS 2 Nanocatalysts. *Science (80-.).* **2007**, *317* (5834), 100–102. https://doi.org/10.1126/science.1141483.

(147) Sygellou, L. Study of the Thermal Decomposition of Ammonium Tetrathiomolybdate, (NH4)2MoS4), in H2 and H2O Media by Quasi in-Situ Photoelectron Spectroscopy (XPS/UPS). *Appl. Surf. Sci.* **2025**, *682*, 161644. https://doi.org/10.1016/j.apsusc.2024.161644.

(148) Ma, B.; Zhang, Y.; He, C. Engineering Amorphous MoS2/RGO Hybrid Nanoflowers with Rich Edge Sites Boost Catalytic Hydrogen Generation. *J. Catal.* **2025**, *448*, 116178. https://doi.org/10.1016/j.jcat.2025.116178.

(149) Kornienko, N.; Resasco, J.; Becknell, N.; Jiang, C.-M.; Liu, Y.-S.; Nie, K.; Sun, X.; Guo, J.; Leone, S. R.; Yang, P. Operando Spectroscopic Analysis of an Amorphous Cobalt Sulfide Hydrogen Evolution Electrocatalyst. *J. Am. Chem. Soc.* **2015**, *137* (23), 7448–7455. https://doi.org/10.1021/jacs.5b03545.

(150) Chen, Y.; Wu, H.; Han, G.; Zhang, B.; Lu, X.; Yang, W.; Wang, G.; Han, X.; Zhou, X. Synergistic Effects Lead to High Thermoelectric Performance of Iodine Doped Pseudo-Binary Layered GeSb2Te4. *J. Mater.* **2025**, *11* (4), 100973. https://doi.org/10.1016/j.jmat.2024.100973.

(151) Tavanti, F.; Calzolari, A. Concurring Effect of Doping and Composition on the Thermodynamic Properties of Amorphous GexSe1-x Alloys. *Acta Mater.* **2024**, *266*, 119676. https://doi.org/10.1016/j.actamat.2024.119676.

(152) Li, Y.; Ding, R.; Guo, J.; Lu, Y.; Chen, Z.; Luo, J.; Gu, T.; Liu, Y. Exploring the Intrinsic Activity Enhancement and Charge Storage Mechanisms of O-doped Binary Ni/Co Perovskite Fluorides in Alkaline Electrolytes for Aqueous Supercapacitors. *Small* **2025**. https://doi.org/10.1002/smll.202508141.

(153) Butt, N.; Kubra, K. T.; Ali, G.; Butt, A.; Shahid, A.; Hayder, U.; Iqbal, F.; Salman, A. Electrochemical Study of Nanoneedle Arrays of Quaternary Metal (Ni-Co-Cu-Ce) -Based Oxides Composite Hybridized with Nitrogen-Doped Graphene Oxide and Polyaniline for Supercapacitor Applications. *J. Alloys Compd.* **2025**, *1013*, 178549. https://doi.org/10.1016/j.jallcom.2025.178549.

(154) Abbas, S.; Jarwal, B.; Ho, T.-T.; Meledath Valiyaveettil, S.; Hsing, C.-R.; Chou, T.-L.; Wei, C.-M.; Chen, L.-C.; Chen, K.-H. Synergistic Effect of Indium Doping on Thermoelectric Performance of Cubic GeTe-Based Thin Films. *Mater. Today Phys.* **2024**, *49*, 101581. https://doi.org/10.1016/j.mtphys.2024.101581.

(155) Zhou, H.; Yan, L.; Yang, Y.; Hong, R.; Zhang, H.; Chu, H. Synergistic Catalytic Effect of

Mo and Ni on the Nitrogen-Doped Carbon Nanotubes in an Axisymmetric Laminar Co-Flow Ethylene/Ammonia/Air Diffusion Flame. *Carbon N. Y.* **2025**, *238*, 120232. https://doi.org/10.1016/j.carbon.2025.120232.

(156) Lin, X.; Tzitzios, V.; Zhang, Q.; Rodriguez, B. J.; Rafferty, A.; Bekarevich, R.; Pissas, M.; Sofianos, M. V. Engineering 2D Nickel Boride/Borate Amorphous/Amorphous Heterostructures for Electrocatalytic Water Splitting and Magnetism. *Sustain. Energy Fuels* **2024**, *8* (10), 2125–2137. https://doi.org/10.1039/D4SE00095A.

(157) Vijayarangan, M.; Sangamithirai, M.; Ashok, V.; Umapathy, K.; Jayabharathi, J.; Thanikachalam, V. Amorphous Cobalt-Impregnated Nitrogen-Doped Carbon Encapsulation Nanochain Enhances Long-Lasting Electrochemical Water Splitting. *ACS Appl. Mater. Interfaces* **2024**, *16* (27), 35013–35023. https://doi.org/10.1021/acsami.4c05382.

(158) Su, Z.; Chen, X.; Sun, M.; Yang, X.; Kang, J.; Cai, Z.; Guo, L. Amorphous Nanobelts for Efficient Electrocatalytic Ammonia Production. *Angew. Chemie* **2025**, *137* (4). https://doi.org/10.1002/ange.202416878.

(159) Zhang, L. Y.; Yuan, W.; Lu, J.; He, M.; Guo, C. X.; Cao, H.; Li, C. M.; Zhao, X. S. Weakening Pd─O Bonds by an Amorphous Pd Layer to Promote Electrocatalysis. *Small* **2025**, *21* (7). https://doi.org/10.1002/smll.202409404.

(160) Yang, J.; Chen, G.; Feng, W.; Guo, Z.; Gu, L.; Li, Z.; Zhao, Y. Room-Temperature High-Efficiency Electrocatalysis in Two-Dimensional Ultrathin Amorphous Ni–Mo–O Nanosheets. *J. Mater. Chem. A* **2025**, *13* (31), 25934–25942. https://doi.org/10.1039/D5TA03090K.

(161) Xu, W.; Zhou, W.; Ye, D.; Luo, X.; Yuan, C.; Lei, W.; Wang, K. Tuning Cu–Cu Spacing in Single-Atomic Layer Cu Catalysts for Efficient and Stable CO2-To-C2H4 Electroreduction. *Adv. Mater.* **2026**, *n/a* (n/a), e22842. https://doi.org/https://doi.org/10.1002/adma.202522842.

(162) Zhan, H.; Jiang, Z.; Luo, X.; Huang, Y.; Ye, D.; Xu, W.; Hu, C.; Zhou, H.; Lei, W.; Yuan, C. A Versatile C/Fe3O4/C Self-Heating Electrode for Universal Application of Alternating Magnetic Fields in Electrocatalytic Hydrogen Production. *Adv. Funct. Mater.* **2024**, *34* (40), 2407600. https://doi.org/https://doi.org/10.1002/adfm.202407600.

(163) Zhou, W.; Zou, C.; Luo, X.; Yuan, C.; Liu, S.; Chen, M.; Zhang, J.; Lei, W.; Wang, S. Enhanced Magnetic Heating for Efficient Oxygen Evolution Reaction by Pinning Effect of Ferromagnetic/Antiferromagnetic Coupling. *Nano Lett.* **2024**, *24* (40), 12420–12425. https://doi.org/10.1021/acs.nanolett.4c02886.

(164) Chen, M.; Zhou, W.; Ye, K.; Yuan, C.; Zhu, M.; Yu, H.; Yang, H.; Huang, H.; Wu, Y.; Zhang, J.; Zheng, X.; Shen, J.; Wang, X.; Wang, S. External Fields Assisted Highly Efficient Oxygen Evolution Reaction of Confined 1T-VSe2 Ferromagnetic Nanoparticles. *Small* **2023**, *19* (38), 2300122. https://doi.org/https://doi.org/10.1002/smll.202300122.

(165) Chunduri, A.; Bhide, A.; Gupta, S.; Mali, K. H.; Bhagat, B. R.; Dashora, A.; Spreitzer, M.; Fernandes, R.; Patel, R.; Patel, N. Exploring the Role of Multi-Catalytic Sites in an Amorphous Co–W–B Electrocatalyst for Hydrogen and Oxygen Evolution Reactions. *ACS Appl. Energy Mater.* **2023**, *6* (9), 4630–4641. https://doi.org/10.1021/acsaem.2c04164.

(166) Yao, Y.; Hu, E.; Wang, Z.; Cui, Y.; Qian, G. Boosting Hydrogen Evolution through the Interface Effects of Amorphous NiMoO 4 –MoO 2 and Crystalline Cu. *ACS Omega* **2022**, *7* (2), 2244–2251. https://doi.org/10.1021/acsomega.1c05844.

(167) Yang, W.; Li, H.; Li, P.; Xie, L.; Liu, Y.; Cao, Z.; Tian, C.; Wang, C.-A.; Xie, Z. Facile Synthesis of Co Nanoparticles Embedded in N-Doped Carbon Nanotubes/Graphitic Nanosheets as Bifunctional Electrocatalysts for Electrocatalytic Water Splitting. *Molecules* **2023**, *28* (18), 6709. https://doi.org/10.3390/molecules28186709.

(168) Liu, S.; Wang, Y.; Zhao, H.; Li, H.; Xiao, W.; Xiao, Z.; Xu, G.; Chen, D.; Wu, Z.; Wang, L. Amorphous W-Doped Iron Phosphide with Superhydrophilic Surface to Boost Water-Splitting under Large Current Density. *Chem. Eng. J.* **2024**, *496*, 153956. https://doi.org/10.1016/j.cej.2024.153956.

(169) Shen, J.; Zheng, Y.; Lei, W.; Shao, H. Unraveling the Fundamental Concepts of Superaerophobic/Superhydrophilic Electrocatalysts for Highly Efficient Water Electrolysis: Implications for Future Research. *ChemElectroChem* **2024**, *11* (2), e202300465. https://doi.org/https://doi.org/10.1002/celc.202300465.

(170) Andaveh, R.; Barati Darband, G.; Maleki, M.; Sabour Rouhaghdam, A. Superaerophobic/Superhydrophilic Surfaces as Advanced Electrocatalysts for the Hydrogen Evolution Reaction: A Comprehensive Review. *J. Mater. Chem. A* **2022**, *10* (10), 5147–5173. https://doi.org/10.1039/D1TA10519A.

(171) Pang, L.; Ma, Q.; Zhu, C. Multifunctional Amorphous Co Phosphosulfide-Coated Fe-Co Carbonate Hydroxide for Highly Efficient Overall Water Splitting. *J. Electron. Mater.* **2023**, *52* (3), 1808–1818. https://doi.org/10.1007/s11664-022-10194-9.

(172) Lee, Y.; Jeong, W.; Hwang, Y. J.; An, B.; Lee, H.; Jeong, H.; Kim, G.; Park, Y.; Kim, M.; Ha, D.-H. Basics, Developments, and Strategies of Transition Metal Phosphides toward Electrocatalytic Water Splitting: Beyond Noble Metal Catalysts. *J. Mater. Chem. A* **2024**, *12* (42), 28574–28594. https://doi.org/10.1039/D4TA04455J.

(173) Huang, S.; Ye, T.; Liu, X.; Cong, X.; Peng, K.; Liu, L.; Jiang, Y.; Chen, Q.; Hu, Z.; Zhang, J. Amorphous and Defective Co-P-O@NC Ball-in-Ball Hollow Structure for Highly Efficient Electrocatalytic Overall Water Splitting. *J. Colloid Interface Sci.* **2023**, *649*, 1047–1059. https://doi.org/10.1016/j.jcis.2023.06.129.

(174) Cao, Y.; Chen, Z.; Ye, F.; Yang, Y.; Wang, K.; Wang, Z.; Yin, L.; Xu, C. One-Step Synthesis of Amorphous NiCoP Nanoparticles by Electrodeposition as Highly Efficient Electrocatalyst for Hydrogen Evolution Reaction in Alkaline Solution. *J. Alloys Compd.* **2022**, *896*, 163103. https://doi.org/10.1016/j.jallcom.2021.163103.

(175) Yadav, A.; Kumar, A.; Purkayastha, S. K.; Guha, A. K.; Ali, M. A.; Deka, S. Nanoarchitectonics of Amorphous Fe–Ni–B Nanosheets for High Throughput Overall Water Splitting Reaction. *Int. J. Hydrogen Energy* **2024**, *53*, 706–716. https://doi.org/10.1016/j.ijhydene.2023.12.106.

(176) Bai, Y.; Wu, Y.; Zhou, X.; Ye, Y.; Nie, K.; Wang, J.; Xie, M.; Zhang, Z.; Liu, Z.; Cheng, T.; Gao, C. Promoting Nickel Oxidation State Transitions in Single-Layer NiFeB Hydroxide Nanosheets for Efficient Oxygen Evolution. *Nat. Commun.* **2022**, *13* (1), 6094. https://doi.org/10.1038/s41467-022-33846-0.

(177) Liang, C.; Zou, P.; Nairan, A.; Zhang, Y.; Liu, J.; Liu, K.; Hu, S.; Kang, F.; Fan, H. J.; Yang, C. Exceptional Performance of Hierarchical Ni–Fe Oxyhydroxide@NiFe Alloy Nanowire Array Electrocatalysts for Large Current Density Water Splitting. *Energy Environ. Sci.* **2020**, *13* (1), 86–95. https://doi.org/10.1039/C9EE02388G.

(178) Shi, X.; Ye, Q.; Huang, Q.; Ma, J.; Liu, Y.; Lin, S. Engineering Amorphous CoNiRuOx Nanoparticles Grown on Nickel Foam for Boosted Electrocatalytic Hydrogen Evolution. *Catalysts* **2025**, *15* (3), 211. https://doi.org/10.3390/catal15030211.

(179) Zhou, T.; Ye, S.; Gao, J.; Zhang, H.; Zhong, S. In Situ Grown Ru-Doped Ni(OH)2 Nanosheets on Nickel Foam for Stable Electrocatalytic Hydrogen Evolution Reaction. *Catal. Sci. Technol.* **2025**, *15* (2), 506–513. https://doi.org/10.1039/D4CY01074D.

(180) Sun, Q.-P.; Wang, T.-T.; Shi, L.-Y.; Deng, Y.; Zhang, S.-F.; Sun, J.-F.; Kang, J.-L.; Li, T.-T.; Li, M.; Mu, Q.-F. Flow-Engineered Multiscale Porous Electrode Design for Promoting Bubbles Removal Efficiency toward High-Current–Density Hydrogen Evolution Reaction. *Rare Met.* **2025**, *44* (12), 10155–10171. https://doi.org/10.1007/s12598-025-03586-3.

(181) Jiang, J.; Dou, H.; Cao, M.; Du, L.; Yan, Y.; Wang, X.; Chen, C.; Ye, L.; Deng, B.; He, H. Amorphous Nickel Oxide Electrodes with High-Current-Density Electrocatalytic Performance for Hydrogen Evolution. *Int. J. Hydrogen Energy* **2024**, *51*, 887–894. https://doi.org/10.1016/j.ijhydene.2023.07.093.

(182) Zhang, J.; Wu, Y.; Hao, H.; Zhang, Y.; Chen, X.; Xing, K.; Xu, J. Construction of Amorphous Fe0.95S1.05 Nanorods with High Electrocatalytic Activity for Enhanced Hydrogen Evolution Reaction. *Electrochim. Acta* **2022**, *402*, 139554. https://doi.org/10.1016/j.electacta.2021.139554.

(183) Wong, T. K. S. Amorphous Transition Metal Sulfide Electrocatalysts for Green Hydrogen Generation from Solar-Driven Electrochemical Water Splitting. *Energies*. 2025, p 6348. https://doi.org/10.3390/en18236348.

(184) Dong, Y.; Fang, Z.; Yang, W.; Tang, B.; Liu, Q. Integrated Bifunctional Electrodes Based on Amorphous Co–Ni–S Nanoflake Arrays with Atomic Dispersity of Active Sites for Overall Water Splitting. *ACS Appl. Mater. Interfaces* **2022**, *14* (8), 10277–10287. https://doi.org/10.1021/acsami.1c22092.

(185) Wu, L.; Hofmann, J. P. Comparing the Intrinsic HER Activity of Transition Metal Dichalcogenides: Pitfalls and Suggestions. *ACS Energy Lett.* **2021**, *6* (7), 2619–2625. https://doi.org/10.1021/acsenergylett.1c00912.

(186) Murthy, R.; Neelakantan, S. C. Graphitic Carbon Cloth-Based Hybrid Molecular Catalyst: A Non-Conventional, Synthetic Strategy of the Drop Casting Method for a Stable and Bifunctional Electrocatalyst for Enhanced Hydrogen and Oxygen Evolution Reactions. *ACS Omega* **2022**, *7* (36), 32604–32614. https://doi.org/10.1021/acsomega.2c04199.

(187) Jian, X.; Zhang, W.; Yang, Y.; Li, Z.; Pan, H.; Gao, Q.; Lin, H.-J. Amorphous Cu–W Alloys as Stable and Efficient Electrocatalysts for Hydrogen Evolution. *ACS Catal.* **2024**, *14* (5), 2816–2827. https://doi.org/10.1021/acscatal.3c05820.

(188) Wang, Z.; Chen, H.; Bao, J.; Song, Y.; She, X.; Lv, G.; Deng, J.; Li, H.; Xu, H. Amorphized Core–Shell NiFeMo Electrode for Efficient Bifunctional Water Splitting. *Appl. Surf. Sci.* **2023**, *607*, 154803. https://doi.org/10.1016/j.apsusc.2022.154803.

(189) Yuan, F.-H.; Mohammadi, M.-R.; Ma, L.-L.; Cui, Z.-D.; Zhu, S.-L.; Li, Z.-Y.; Wu, S.-L.; Jiang, H.; Liang, Y.-Q. Electrodeposition of Self-Supported NiMo Amorphous Coating as an Efficient and Stable Catalyst for Hydrogen Evolution Reaction. *Rare Met.* **2022**, *41* (8), 2624–2632. https://doi.org/10.1007/s12598-022-01967-6.

(190) Wen, Y.; Zhao, Y.; Zhang, Z.; Wu, Y.; Zhu, H.; Xu, K.; Liu, Y. Electrodeposition of NiMo Alloys and Composite Coatings: A Review and Future Directions. *J. Manuf. Process.* **2024**, *119*, 929–951. https://doi.org/https://doi.org/10.1016/j.jmapro.2024.03.099.

(191) Shooshtari Gugtapeh, H.; Rezaei, M. Preparation of a Superhydrophilic and Amorphous Ni-Sb-P Nanostructure: A Highly Performance and Durable Bifunctional Electrocatalyst for Overall Water Splitting. *J. Alloys Compd.* **2022**, *927*, 167035. https://doi.org/10.1016/j.jallcom.2022.167035.

(192) Yang, B.; Xu, J.; Bin, D.; Wang, J.; Zhao, J.; Liu, Y.; Li, B.; Fang, X.; Liu, Y.; Qiao, L.; Liu, L.; Liu, B. Amorphous Phosphatized Ruthenium-Iron Bimetallic Nanoclusters with Pt-like Activity for Hydrogen Evolution Reaction. *Appl. Catal. B Environ.* **2021**, *283*, 119583. https://doi.org/10.1016/j.apcatb.2020.119583.

(193) Wang, R.; Li, D.; Li, T.; Sun, W.; Hu, W. Crystalline-Amorphous Ru@RuP Core-Shell Nanoparticles Anchored on Carbon Nanotube for Enhanced Hydrogen Evolution Electrocatalysis. *Colloids Surfaces A Physicochem. Eng. Asp.* **2023**, *668*, 131452. https://doi.org/https://doi.org/10.1016/j.colsurfa.2023.131452.

(194) Kang, Y.; Han, Y.; Chen, H.; Borrmann, H.; Adler, P.; Pohl, D.; Hantusch, M.; König, M.; He, Y.; Ma, Y.; Wang, X.; Felser, C. Ruthenium-Alloyed Iron Phosphide Single Crystal with Increased Fermi Level for Efficient Hydrogen Evolution. *ACS Appl. Mater. Interfaces* **2022**, *14* (50), 55587–55593. https://doi.org/10.1021/acsami.2c16419.

(195) Bae, S.-Y.; Mahmood, J.; Jeon, I.-Y.; Baek, J.-B. Recent Advances in Ruthenium-Based Electrocatalysts for the Hydrogen Evolution Reaction. *Nanoscale Horizons* **2020**, *5* (1), 43–56. https://doi.org/10.1039/C9NH00485H.

(196) El-Refaei, S. M.; Russo, P. A.; Schultz, T.; Chen, Z.-N.; Amsalem, P.; Koch, N.; Pinna, N. Activating Ru in the Pyramidal Sites of Ru2P-Type Structures with Earth-Abundant Transition Metals for Achieving Extremely High HER Activity While Minimizing Noble Metal Content. *Carbon Energy* **2024**, *6* (9), e556. https://doi.org/https://doi.org/10.1002/cey2.556.

(197) Jiang, M.; Zhang, J.; Liao, H.; Zhai, H.; Liu, X.; Tan, P.; Yang, K.; Pan, J. The Ultrafast Reconfigurability and Ultrahigh Durability of an NiFe Phosphide Electrocatalyst with an Fe-Rich Surface Induced by in Situ Acid Corrosion for Water Oxidations. *Inorg. Chem. Front.* **2024**, *11* (18), 6168–6177. https://doi.org/10.1039/D4QI01378F.

(198) Wang, Y.; Yang, P.; Gong, Y.; Liu, D.; Liu, S.; Xiao, W.; Xiao, Z.; Li, Z.; Wu, Z.; Wang, L. Amorphous High-Valence Mo-Doped NiFeP Nanospheres as Efficient Electrocatalysts for Overall Water-Splitting under Large-Current Density. *Chem. Eng. J.* **2023**, *468*, 143833. https://doi.org/10.1016/j.cej.2023.143833.

(199) Li, K.; Xiang, J.; Ma, X.; Wu, J.; Tao, Z.; Zheng, J.; Xue, J. Mo-Doping Directed Nanoflower Architecture in NiFe Phosphide for Ultralow-Overpotential Oxygen Evolution Catalysis. *Mater. Chem. Phys.* **2026**, *348*, 131578.

https://doi.org/https://doi.org/10.1016/j.matchemphys.2025.131578.

(200) Khan, S. A. Facile Synthesis of Amorphous Co Engineered FePO4: As an Efficient Electrocatalyst for Hydrogen and Oxygen Evolution Reactions. *Int. J. Hydrogen Energy* **2025**, *144*, 417–429. https://doi.org/10.1016/j.ijhydene.2025.06.050.

(201) Wang, N.; Yu, J.; Wang, C.; Li, G.; Liu, X.; Gao, H. Amorphous Ternary Mn-Co-B as a Highly Efficient Electrocatalyst for Oxygen Evolution Reaction: Experimental and Theoretical Study. *Mater. Today Commun.* **2021**, *26*, 102157. https://doi.org/10.1016/j.mtcomm.2021.102157.

(202) Samanta, R.; Mishra, R.; Manna, B. K.; Barman, S. Two-Dimensional Amorphous Cobalt Oxide Nanosheets/N-Doped Carbon Composites for Efficient Water Splitting in Alkaline Medium. *ACS Appl. Nano Mater.* **2022**, *5* (11), 17022–17032. https://doi.org/10.1021/acsanm.2c03941.

(203) Wu, D.; Chen, D.; Zhu, J.; Mu, S. Ultralow Ru Incorporated Amorphous Cobalt-Based Oxides for High-Current-Density Overall Water Splitting in Alkaline and Seawater Media. *Small* **2021**, *17* (39). https://doi.org/10.1002/smll.202102777.

(204) Wang, C.; Shang, H.; Li, J.; Wang, Y.; Xu, H.; Wang, C.; Guo, J.; Du, Y. Ultralow Ru Doping Induced Interface Engineering in MOF Derived Ruthenium-Cobalt Oxide Hollow Nanobox for Efficient Water Oxidation Electrocatalysis. *Chem. Eng. J.* **2021**, *420*, 129805. https://doi.org/https://doi.org/10.1016/j.cej.2021.129805.

(205) Xiao, H.; Yin, H.; Li, X.; Zhou, X.; Zhang, W.; Pan, F.; Zhao, J.; Guo, J.; Li, S.; Qian, L. An Intrinsic Mechanism of Surface Reconstruction of Cobalt-Based Oxide Intermediated by Oxygen Vacancies. *Sustain. Mater. Technol.* **2024**, *40*, e00955. https://doi.org/https://doi.org/10.1016/j.susmat.2024.e00955.

(206) Zhang, R.; Qian, B.; Xu, K.; Said, A.; Chen, K.; Yang, C.; Komarneni, S.; Xue, D. Dynamic Lattice Reconstruction of Transition Metal Sulfides: Insights into Microstructural Evolution and Electrocatalytic Performance Enhancement. *Rev. Mater. Res.* **2025**, *1* (3), 100045. https://doi.org/https://doi.org/10.1016/j.revmat.2025.100045.

(207) Kale, S. B.; Bhardwaj, A.; Lokhande, V. C.; Lee, D.-M.; Kang, S.-H.; Kim, J.-H.; Lokhande, C. D. Amorphous Cobalt-Manganese Sulfide Electrode for Efficient Water Oxidation: Meeting the Fundamental Requirements of an Electrocatalyst. *Chem. Eng. J.* **2021**, *405*, 126993. https://doi.org/10.1016/j.cej.2020.126993.

(208) Kim, Y. J.; Lim, A.; Kim, J. M.; Lim, D.; Chae, K. H.; Cho, E. N.; Han, H. J.; Jeon, K. U.; Kim, M.; Lee, G. H.; Lee, G. R.; Ahn, H. S.; Park, H. S.; Kim, H.; Kim, J. Y.; Jung, Y. S. Highly Efficient Oxygen Evolution Reaction via Facile Bubble Transport Realized by Three-Dimensionally Stack-Printed Catalysts. *Nat. Commun.* **2020**, *11* (1), 4921. https://doi.org/10.1038/s41467-020-18686-0.

(209) Abd-Elrahim, A. G.; Ali, M. A.; Chun, D.-M. Enhanced Oxygen Evolution Using Sulfate-Intercalated Amorphous FeNiS@FeS Layered Double Hydroxide Nanoflowers for Advanced Water-Splitting Performance. *J. Power Sources* **2025**, *635*, 236472. https://doi.org/10.1016/j.jpowsour.2025.236472.

(210) Maghool, S.; Asgharinezhad, A. A.; Larimi, A.; Ghotbi, C.; Khorasheh, F. Efficient Electrocatalysts for OER: Amorphous Cerium-Doped Cobalt Sulfide with Enhanced

Performance and Durability. *Surfaces and Interfaces* **2024**, *54*, 105108. https://doi.org/10.1016/j.surfin.2024.105108.

(211) He, W.; Wang, F.; Gao, Y.; Hao, Q.; Liu, C. One-Step Synthesis of Amorphous Transition Metal Sulfides as Bifunctional Electrocatalysts for the Hydrogen Evolution Reaction and Oxygen Evolution Reaction. *Sustain. Energy Fuels* **2022**, *6* (16), 3852–3857. https://doi.org/10.1039/D2SE00886F.

(212) Chaudhary, K. J.; Patel, R.; Chaudhary, M. L.; Gupta, R. K. Progress in Transition Metal Sulfides for Oxidation Reactions BT - Handbook of Energy Materials; Gupta, R., Ed.; Springer Nature Singapore: Singapore, 2022; pp 1–24. https://doi.org/10.1007/978-981-16-4480-1_83-1.

(213) Qiu, P.; Fang, Z.; Yuan, L.; Hou, J.; Zhu, J.; Ke, C.; Zhang, L.; Zhuang, X. Amorphous NiFeCo Oxyhydroxide as a High-Performance Electrocatalyst for Alkaline Oxygen Evolution Reaction. *ChemCatChem* **2025**. https://doi.org/10.1002/cctc.202500454.

(214) Han, X.; Cheng, Z.; Zhang, J.; Liu, J.; Zhong, C.; Hu, W. Design of Amorphous High-Entropy FeCoCrMnBS (Oxy) Hydroxides for Boosting Oxygen Evolution Reaction. *Acta Physico-Chimica Sin.* **2025**, *41* (4), 100033. https://doi.org/10.3866/PKU.WHXB202404023.

(215) Li, X.; Xie, Z.; Roy, S.; Gao, L.; Liu, J.; Zhao, B.; Wei, R.; Tang, B.; Wang, H.; Ajayan, P.; Tang, K. Amorphous High-entropy Phosphide Nanosheets With Multi-atom Catalytic Sites for Efficient Oxygen Evolution. *Adv. Mater.* **2025**, *37* (10). https://doi.org/10.1002/adma.202410295.

(216) Manso, R. H.; Hong, J.; Wang, W.; Acharya, P.; Hoffman, A. S.; Tong, X.; Wang, F.; Greenlee, L. F.; Zhu, Y.; Bare, S. R.; Chen, J. Revealing Structural Evolution of Nickel Phosphide-Iron Oxide Core–Shell Nanocatalysts in Alkaline Medium for the Oxygen Evolution Reaction. *Chem. Mater.* **2024**, *36* (13), 6440–6453. https://doi.org/10.1021/acs.chemmater.4c00379.

(217) Chen, X.; Tao, J.; Ha, Y.; Xu, Z.; Zhu, X.; Xu, D.; Zhou, T. Amorphous NiMoCu-PO/NF as a Bifunctional Catalyst for Effective Water Splitting. *Int. J. Hydrogen Energy* **2025**, *106*, 1041–1049. https://doi.org/10.1016/j.ijhydene.2025.02.050.

(218) Xu, Z.; Wang, Z.; Yang, L.; Xu, H. Porous High-Entropy Phosphides with Multiple Active Sites for Synergistically Promoting Electrocatalytic Oxygen Evolution Reaction. *Appl. Surf. Sci.* **2025**, *698*, 163090. https://doi.org/https://doi.org/10.1016/j.apsusc.2025.163090.

(219) Yan, S.; Zhong, M.; Wang, C.; Lu, X. Amorphous Aerogel of Trimetallic FeCoNi Alloy for Highly Efficient Oxygen Evolution. *Chem. Eng. J.* **2022**, *430*, 132955. https://doi.org/10.1016/j.cej.2021.132955.

(220) Chai, L.; Liu, S.; Pei, S.; Wang, C. Electrodeposited Amorphous Cobalt-Nickel-Phosphide-Derived Films as Catalysts for Electrochemical Overall Water Splitting. *Chem. Eng. J.* **2021**, *420*, 129686. https://doi.org/10.1016/j.cej.2021.129686.

(221) Yu, X.; Yang, J.; Sui, Z.; Wang, M. Effects of Ultrasonic Field on Structure Evolution of Ni Film Electrodeposited by Bubble Template Method for Hydrogen Evolution Electrocatalysis. *J. Solid State Electrochem.* **2021**, *25* (8), 2201–2212. https://doi.org/10.1007/s10008-021-04980-4.

(222) Wang, C.; Wu, Y.; Zhou, Z.; Wang, J.; Pei, S.; Liu, S. Electrodeposited Amorphous Nickel–Iron Phosphide and Sulfide Derived Films for Electrocatalytic Oxygen Evolution. *Int. J. Hydrogen Energy* **2022**, *47* (97), 40849–40859. https://doi.org/https://doi.org/10.1016/j.ijhydene.2022.09.200.

(223) Hou, W.; Zhou, C.; Li, Q.; Zhou, H.; Liu, Z.; Yang, L.; Wu, C.; Zhao, H.; Dong, S. Preparation and Overall Water-Splitting Performance Study of Amorphous Nickel-Copper-Phosphide. *J. Alloys Compd.* **2024**, *1002*, 175314. https://doi.org/10.1016/j.jallcom.2024.175314.

(224) Wei, L.; Goh, K.; Birer, Ö.; Karahan, H. E.; Chang, J.; Zhai, S.; Chen, X.; Chen, Y. A Hierarchically Porous Nickel–Copper Phosphide Nano-Foam for Efficient Electrochemical Splitting of Water. *Nanoscale* **2017**, *9* (13), 4401–4408. https://doi.org/10.1039/C6NR09864A.

(225) Chen, Z.; Kang, Q.; Cao, G.; Xu, N.; Dai, H.; Wang, P. Study of Cobalt Boride-Derived Electrocatalysts for Overall Water Splitting. *Int. J. Hydrogen Energy* **2018**, *43* (12), 6076–6087. https://doi.org/10.1016/j.ijhydene.2018.01.161.

(226) Song, S.; Wang, Y.; Liu, Y.; Tian, P.; Zang, J. Heterogeneous Ni-Boride/Phosphide Anchored Amorphous B-C Layer for Overall Water Electrocatalysis. *ChemSusChem* **2024**. https://doi.org/10.1002/cssc.202301547.

(227) He, Y.; Cui, Y.; Zhao, Z.; Chen, Y.; Shang, W.; Tan, P. Strategies for Bubble Removal in Electrochemical Systems. *Energy Rev.* **2023**, *2* (1), 100015. https://doi.org/https://doi.org/10.1016/j.enrev.2023.100015.

(228) Angulo, A.; van der Linde, P.; Gardeniers, H.; Modestino, M.; Fernández Rivas, D. Influence of Bubbles on the Energy Conversion Efficiency of Electrochemical Reactors. *Joule* **2020**, *4* (3), 555–579. https://doi.org/10.1016/j.joule.2020.01.005.

(229) He, J.-C.; Duan, D.-C.; Du, Y.-C.; Ding, Z.-Q.; Yan, S.-S.; Chen, X.; Zhang, H.; Bi, X.-X.; Wang, R.-Y.; Ge, X.-B. Three-Dimensional Amorphous N-Doped Cobalt–Copper Sulfide Nanostructures for Efficient Full Water Splitting. *Rare Met.* **2025**, *44* (5), 3080–3093. https://doi.org/10.1007/s12598-024-03035-7.

(230) Sun, H.; Kim, H.; Song, S.; Jung, W. Copper Foam-Derived Electrodes as Efficient Electrocatalysts for Conventional and Hybrid Water Electrolysis. *Mater. Reports Energy* **2022**, *2* (2), 100092. https://doi.org/https://doi.org/10.1016/j.matre.2022.100092.

(231) Li, X.; Xiao, L.; Zhou, L.; Xu, Q.; Weng, J.; Xu, J.; Liu, B. Adaptive Bifunctional Electrocatalyst of Amorphous CoFe Oxide @ 2D Black Phosphorus for Overall Water Splitting. *Angew. Chemie Int. Ed.* **2020**, *59* (47), 21106–21113. https://doi.org/10.1002/anie.202008514.

(232) Yin, Z.-H.; Liu, H.; Hu, J.-S.; Wang, J.-J. The Breakthrough of Oxide Pathway Mechanism in Stability and Scaling Relationship for Water Oxidation. *Natl. Sci. Rev.* **2024**, *11* (11), nwae362. https://doi.org/10.1093/nsr/nwae362.

(233) Wu, X.; Li, Z.; Wang, H.; Wang, J.; Xi, G.; Zhao, X.; Zhang, C.; Liao, W.; Ho, J. C. Defect-Engineered Multi-Intermetallic Heterostructures as Multisite Electrocatalysts for Efficient Water Splitting. *Adv. Sci.* **2025**, *12* (26). https://doi.org/10.1002/advs.202502244.

(234) Su, J.; Jiang, N.; Wang, Y.; Jiang, B.; Wang, X.; Song, H. Manipulating Interfacial Built-in Electric Field of Heterostructure Catalysts to Promote Overall Water Splitting in Alkaline. *J. Colloid Interface Sci.* **2025**, *699*, 138177. https://doi.org/https://doi.org/10.1016/j.jcis.2025.138177.

(235) Yang, K.; Xu, P.; Lin, Z.; Yang, Y.; Jiang, P.; Wang, C.; Liu, S.; Gong, S.; Hu, L.; Chen, Q. Ultrasmall Ru/Cu-doped RuO 2 Complex Embedded in Amorphous Carbon Skeleton as Highly Active Bifunctional Electrocatalysts for Overall Water Splitting. *Small* **2018**, *14* (41). https://doi.org/10.1002/smll.201803009.

(236) Wu, X.; Wu, J.; Zhu, L.; Hu, N.; Zhang, Y.; Wang, Z.; Qiu, H.-J. Enhanced Ruthenium Oxide-Based OER Catalyst by Multicomponent Acid-Tolerant Element Doping. *Mater. Today Energy* **2025**, *52*, 101919. https://doi.org/https://doi.org/10.1016/j.mtener.2025.101919.